Grigorios Koltsakis*, Onoufrios Haralampous, Christopher Depcik and J. Colter Ragone

Catalyzed diesel particulate filter modeling

Abstract: An increasing environmental concern for diesel particulate emissions has led to the development of efficient and robust diesel particulate filters (DPF). Although the main function of a DPF is to filter solid particles, the beneficial effects of applying catalytic coatings in the filter walls have been recognized. The catalyzed DPF technology is a unique type of chemical reactor in which a multitude of physicochemical processes simultaneously take place, thus complicating the tasks of design and optimization. To this end, modeling has contributed considerably in reducing the development effort by offering a better understanding of the underlying phenomena and reducing the excessive experimental efforts associated with experimental testing. A comprehensive review of the evolution and the most recent developments in DPF modeling, covering phenomena such as transport, fluid mechanics, filtration, catalysis, and thermal stresses, is presented in this article. A thorough presentation on the mathematical model formulation is given based on literature references and the differences between modeling approaches are discussed. Selected examples of model application and validation versus the experimental data are presented.

Keywords: diesel particulate filter; filtration; mathematical modeling; soot oxidation.

***Corresponding author: Grigorios Koltsakis**, Laboratory of Applied Thermodynamics, Aristotle University Thessaloniki, University Campus, 54124 Thessaloniki, Greece, e-mail: Grigoris@auth.gr
Onoufrios Haralampous: Laboratory of Heat Transfer, Department of Mechanical Engineering, Technological Educational Institute of Larissa, 41110 Larissa, Greece
Christopher Depcik and J. Colter Ragone: Department of Mechanical Engineering, University of Kansas, 3144C Learned Hall, 1530 West 15th Street, Lawrence, KS 66049, USA

1 Introduction

The international environmental legislation is enacting increasingly stringent regulations on the engine emission levels. These levels have gotten sufficiently low that the improvements to the engine's combustion and fuel delivery technology no longer can meet these requirements without the aid of the aftertreatment devices. In particular, the direct-injection compression-ignition engine aftertreatment systems must specifically target particulate matter (PM; also referred to as soot) emission levels through a diesel particulate filter (DPF). Moreover, the newer model direct-injection spark-ignition engines are under analysis for their PM levels that may require the future implementation of a DPF.

1.1 Scope

DPFs have been researched for close to three decades based on their ability to capture PM or soot with approximately 100% efficiency (Springer and Stahman 1977, General Motors 1979, Tessier et al. 1980, Howitt and Montierth 1981). In the early market introduction, a fibrous type of DPF was used, which trapped the PM according to the classic theory of aerosol filtration, as shown in Figure 1 (Oh et al. 1981, Shadman and Bissett 1983, Garner and Dent 1988). Although the collection efficiency of such a device is initially high, eventually the tendency of the PM to adhere to the fibers decreases, lowering its trapping efficiency (MacDonald and Vaneman 1981). Hence, most researchers abandoned this type of device and instead moved onto the porous wall type.

The porous wall DPF consists of a honeycomb of long channels similar to the traditional catalytic converter (Howitt and Montierth 1981). Unlike the catalytic converter, the manufacturer now blocks alternating open channels of the honeycomb, so all of the flow entering the device must pass through a porous wall as illustrated in Figure 2. The sizes of the pores in the wall are of appropriate size to capture PM by diffusion and secondarily by interception. After the soot amount in the wall exceeds a certain level, the inlet pores are bridged by soot and a soot cake deposit starts to build up. The accumulation of soot in the wall and on the surface increases the flow resistance and the pressure drop. Eventually, regeneration is required to reduce the pressure drop to a more reasonable value. Similar to the fibrous DPF, this regeneration occurs through a temperature excursion with the proper amount of oxidant available. The energy released by this oxidation conducts along the monolith and advects to the exhaust flow that passes through the deposited PM layer and the porous wall. The structure of the DPF offers the advantage of a large potential filter area in a reasonably compact

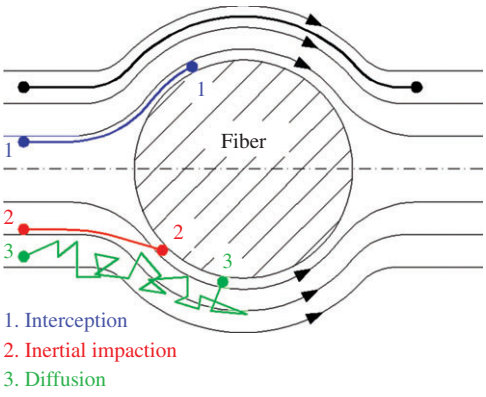

Figure 1 Particle collection mechanisms by a single fiber (Oh et al. 1981).

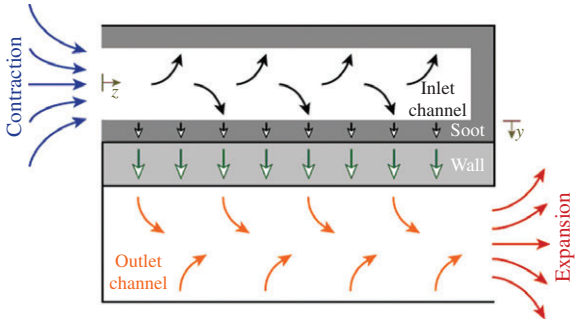

Figure 2 Flow schematic of a DPF (Depcik and Assanis 2008).

volume. In addition, another benefit of this type of DPF is that the PM eventually builds up on the inlet channel, forming a "soot cake", which acts as a nearly 100% filter.

The flow through a DPF is, in principle, three-dimensional (3D) with a different PM loading, oxidation, and temperature for each flow channel. Furthermore, when the DPF is located close to the exhaust manifold, the pulsating flow leaving the engine along with the 3D geometry of the manifold creates a flow maldistribution within the DPF that can lead to partial regeneration events and an incomplete utilization. Nonetheless, there are many applications in the exhaust where the flow profile has time to develop and provide relatively uniform inlet conditions. For those types of problems, a one-dimensional (1D)–based treatment of the DPF will often yield satisfactory results (Bissett 1984, Konstandopoulos and Johnson 1989, Koltsakis and Stamatelos 1997a,b). In addition, when studying catalyzed DPFs, these 1D-based models incorporating chemical kinetics have a significant computational edge over their 3D counterparts. 1D models are also attractive for engine aftertreatment system configuration studies, where the placement and the size of a number of aftertreatment devices need to be optimized. Lastly, if multidimensional models of DPFs are needed, the 1D model can be readily adapted (Gropi and Tronconi 1996, Konstandopoulos et al. 2001, Haralampous et al. 2003, Kostoglou et al. 2003).

As discussed in a previous article (Depcik and Assanis 2005), a monolithic type of device can be reduced from 3D to 1D by making a number of reasonable assumptions as illustrated in Figure 3. The first step in simplifying the modeling effort is to reduce the 3D device in Cartesian coordinates into two-dimensional (2D) cylindrical coordinates: axial and radial. Keeping these radial components allows for a 2D DPF model, however, assuming that all axial and radial cells are identical results in the traditional 1D model. Whereas a catalyst only needs one channel to describe the proper flow profile, a DPF will need an inlet and outlet channel to obtain the correct profile.

The scope of this work is to present a thorough history of DPF modeling efforts. This will begin by first illustrating some of the early preliminary efforts at modeling both fibrous- and monolithic-type devices. Next, the authors summarize the pioneering work by Bissett and Shadman (Bissett 1984, 1985, Bissett and Shadman 1985) to illustrate the foundation of the classic 1D model. Then, this article illustrates the extensions to the model according to the governing equations of flow, indicating primary and secondary phenomena along with how the equations are continually evolving into 1+1D, 2D, and 3D regimes. Finally,

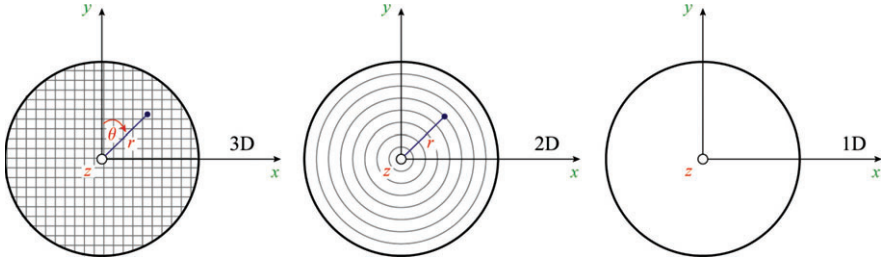

Figure 3 Monolithic device modeling in various levels of dimensional description.

this work indicates how to use this model in conjunction with real-world operation.

1.2 Early history

Wark and Warner (1981) describe the use of fabric filters for particulate control in industrial applications. The pressure drop across these fabric filters is a function of both the dust layer and the filter represented by Darcy's law:

$$\Delta p = \frac{\mu u t}{\mathrm{K}}, \tag{1}$$

which is a phenomologically derived constitutive equation that describes the flow of a fluid through a porous medium and is an expression of the conservation of momentum. Except for the permeability (K), all of the variables in this equation can be determined. This coefficient is independent of the nature of the fluid, but it depends on the geometry of the medium that is a function of the deposited PM: porosity, specific surface area, pore size distribution, and particle size distribution. The overall pressure drop across an industrial fabric filter is a sum of the individual pressure drops across the filter cloth and the deposited particulate.

They state that the pressure drop is essentially a constant for a given cloth material and particulate. Models may assume these values as separate but constant permeabilities for the filter wall and PM. During operation, the thickness of the dust layer builds up with time, increasing the pressure drop across the filter. They find that initially the pressure drop curve is nonlinear, accounting for a new filter cake forming on a clean filter cloth. The surface of the PM layer is irregular for an initial time and the resistance to flow increases rapidly until the complete filling of the nonhomogeneous regions in the dust layer. Once a uniform bed is established, the filter drag then varies linearly as shown in Figure 4.

Around the same time, Mogaka et al. (1982) formulate the first model of an alternating channel, porous wall DPF. In their model, they use dimensionless parameters to describe the relationship between trap performance and various operating and design parameters. They depict the pressure drop across the DPF as

$$\Delta p_{trap} = \Delta p_{wall} + \Delta p_{channel} = \frac{c}{2}\left(\frac{\rho u d}{\mu}\right)^{x} \rho u^2, \tag{2}$$

where c and x are empirical constants. Figure 5 illustrates how this article defines the geometric variables of interest.

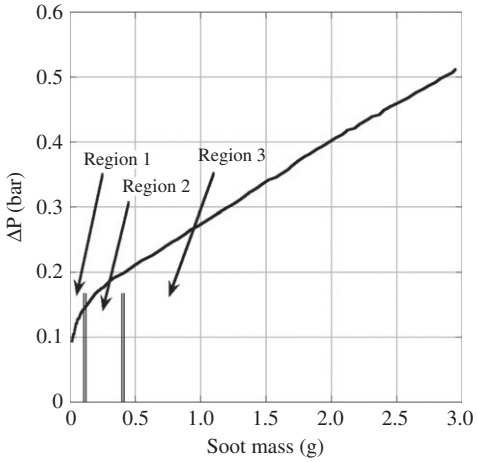

Figure 4 Three regions of pressure drop during PM loading (Versaevel et al. 2000).

The empirical relationships of Benedict et al. (1966) are used to account for inlet and exit pressure losses:

$$\Delta p_{inlet} = 0.25\,\rho u_{channel}^2 \quad \text{and} \quad \Delta p_{exit} = 0.549\,\rho u_{channel}^{1.919} \tag{3}$$

with the pressure drops calculated as a function of the axial velocity through the channels ($u_{channel}$).

The main contribution of Mogaka et al. is a first attempt at simulating the particulate accumulation and oxidation that occurs within the filter by estimating the net accumulation rate of soot $(\dot{m}_{accumulation})$ as

$$\dot{m}_{accumulation} = \dot{m}_{in} - \dot{m}_{out} - \dot{m}_{oxidation}, \tag{4}$$

where $\dot{m}_{in}$ and $\dot{m}_{out}$ are the mass flow rates of soot into and out of the DPF with the oxidation rate $(\dot{m}_{oxidation})$ written as a function of the mass of particulate on the surface (m_d), the surface area of soot (S_p), and the oxygen concentration at the surface:

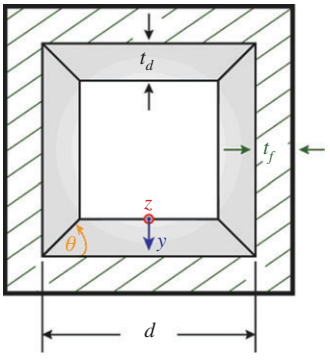

Figure 5 Schematic of single-cell and associated variables (Depcik and Assanis 2008).

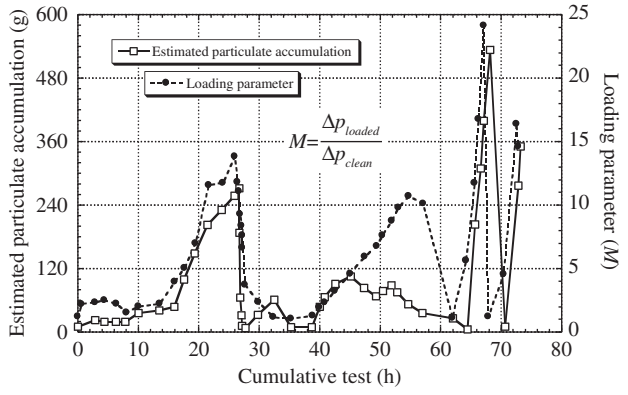

Figure 6 Mogaka et al.'s (1982) comparison of loading parameter with estimated particulate accumulation.

$$\dot{m}_{oxidation} = A m_d S_p p C_{O_2} \exp\left(\frac{-E_a}{R_u T_f}\right), \tag{5}$$

with A and E_a as the traditional Arrhenius rate preexponential and activation energy terms. Their model results reproduced in Figure 6 show a reasonable correlation with the experimental data.

In the following year, Pauli et al. (1983) expand the DPF model by incorporating a third equation for the filter energy. As shown by their results in Figure 7A, this energy balance for the deposit layer and underlying filter material describes the influence of heat transfer conditions through the channel temperature (T) and reaction enthalpy on the local temperature of the oxidizing particulate:

$$\left(m_f c_f + m_d c_d\right)\frac{\partial T_f}{\partial t} = R m_d \Delta H_{reac} - h_g S_a \left(T - T\right) \tag{6}$$

with the reaction rate of deposit written as

$$R = A C_{O_2}^x \exp\left(-E_a / R_u T_f\right), \tag{7}$$

where A and E_a are again the traditional Arrhenius terms, and the order of reaction, x, was characterized to be less than or equal to unity for oxygen concentrations >9% by volume.

They write the net accumulation of particulate slightly different from Mogaka et al. by including a filtration efficiency term:

$$\frac{dm_d}{dt} + R m_d - \eta_d \dot{m}_d = 0, \tag{8}$$

where η_d and $\dot{m}_d$ are the filtration efficiency and the particulate mass flow rate, respectively. In addition, they determine that the exhaust flow through the walls leads to a reduction of the exhaust flow over the length of the filter channel as shown in Figure 7B. As a result, they formulate the following relationship between the exhaust volumetric flow rate $\left(\dot{V}_w\right)$ through the wall and the flow resistance coefficients of the filter wall (ψ_f) and soot layer (ψ_d):

$$\dot{V}_w \sim \frac{1}{\left(\psi_f + \psi_d\right)}. \tag{9}$$

This expression is a precursor to the flow terms that will appear in the continuity equations describing mass lost in the inlet channel.

1.3 Bissett and Shadman's wall model

Bissett and Shadman (1985) initialize the modern path of DPF modeling by exploring the thermal regeneration

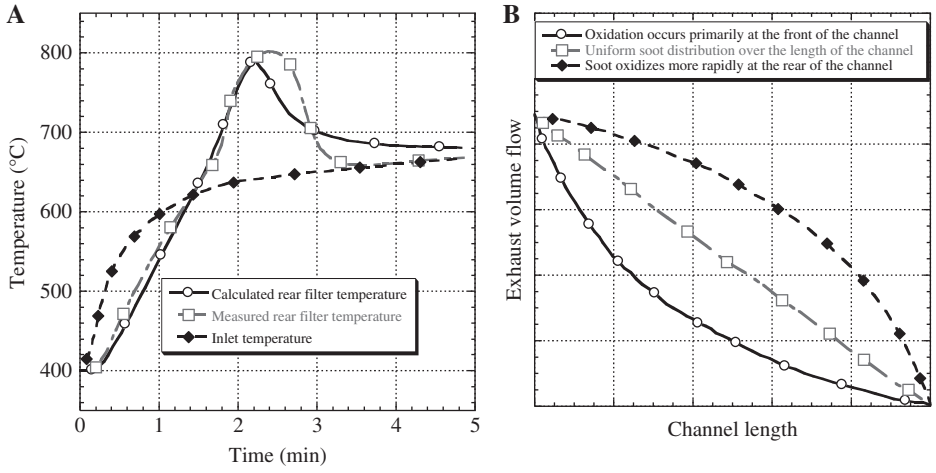

Figure 7 (A) Exhaust and filter temperature during regeneration and (B) influence of particle load variation on axial exhaust flow distribution (Pauli et al. 1983).

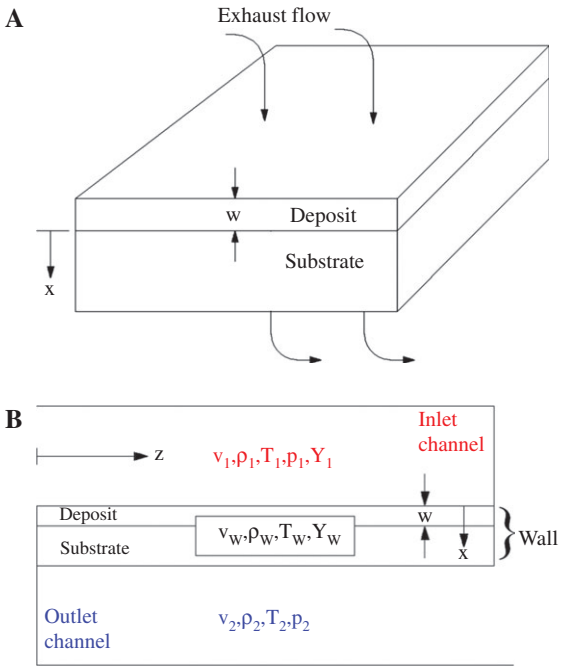

Figure 8 (A) Bissett and Shadman's (1985) wall model and (B) Bissett's (1984) channel model.

of the filter through a detailed study of the wall system as illustrated in Figure 8. Bissett uses the conclusions, in this article, to help create the standard channel model seen in widespread use today that is presented in the next section. It is important to mention that, although the actual in press date for this reference states 1985, this article was the first written and submitted of the two Bissett-authored articles. This model simulates the governing equations in the PM and wall layers according to the following assumptions:

- The change in the internal structure of the deposit during reaction will be neglected.
- The addition of particles to the deposit can be neglected because the duration of regeneration is short.
- All variations in the direction perpendicular to *y* will be neglected.
- The flow distributes itself uniformly over the entire filtration area; hence, the filtration area is uniformly loaded with particles.
- Conductive heat transfer between the channel gas and the filter walls is negligible compared with convective transport in the channels, so the entire length of the channels will be exposed to similar temperatures (isothermal channels during conditions of high flow rates).
- Gas molecular weight through the PM and wall layers is constant.

This model neglects the influence of the channel variations in temperature and species on the solution to the equations in the PM and wall layers. Of particular importance is the usage of constant mole fractions for the chemical species inlet channel. This is because later researchers find that the mass diffusion to the surface from the channel is important. This is what will require a merging of two 1D models into one complete 1+1D simulation.

1.3.1 Continuity and species equations

Determining the equation for the particle mass balance requires a mathematical exercise to calculate the change in oxygen mole fraction through the wall. As a result, Bissett and Shadman write the equation for continuity in the wall as

$$\frac{\partial(\rho_w u_w)}{\partial y}=0. \tag{10}$$

They state that any reactant mass added to the gas phase from PM combustion is negligible compared with the advected mass flux. Later researchers revisit this assumption and subsequently incorporate a term to account for PM conversion into gaseous products.

To model the local oxygen level in the inlet channel, Bissett assumes that advection dominates oxygen transport in the porous wall (unlike temperature presented subsequently); hence, the depletion of oxygen in the reactive deposit layer does not influence the oxygen concentration at the upstream channel and wall interface. Then, by neglecting any gas-phase reactions in the channels, the mole fraction of oxygen in the entire upstream channel will be equal to its value at the inlet:

$$\frac{dX_{I,O_2}}{dz}=0. \tag{11}$$

The local oxygen level in the PM layer is governed by a balance between advective transport in the *y*-direction,

$$\frac{\partial\left(\rho_w u_w X_{s,O_2}\right)}{\partial y}=-kS_p\rho_w X_{s,O_2}, \tag{12}$$

and the PM reaction is expressed as a first-order heterogeneous oxidation of solid carbon oxidizing into carbon dioxide,

$$C_{(s)}+O_2\rightarrow CO_2, \tag{13}$$

where $k=AT_f \exp(-E_a/R_uT_f)$. The oxidation expression in Eq. (12) includes a specific area term (S_p), which is a function of the geometric properties of the PM layer.

The wall species equation for oxygen is

$$\frac{\partial\left(\rho_w u_w X_{w,O_2}\right)}{\partial y}=0. \quad (14)$$

Note that the *s* notation on the mole fractions (X) indicates the values for the mole fractions in the PM layer, whereas *w* indicates the values for the mole fractions in the wall layer. The authors indicate a specific nomenclature difference here (indicated as regions 1 and 2 in the Bissett and Shadman article) to prepare the readers for later revisions in a following section. Moreover, Bissett and Shadman use average density (ρ_w) and velocity (u_w) values for both layers that will be revisited by future authors.

1.3.2 Particle mass balance

By expanding Eq. (12) according to the chain rule, substituting the equation for continuity in the wall via Eq. (10) and using the method of separation of variables while integrating over oxygen mole fraction generates the following result:

$$X_{s,O_2}\Big|_{y=t_d}=\frac{X_{s,O_2}\Big|_{y=0}}{\exp\left(kS_pt_d/u_w\right)}. \quad (15)$$

The total change in the oxygen mole fraction through the wall is then equal to

$$\Delta X_{s,O_2}=X_{s,O_2}\Big|_{y=0}-X_{s,O_2}\Big|_{y=t_d}=X_{s,O_2}\Big|_{y=0}\left[1-\exp\left(-kS_pt_d/u_w\right)\right]. \quad (16)$$

Since Bissett and Shadman assume that the mole fraction of oxygen is constant in the inlet channel via Eq. (11), the change in oxygen mass flow rate through the wall per unit surface area is

$$\dot{m}_{w,O_2}=\rho_w u_w X_{I,O_2}\left[1-\exp\left(-kS_pt_d/u_w\right)\right]. \quad (17)$$

Using the PM oxidation reaction of Eq. (13) for the molar ratios, along with the relative mass differences between the PM (assumed as solid carbon) and oxygen, allows a computation of the time change in mass of the PM,

$$\rho_d\frac{\partial t_d}{\partial t}=-\left(W_{C_{(s)}}/W_a\right)\rho_w u_w X_{I,O_2}\left[1-\exp\left(-kS_pt_d/u_w\right)\right], \quad (18)$$

with W_a as the molecular weight of the gaseous mixture and the density of the PM before the derivative converts the right-hand side into the proper units of thickness. This equation assumes that all the deposit consumed in the reaction shrinks the thickness of the deposit layer while keeping the particle bulk density and particulate specific area constant. The subsequent simulation results illustrate that although reactions can occur throughout the entire deposit later, often most PM depletion occurs in a thin layer near the surface.

1.3.3 Energy balances

Bissett and Shadman's initial calculations showed that the typical length scale over which the gas temperature in the wall (T_w) adjusts to differences within the solid temperature (T_f) is several orders of magnitude smaller than typical deposit layer thicknesses. Bissett presents this calculation in an internal report for General Motors (Bissett 1981). Therefore, they assume that the gas and the solid temperatures are equal, except at the inlet face of the deposit layer (y=0):

$$T_w=T_f, \quad (19)$$

where

$$T_w|_{y=0}=T_I. \quad (20)$$

With respect to the PM energy balance, they assume that heat losses to the surroundings are negligible due to proper insulation:

$$\rho_d c_d\frac{\partial T_{ff}}{\partial t}+\rho_w u_w c_p\frac{\partial T_f}{\partial y}=\frac{\partial}{\partial y}\left(\lambda_d\frac{\partial T}{\partial y}\right)-kS_p\left(\Delta H_{reac}/W_a\right)\rho_w X_{s,O_2} \quad (0<y<t_d). \quad (21)$$

Because they set the gas temperature in the deposit layer equal to the filter temperature, equating the solid and fluid phase energy equations results in the inclusion of the advection derivative as a function of the gas flow in this equation. Of importance, Bissett and Shadman state that their filter density and conductivity variables are bulk values that will include the influence of the porosity of the medium.

They write the wall energy balance similarly as

$$\rho_f c_f\frac{\partial T_f}{\partial t}+\rho_w u_w c_p\frac{\partial T_f}{\partial y}=\frac{\partial}{\partial y}\left(\rho_f\frac{\partial T_f}{\partial y}\right) \quad (t_d<y<t_m). \quad (22)$$

This model provides a method for computing the regeneration event of the filter and they use it to predict

the temperature profiles as a function of time with different PM loading amounts.

1.4 Bissett's channel model

Bissett (1984) follows up the previous effort by creating a model for the transport of nearly all thermodynamic variables through a wall-flow DPF while trying to avoid the complexities of multidimensional compressible fluid flow. He accomplishes this by representing the flow at each axial position in 1D and incorporating the proper physics for the flow to and from the wall system. In his article, Bissett makes the following assumptions:

- The properties of the gas entering the front face of the monolith are spatially uniform; however, they can be time dependent.
- The model assumes perfect insulation for the circumferential walls of the monolith.
- A single inlet and outlet channel represents the behavior of all inlet and outlet channels.
- He neglects radiative heat transport in the channels because the long thin channel walls have similar view factors and should have similar temperatures.
- The thickness of the PM layer is so thin compared with the channel thickness during the initial period of operation; the change in the channel geometry due to the presence of the PM layer can be neglected: $t_d << d$.
- The emitted particles do not interfere with the flow due to their low mass fraction within the bulk gas.
- Although not explicitly stated in his article, Bissett omits the time derivatives of the gaseous state variables, effectively stating that there is not any storage in the gas according to a quasi-steady-state approximation.

This effort becomes the definitive beginning to the channel flow DPF model with all extensions and adaptations basing themselves off this seminal article. This section describes the theory included in this article along with the assumptions made helping lead into the extensions presented by later authors.

1.4.1 Continuity equations

Bissett writes the mass equations for the channels as

$$\frac{\partial(\rho_I u_I)}{\partial z} = \frac{-4}{d}\rho_w u_w \text{ and } \frac{\partial(\rho_{II} u_{II})}{\partial z} = \frac{4}{d}\rho_w u_w, \tag{23}$$

where the subscripts *I* and *II* represent the inlet and outlet channels, respectively. In this equation, the terms on the right-hand side of the equation are a measure of the mass leaking and entering through the porous walls. In his article, Bissett uses only one average density, velocity, and pressure to describe the thermodynamic properties in the wall and PM layers as discussed prior. The following sections will indicate how to compute these values for this model.

1.4.2 Momentum equations

For the momentum equations through the channel, Bissett assumes that the gas flows only in the *z*-direction as it enters or exits the channel; hence, there is no transport of the *y*-component of momentum at the wall. However, because the no-slip condition holds at the walls in the *z*-direction, friction will occur. Bissett states that this variation should be very close to that observed when the walls are solid because only a very small fraction of the flow at each axial position passes through the wall:

$$\frac{\partial p_I}{\partial z} + \frac{\partial(\rho_I u_I^2)}{\partial z} = -F\frac{\mu u_I}{d^2} \text{ and } \frac{\partial p_{II}}{\partial z} + \frac{\partial(\rho_{II} u_{II}^2)}{\partial z} = -F\frac{\mu u_{II}}{d^2}. \tag{24}$$

A correlation for fully developed laminar flow in a square channel relates the constant (*F*) on the right-hand side to the local differential pressure. This simplified assumption has been addressed and withdrawn in a recent effort by Bissett et al. (2012) by solving the 3D boundary layer in the channel.

To simulate the pressure drop across the porous wall, Bissett uses Darcy's (1856) law and includes Forchheimer's (1901) modification to allow for the possibility of inertial flow effects caused by high velocities:

$$p_I - p_{II} = \left(\frac{\mu_w u_w}{K} + \beta\rho_w u_w^2\right)\left[t_f + \phi(t_d)\right], \tag{25}$$

where $\phi(t_d)$ is a function of the thickness of the deposit loaded on the filter. Although not expressly indicated in his article, this equation is an algebraic result of the momentum equation through the wall when employing Darcy's law. In his model, the ideal gas law is valid for the channels and the wall gases:

$$p_{atm} = \rho RT. \tag{26}$$

However, he uses atmospheric pressure instead of local pressure, because the assumption is that all pressure differences are small in comparison with the atmospheric pressure. Of particular note, the value for the average wall

velocity comes from the solution of Eq. (25), whereas the average wall density will come from the ideal gas law once making an assumption for temperature of the gas in the wall in the next section.

1.4.3 Energy equations

In the energy equations, because there is mass flowing through the walls, there will be transport of energy between the channels and the porous wall in addition to heat transfer between the gases and the wall. In Bissett's original article, he writes these equations as

$$\rho_I u_I c_p \frac{\partial T_I}{\partial z} = \frac{4}{d}\left[h_g - \rho_w u_w c_p\right]\left(T_f - T_I\right) \text{ and } \rho_{II} u_{II} c_p \frac{\partial T_{II}}{\partial z} = \frac{4}{d}\left[h_g + \rho_w u_w c_p\right]\left(T_f - T_{II}\right). \quad (27)$$

Bissett states that the formulation of his model neglects the thin heat transfer layer in the wall (essentially the boundary layer at the inlet channel interface and the wall) requiring all heat transfer to take place in the channels. As a result, the wall temperature is the equal temperature of both phases in the wall (gas as T_w and filter as T_f) and independent of the radial direction ($T_w = T_f$); it can still vary in the axial direction. Hence, by continuity, the wall temperature is also the temperature of the channel gas just outside the wall system. In addition, conduction is determined to be negligible relative to advective transport in the axial direction. However, because this is a 1D model, he states that an effective heat transfer coefficient (h_g) in this equation includes the contribution of conduction in the radial direction to effectively account for 2D effects.

1.4.4 Species equation and particle mass balance

Drawing from his earlier effort, Bissett restates the equation for the oxygen level in the PM layer as a balance between advection and reaction kinetics but writing now via mass fractions:

$$\frac{\partial\left(\rho_w u_w Y_{s,O_2}\right)}{\partial y} = -kS_p \rho_w Y_{s,O_2}. \quad (28)$$

This equation is needed to calculate the change in particle mass balance derived prior:

$$\rho_d \frac{\partial t_d}{\partial t} = -\left(W_{C_{(s)}}/W_{O_2}\right)\rho_w u_w Y_{I,O_2}\left[1 - \exp\left(-kS_p t_d/u_w\right)\right], \quad (29)$$

which is used in predicting the influence of exothermic reactions in the filter energy balance. Hence, although not expressly a 1+1D model, one can see the need to model in both the channel direction (z) and through the wall (y).

1.4.5 Filter energy balance

To calculate the temperature of the filter, Bissett uses the traditional heat diffusion equation writing it as a function of the thicknesses of the wall and PM. He assumes that these layers have the same temperature due to their proximity to each other and the fact that PM is present within the filter wall due to deep-bed filtration. The model includes the effects of conduction in the wall $\left(\dot{Q}_{cond}\right)$, the heat transfer from the gases in the channel $\left(\dot{Q}_{conv}\right)$, and the effects of PM oxidation on the energy of the wall $\left(\dot{Q}_{reac}\right)$:

$$\frac{\partial}{\partial t}\left[\left(\rho_f c_f t_f + \rho_d c_d t_d\right)T_f\right] = \dot{Q}_{cond} + \dot{Q}_{conv} + \dot{Q}_{reac} \quad (30)$$

It is important to note that Bissett did include a wall energy flux in the derivation $\left(\dot{Q}_{wall}\right)$ of this equation; however, the two resulting terms cancelled each other out, and consequently, the influence of wall energy flux is not included in the final equation. The authors will explain this flux omission and later inclusion in a later section.

Bissett's derivation of the conduction term in this energy equation allows for the impact of different PM thicknesses along the length of the filter:

$$\dot{Q}_{cond} = \lambda_d \frac{\partial}{\partial z}\left(t_d \frac{\partial T_f}{\partial z}\right) + \lambda_f t_f \frac{\partial^2 T_f}{\partial z^2}. \quad (31)$$

The heat transfer to the filter wall balances according with the channel energy equations (Eq. 27),

$$\dot{Q}_{conv} = -h_g\left(T_f - T_I\right) - h_g\left(T_f - T_{II}\right), \quad (32)$$

and the effects of PM oxidation include the updated derived effort of Eq. (18) to Eq. (29):

$$\dot{Q}_{reac} = -\left(\Delta H_{reac}/W_{O_2}\right)\rho_w u_w Y_{I,O_2}\left[1 - \exp\left(-kS_p t_d/u_w\right)\right], \quad (33)$$

where ΔH_{reac} is the heat of reaction of the carbon oxidation reaction (Eq. 13).

Bissett's model can simulate complete PM regeneration events and calculate the time change of filter temperature as shown in Figure 9. As mentioned previously, this work is of prime importance to the DPF modeling community and its importance has been widely recognized in the technical literature. In the next section, another article by

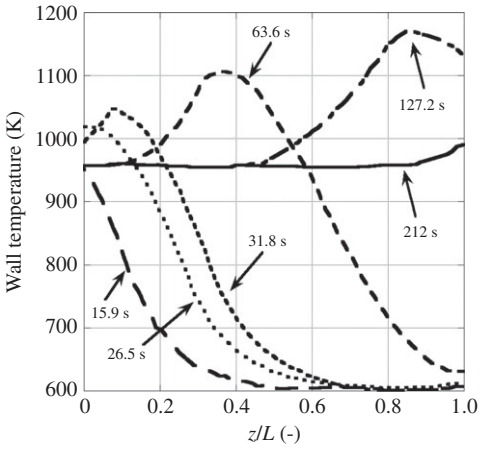

Figure 9 Profiles of wall temperature as a function of dimensionless axial distance at selected times (Bissett 1984).

Bissett describes the flow through the filter PM and wall layers in more detail. This work will eventually merge into the channel wall model right after the turn of the century.

2 Updated model equations

Bissett and Shadman published two seminal articles in the DPF modeling community of which most others base their efforts. In this section, the authors indicate those who expanded the model to account for area conservation, NO_2 passive regeneration, catalyzed filters, and multidimensional effects. Because the two models have undergone a merging into one, this article presents these sections according to the governing equations of flow making little distinction between the versions. For example, the next section presents the mass equations for the PM and wall layers alongside those for the channel equations. In addition, each area illustrates a brief historical summary of who modified the equations and why they revised them.

2.1 Continuity equations

The assumption of changes in channel geometry due to PM layer loading was revisited by Peters et al. (Peters 2003, Peters et al. 2004), Haralampous et al. (Haralampous and Koltsakis 2004a,b, Haralampous et al. 2004a,d,e), and recently by Depcik and Assanis (Depcik and Assanis 2008, Depcik 2010). In particular, these works reflect a consideration of Bissett's original concept that the thickness of the PM layer does not influence the flow properties (1984 article, assumption #5). To do so, the Peters et al. articles use different velocities to represent the lateral components through the PM layer and the porous filter wall, respectively; that is, they use one average velocity for the PM layer (u_s) and one average velocity for the wall layer (u_w). However, Haralampous et al. only use one average velocity for both layers (u_w), similar to the original efforts of Bissett, but instead add a function to the species equations to account for the change in cross-sectional area that the flow encounters through these layers. Depcik and Assanis take a slightly different approach by modeling the velocity profile through both layers as a function of distance: u_s, $u_w=f(y)$.

Peters et al. describe the continuity equations for square channels as

$$\frac{\partial\left(\rho_I u_I d_I^2\right)}{\partial z}=-4d_I\rho_I u_s \text{ and } \frac{\partial\left(\rho_{II} u_{II} d_{II}^2\right)}{\partial z}=4d_{II}\rho_{II}u_w\,. \qquad (34)$$

When applying continuity to the mass flow entering the PM layer and leaving the porous wall into the outlet channel, they recover the following equation for the velocities:

$$u_w=u_s\frac{\rho_I d_I}{\rho_{II}d_{II}}\,, \qquad (35)$$

with the effective hydraulic diameters now computed as

$$d_I=d\text{-}2t_d \text{ and } d_{II}=d. \qquad (36)$$

In this model, the right-hand side of the continuity equation uses the inlet density leaving the inlet channel; for the outlet channel, they use the outlet channel density entering from the wall. According to the classic model, this does not correspond correctly to the system because the density at the interface of the wall can have a different value than the channels. A discussion of this concept occurs later in this article illustrating how to either compute the density as a function of a local thermodynamic equilibrium or use an average pressure across these layers.

In the Peters et al. articles, the surface areas per unit length in the inlet and outlet channels equations are different because of the smaller gaseous control volume in the inlet channel when PM is present:

$$S_I=4d_I \text{ and } S_{II}=4d_{II}. \qquad (37)$$

A physical property that must be met by all models is that there should not be any mass storage in the PM or wall layers during steady-state conditions: ($\partial\rho_s/\partial t=0$) and ($\partial\rho_w/\partial t=0$). Because Eq. (36) relates the velocities, the mass flux source terms cancel out and the model does not violate any mass conservation laws. However,

because of the erroneous use of channel densities on the right-hand side in the continuity equation, the authors do not explore this article further, but its importance is noted.

The Haralampous et al. articles indicate the use of the proper density, but their model does not make a distinction between the surface areas per unit length of the two channels:

$$\frac{\partial\left(\rho_I u_I d_I^2\right)}{\partial z}=-4d\rho_w u_w \text{ and } \frac{\partial\left(\rho_{II} u_{II} d_{II}^2\right)}{\partial z}=4d\rho_w u_w. \quad (38)$$

When using different surface areas for the inlet and outlet channels when PM is present, to balance the mass fluxes, the density, velocity, or density times velocity must change in the PM and wall layers. This allows different mass flux values for the inlet and outlet channels to account for the dissimilar surface areas while not causing mass accumulation within the wall. Although Peters et al. did not use boundary conditions *per se*, they did use different wall velocities for the PM and wall layers to account for the different surface areas. In the Haralampous et al. articles, because they only use one average value for the density (ρ_w) and velocity (u_w) to describe the properties through the wall and soot layers, using the same surface area prevents mass accumulation.

In the Depcik and Assanis articles, the flow equations are formulated in the area-conserved format often used for converging-diverging nozzles (Roe 1986, Lee 1992) and the intake and exhaust of internal combustion engines (Liu et al. 1996, Onorati et al. 1999), often called quasi 1D flow. The thermodynamic properties through the PM and wall layers can change and are calculated according to the Navier-Stokes equations of motion. As a result, the equations of mass for square channels incorporating different surface areas are

$$\frac{\partial\left(\rho_I u_I d_I^2\right)}{\partial z}=-4d_I\rho_s u_s \text{ and } \frac{\partial\left(\rho_{II} u_{II} d_{II}^2\right)}{\partial z}=4d_{II}\rho_w u_w. \quad (39)$$

In this version, for the inlet channel equations, the density and velocity of the gas in the PM layer used in the flux term are evaluated at the interface: $\rho_s u_s|_{y=0}$. For the outlet channel equations, the density and velocity of the gas in the wall layer used in the flux term are also evaluated at the interface: $\rho_w u_w\big|_{y=t_m+t_d}$. Although the area-conserved formulation is not necessary for the outlet channel, writing the equations in this manner allows for different geometries to be used similar to work previously accomplished by Konstandopoulos et al. (2003b, 2005). The area-conserved format more accurately tracks

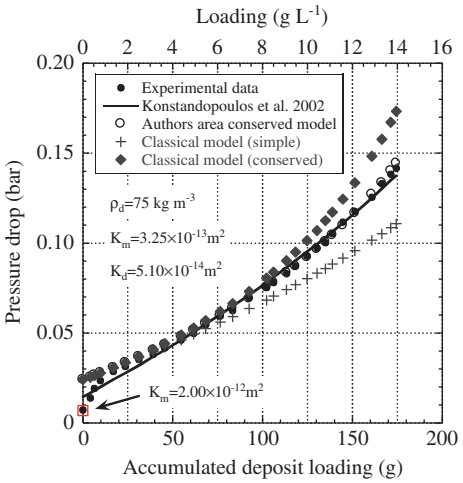

Figure 10 Comparison of area-conserved model with classic formulation (Depcik and Assanis 2008).

mass conservation in situations of varying geometry and matches the experimental data better in situations of medium to heavy loading events as shown in Figure 10.

At this stage of the article, it is necessary to explain the methodology for the rest of this document. As indicated in the previous paragraphs, there are two fundamental derivations in the literature. One approach uses a singular average velocity and density for the PM and wall layers, whereas another tactic is to generate a profile for these variables. The difference between the two models relates to a tradeoff between accuracy and computational cost. To be complete, the rest of this article presents both model formulations.

The equation for continuity in the wall originally described by Bissett and Shadman in Eq. (10) was later expanded by Haralampous and Koltsakis (2002). In this article, they eliminate the original assumption regarding the omission of the reactant mass added to the gas phase from the combustion of deposit:

$$\frac{\partial\left(\rho_w u_w\right)}{\partial y}=\dot{S}_{mass}, \quad (40)$$

where the term on the right-hand side accounts for the mass of product gases added to the flow from PM combustion.

In the Depcik and Assanis formulation, the flow is no longer 1D due to the varying cross-sectional area through the layer. Because area conservation is a methodology for incorporating multidimensional effects without having to include the other dimensions in the solution algorithm, the PM layer equation becomes

$$\frac{\partial(\rho_s u_s A_s)}{\partial y} = A_s \dot{S}_{mass}. \quad (41)$$

The change in nomenclature here stems from the fact that the Haralampous and Koltsakis article does not differentiate the gas properties between the PM and the wall layer (besides the chemical species), whereas mass equations are written for the PM and the wall layers in the Depcik and Assanis articles.

For square channels, the change in cross-sectional area per unit length through the PM layer can be determined from Figure 5:

$$A_s = 4\left[d - 2\left(t_d - \frac{y}{\tan\theta}\right)\right], \text{ where } \tan\theta = 1 \quad (42)$$

and the instantaneous change the cross-sectional area comes from the derivative of this value with respect to the distance through the PM layer; that is, $dA_s/dy = 8$. For different channel geometries, it is relatively easy to replace A_s and its derivative with the respective new values while maintaining the same visual identity of the governing equations.

Although the cross-sectional area that the flow sees is constant in the wall layer, writing the mass equation in an area-conserved format allows for continuity with the other equations:

$$\frac{d(\rho_w u_w A_w)}{dy} = 0, \quad (43)$$

where $A_w = 4d$. On inspection of the mass equations in the channel Eq. (39), the mass flux terms do cancel each other out similar to the before mentioned references. Although the properties in the PM and wall layers change, they must remain consistent with the governing equations of mass in each respective layer. In all cases, the time derivatives of the variables are neglected, which is a reasonable assumption as long as the time scales in the problem are a function of the filter and not the bulk gas (Depcik and Assanis 2005).

With respect to the original assumptions of Bissett and Shadman in their 1985 article, Depcik and Assanis found that not including the mass source term in Eq. (40) or Eq. (41) results in a small error of approximately 6% in the mass flow rate and 1% in the final deposit mass during an experimental test involving PM oxidation. They also found that, in the cases of heavy PM loading of the filter, the wall velocity could change throughout the wall by up to 20%. However, in the cases of light to moderate loading under which most DPF filters see operation, as illustrated in Figure 11, the velocity of the gas through the wall does not vary significantly, indicating that the singular velocity model of Haralampous et al. will not generate appreciably different results.

Focusing on the variable filtration area per unit length variable A_s, three cases can be identified. When t_d/d is close to zero, no variability needs to be taken into account (Bissett and Shadman 1985). In the range of $t_d/d << 1$, a "quasi 1D flow" can be assumed in a thin cake with the variable filtration area useful in modeling activities. Finally, the case of $t_d/d = O(1)$ corresponds to filter clogging conditions. Inside the cake, the assumption of quasi 1D flow will be less accurate due to the velocity components perpendicular to wall velocity. Most important during this situation is that the axial flow friction increases significantly, pressure and density may vary considerably inside the cake, and the surface of the cake may deviate from the rectangular shape. These conditions are increasingly difficult to model accurately and simulation results, although useful, must be treated with caution.

2.2 Momentum equations

Similar to the continuity equations, the momentum equation in the channel remained constant from Bissett's

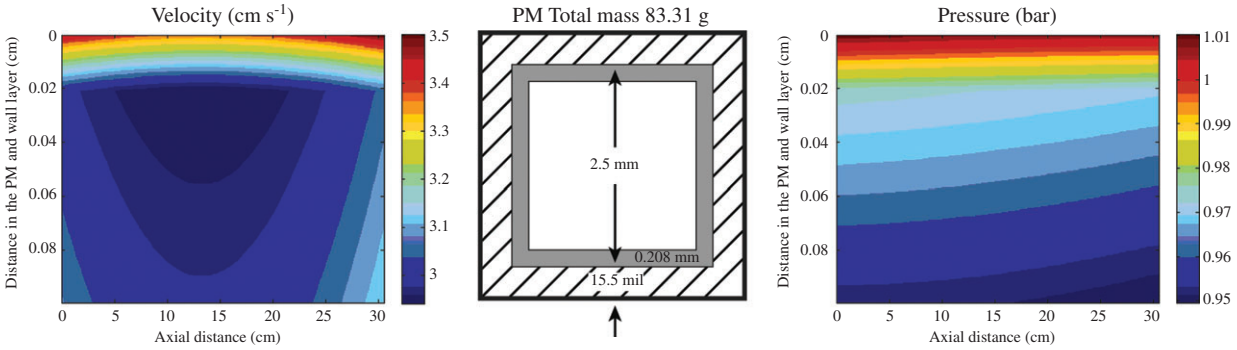

Figure 11 Velocity and pressure in PM and wall layers under moderate loading (Depcik and Assanis 2008).

formulation until Peters et al. and Haralampous et al. revisited the change in channel volume due to PM loading. The Haralampous et al. model incorporates the change in geometry only in the frictional component on the right-hand side of the equation through the effective channel diameter:

$$\frac{\partial p_I}{\partial z}+\frac{\partial\left(\rho_I u_I^2\right)}{\partial z}=-F\frac{\mu u_I}{d_I^2} \text{ and } \frac{\partial p_{II}}{\partial z}+\frac{\partial\left(\rho_{II} u_{II}^2\right)}{\partial z}=-F\frac{\mu u_{II}}{d_{II}^2}. \quad (44)$$

In the Depcik and Assanis model, the equations resemble those used in area-conserved, 1D flow (Liu et al. 1996, Onorati et al. 1999, Depcik et al. 2005):

$$\frac{\partial\left(\rho_I u_I^2 d_I^2\right)}{\partial z}+\frac{\partial\left(p_I d_I^2\right)}{\partial z}=-F\mu u_I+p_I\frac{d\left(d_I^2\right)}{dz} \quad (45)$$

$$\frac{\partial\left(\rho_{II} u_{II}^2 d_{II}^2\right)}{\partial z}+\frac{\partial\left(p_{II} d_{II}^2\right)}{\partial z}=-F\mu u_{II}+p_{II}\frac{d\left(d_{II}^2\right)}{dz}. \quad (46)$$

Writing the above equations in this form requires including an additional term on the right-hand side to balance the forces. Expanding the derivatives recovers the same equations of Haralampous et al. when assuming the change in PM thickness in the z-direction is negligible: $dt_d/dz \approx 0$. It is important to note that keeping the area terms in the derivatives and solving the governing equations as indicated is more accurate with respect to mass conservation (Roe 1986, Liu et al. 1996, Onorati et al. 1999).

Konstandopoulos et al. (2000) revisited the momentum equation through the PM and wall layers by adding the effects of variable area within the PM layer. This was expressed the following year in a manner similar to Bissett's work through an algebraic formulation (Konstandopoulos et al. 2001):

$$p_I - p_{II}=\frac{\mu u_w}{\mathrm{K}_f}t_f+\beta_m\rho_w u_w^2 t_f+\frac{\mu u_w}{2\mathrm{K}_d}d\ln\left(\frac{d}{d_I}\right). \quad (47)$$

The traditional model for pressure drop can still be seen (Mohammed et al. 2006) as well as other variants (Haralampous et al. 2004d,e, Peters et al. 2004):

$$p_I - p_{II}=\frac{\mu u_w}{\mathrm{K}_f}t_f+\frac{R_u T_f}{\hat{W}p_w}\frac{\mu d\rho_w u_w}{2\mathrm{K}'_d}\ln\left(\frac{d}{d_I}\right), \quad (48)$$

where the effective PM permeability is a function of the local mean free path length:

$$\mathrm{K}'_d=\mathrm{K}_d\left(1+c\mu\frac{p_0}{p_w}\sqrt{\frac{T_f}{\hat{W}}}\right), \quad (49)$$

where c is the slip flow correction factor and p_0 is the reference pressure for apparent permeability. The discussion of this equation and the impact of mean free path length will come in a later section of this article, which presents a historical summary of the calculation of appropriate permeability for the momentum equation.

In these approaches, the derived algebraic equation for the pressure drop comes from solving the momentum equation. Following Wooding (1957) and Brinkman (1947a,b), a theorized extension of the Navier-Stokes momentum equation to porous media involves the use of an effective viscosity to account for the diffusion of velocity. However, for many practical purposes, there is no need to include this viscous term (Nield and Bejan 2006). In addition, Beck (1972) found that the inclusion of the advection term, $\partial(\rho u^2)/\partial y$, is erroneous when Darcy's law is employed. Depcik and Assanis include these concepts in formulating their area-conserved PM and wall momentum equations:

$$\frac{d\left(p_s A_s\right)}{dy}=p_s\frac{dA_s}{dy}-\frac{\mu u_s A_s}{\mathrm{K}_d}-\beta_d\rho_s A_s u_s^2 \quad (50)$$

$$\frac{d\left(p_w A_w\right)}{dy}=p_w\frac{dA_w}{dy}-\frac{\mu u_w A_w}{\mathrm{K}_f}-\beta_m\rho_w A_w u_w^2. \quad (51)$$

Again, it is important to note that the area change term on the right-hand side allows a balance in the pressure forces when writing in this format. Expanding the derivative of the pressure force recovers the equations of Konstandopoulos et al. and Haralampous et al. but written as a differential as required by Depcik and Assanis's numerical scheme explained later. As a result, the choice of methodology depends on the requirements of the modeler within their computational framework.

2.3 Energy equations

For the energy equations in the channel, there is some discrepancy in the literature on how to write the governing equations. Because there is mass flowing through the walls, there will be a transport of energy from the inlet channel to the porous wall in addition to convective heat transfer; another relative term is present for the outlet channel. In Bissett's article, he neglects the thin heat transfer layer in the wall requiring all heat transfer to take place in the channels. As a result, the filter temperature (T_f) is the equal temperature of both phases in the wall and independent of the radial direction, but it can still vary in

the axial direction. In 1997, Bissett's original energy equations were modified by Koltsakis and Stamatelos (1997a,b) illustrating a change to the inlet channel equation:

$$\rho_I u_I c_p \frac{\partial T_I}{\partial z} = \frac{4}{d_I} h_g \left(T_f - T_I\right). \tag{52}$$

However, no discussion is noted regarding this discrepancy, and in the same year, the original equation of Bissett is published by the same authors (Koltsakis and Stamatelos 1997a,b). This inconsistency is again seen in an article by Konstandopoulos et al. (2001) through a derivation of these equations using a continuum description of the filter formulated from a multidimensional model of a DPF.

A later multidimensional article by Kostoglou et al. (2003) referencing this 2001 article discusses this inconsistency. In this article, for a perimeter-averaged 1D approach for the temperature field in the channel (e.g., volume-averaged mixing cup temperature), the cross-sectional temperature distribution of the channel no longer enters the problem and the gas entering the porous medium assumes a temperature equal to T_I. This gas quickly goes to thermal equilibrium with the porous wall and exits into the outlet channel with the filter temperature T_f. They note that the difference between the models is small for most practical cases; however, the older model can lead to some unphysical behavior in some circumstances. Other efforts by Konstandopoulos et al. (2005) revisit this difference, but no definitive conclusion is reached.

The recent work by Depcik and Assanis revisits these equations through their area-conserved derivation. The full formulation of energy equations includes the effects of kinetic energy in the internal energy and enthalpy terms; however, these kinetic energy terms are small in comparison and can be eliminated; $u^2 << h$. The articles by Kostoglou et al. (2003) and Konstandopoulos et al. (2005) assume that the gas entering the porous medium is assumed to have a temperature equal to T_I. However, instead of using this assumption, Depcik and Assanis solve the gas temperature in the PM and wall equations as a function of the governing equations of flow accordingly; that is, T_s at y=0, the inlet channel and PM interface, is computed in deference to assuming this value as T_I. This will then solve for the thermal heat transfer layer allowing for continuity between the channel gas temperatures and the gas in the different layers. In other words, this model imposes thermal equilibrium at the surface according to the first law of thermodynamics as illustrated later in the boundary conditions section. As a result, the channel equations are

$$\frac{\partial\left(\rho_I u_I h_I d_I^2\right)}{\partial z} = 4 d_I \left[h_g \left(T_s - T_I\right) - \rho_s u_s h_I\right] \tag{53}$$

$$\frac{\partial\left(\rho_{II} u_{II} h_{II} d_{II}^2\right)}{\partial z} = 4 d_{II} \left[h_g \left(T_w - T_{II}\right) + \rho_w u_w h_w\right], \tag{54}$$

where the equations write the heat transfer term as a function of the local gas temperature of the PM (T_s) and wall layers (T_w).

By expanding the derivatives, using the definition of constant pressure specific heats, $\partial h/\partial z = c_p(\partial T/\partial z)$, and incorporating mass Eq. (39), the model produces the same result for the energy equations as the articles by Koltsakis and Stamatelos for the inlet channel:

$$\rho_I u_I c_p \frac{dT_I}{dz} = \frac{4}{d_I} h_g \left(T_s - T_I\right). \tag{55}$$

For the outlet channel, performing the same analysis results in a similar equation with the difference of using enthalpy terms in the second term on the right-hand side:

$$\rho_{II} u_{II} c_p \frac{dT_{II}}{dz} = \frac{4}{d_{II}} \left[h_g \left(T_w - T_{II}\right) + \rho_w u_w \left(h_w - h_{II}\right)\right]. \tag{56}$$

Often, researchers write this second term as the constant pressure-specific heat times a temperature difference: $\rho_w u_w c_p (T_w - T_{II})$. However, when using chemical species including their associated heats of formation, the constant pressure-specific heats will be dissimilar. This will occur under reacting conditions, such as a catalyzed wall, with significant composition changes. As Figure 12 illustrates, using the constant pressure assumption results in under predicting PM conversion during a cool down and oxidation test by 3%.

Because the channels are undergoing a relative loss and gain of mass with an accompanying flow rate, there exists a possibility that the heat transfer coefficients between the channel gas and wall are affected. Konstandopoulos et al. (2005) present a fundamental analysis to determine the impact of suction and injection on the heat transfer coefficients in the channels, but they do not generate a result for use in the channel model. Follow-up efforts by Depcik and Assanis using the one-porous wall literature created both square and circular fully developed Nusselt number correlations based on the flow Peclet number through the wall. Current efforts by Bissett et al. (2012) revisit this model and formulate pertinent four-porous wall expressions for wall-flow particulate filter modeling requirements.

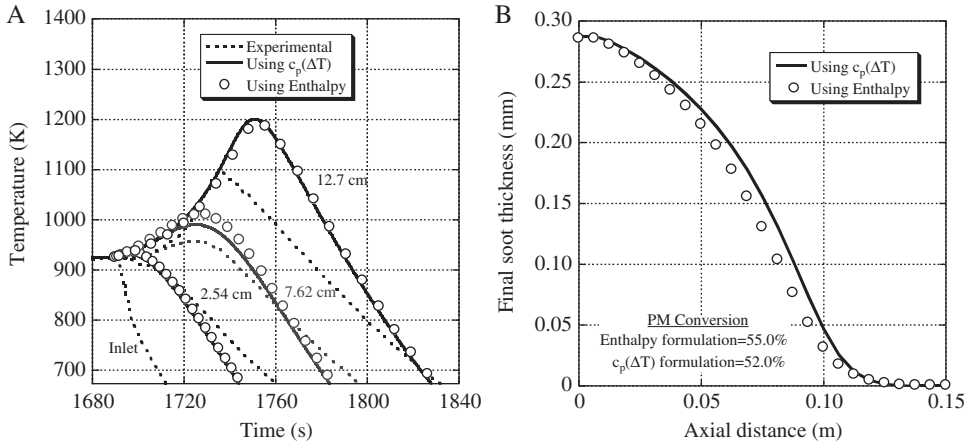

Figure 12 Comparing the use of $c_p(\Delta T)$ for enthalpy with actual enthalpy in energy equations (Depcik 2010).

To conclude their model development, Depcik and Assanis model the gas temperature in the PM and wall layers. Again, because the kinetic energy of the gas in the wall is much smaller than its enthalpy $\left(h_w \gg u_w^2\right)$, the following equations for the energy of the gas in the PM and wall layers can be written as (Calmidi and Mahajan 2000, Ingham et al. 2004, Zhao et al. 2004, Lu et al. 2006)

$$\frac{\partial\left(\rho_s u_s h_s A_s\right)}{\partial y}-\frac{\partial}{\partial y}\left(\lambda_s^{\star} A_s \frac{\partial T_s}{\partial y}\right)=\frac{h_c A_s \tilde{a}}{\varepsilon_p}\left(T_f-T_s\right) \tag{57}$$

$$\frac{\partial\left(\rho_w u_w h_w A_w\right)}{\partial y}-\frac{\partial}{\partial y}\left(\lambda_w^{\star} A_w \frac{\partial T_w}{\partial y}\right)=\frac{h_c A_w \tilde{a}}{\varepsilon_p}\left(T_f-T_w\right). \tag{58}$$

In these equations, the close proximity of the filter affects the thermal conductivity of the fluid in the porous layers and, as a result, requires an effective thermal conductivity calculation. The calculation of which is described for metal foams by Boomsma and Poulikakos (2001). Because no fundamental models of effective conductivity exist for DPF purposes, Depcik and Assanis use the metal foam formulation in their article (see also Lu et al. 2006 for more information on its application).

The term on the right-hand side accounts for the heat transfer between the filter and the gas in each respective layer. It has been stated that the calculation of the heat transfer coefficient (h_c) is difficult to measure (Ingham et al. 2004); however, two correlations exist in the literature served as an approximate upper and lower bounds. In the situation where the filter wall is packed full of PM and a cake layer exists in the inlet channel, Depcik and Assanis theorize that the heat transfer will be analogous to a packed bed reactor with a representative heat transfer coefficient found using a reference by Wakao et al. (1979). When the filter is empty, they use a correlation developed by Zukauskas (1987) for staggered cylinders used in heat transfer studies for metal foams. This correlation should give a heat transfer coefficient smaller than actual due to the high porosity of the metal foams compared with a DPF filter wall.

To check the assumption that the gas temperature in the wall instantly assumes the filter temperature, Depcik and Assanis ran a sample simulation artificially raising the inlet gas temperature while holding the filter wall at a constant lower temperature. When comparing the magnitudes of the three terms in Eqs. (57) and (58), they calculate the magnitude of convection to advection to be approximately 10^5, whereas the magnitude of convection to conduction is about 10^4. This illustrates that convection dominates the mode of heat transfer in the wall validating the common assumption that $T_s=T_w=T_f$. As a result, incorporating this finding in Eqs. (55) and (56) will result in Eq. (52) for the inlet channel and Eq. (27) for the outlet channel when making the assumption of constant pressure specific heats.

In a recent article from Bissett et al. (2012), the authors solve the boundary layer equations for mass, momentum, and energy in the square channel with the aim to derive appropriate "film" heat transfer coefficients. They solve their equations using a boundary condition of fixed temperature at the channel/wall interface (T_f via the nomenclature in this article). The authors imply that this temperature value used in the boundary could be considered equal to the solid wall temperature due to the extremely efficient heat transfer between gas/wall in the solid phase. However, the gas temperature will become equal to the wall temperature only as a result of heat

transfer inside the wall. At the channel/wall boundary, the gas temperature will assume a different temperature. Therefore, the derivation of transport coefficients in the work of Bissett et al. (2012) is indeed valid for the case of fixed gas temperature at the channel/wall boundary; however, this temperature is not a priori known in the standard formulation of the DPF model equations. The use of the solid wall temperature in the fixed temperature boundary condition is only acceptable when the "no-slip" condition is valid, which is not the case in the DPF porous wall case.

Note that the Nu number is subject to the selection of the boundary condition even in the simpler case of flows in closed parallel ducts (no-slip condition). For example, the Nu number in square ducts is 3.61 in the case of uniform heat flux boundary condition in contrast to the typically used value of 2.98 for the case of fixed wall temperature. This is to emphasize the importance of the proper inclusion of the boundary condition when trying to derive global heat transfer coefficients, suggesting that a deeper investigation of the boundary layer problem with the inclusion of the wall domain would be worth study in the future (Sahraoui and Kaviany 1994, Ochoa-Tapia and Whitaker 1997, Depcik and Assanis 2008, d'Hueppe et al. 2011). In the meantime, the use of the standard Nu number for closed ducts is justified by the conceptual assumption that the portion of the flow that is not sucked through the porous wall exchanges convective heat with the wall surface as if the wall is nonporous.

2.4 Species equations

A few years after Bissett, Garner and Dent (1988) developed a model applicable to both fibrous and porous wall DPFs. This model incorporates medium porosity and, more importantly, an equation for the oxygen transport to the particulate surface and its subsequent consumption:

$$\varepsilon_p \rho_I \left(\frac{\partial Y_{I,O_2}}{\partial t} + u_I \frac{\partial Y_{I,O_2}}{\partial z} \right) = -k \rho_w Y_{w,O_2}. \quad (59)$$

This equation is reminiscent of the Euler species equation that can replace Bissett's constant O_2 mole fraction assumption. However, researchers never include it along with the classic model formulation.

At the same time, Cooper and Thoss (1989) find that NO_2 present in the exhaust is also effective at oxidizing the particulate at a significantly reduced temperature level versus oxygen (~250°C vs. 550°C). In their work, they theorize a two-equation reaction mechanism for conversion of particulates to partial and complete products of combustion:

$$C_{(s)} + NO_2 \rightarrow NO + CO \quad (60)$$

$$CO + NO_2 \rightarrow NO + CO_2. \quad (61)$$

The use of NO_2 to combust the particulate is adapted a number of years later by Hawker et al. (1997) through the design of an upstream catalyst for the oxidation of NO to NO_2 to make use of its lower temperature DPF regeneration characteristics. Because diesel exhaust consists mainly of NO (Heywood 1988), an oxidation catalyst (typically platinum based) is needed to form NO_2. They later use this catalyst for continuously regenerated DPF operation in which deposit is constantly being regenerated by NO_2 during its operation (Hawker et al. 1998).

At the same time, Ahlström and Odenbrand (1989) find that PM does not proceed completely toward complete combustion in an oxidative environment. This is later collaborated by Aoki et al. (1993) when they find that a significant portion of the exhaust flow measured out of the DPF shows the formation of CO as illustrated by Figure 13. As a result, they write the particulate combustion reaction as

$$C_{(s)} + (1-\alpha_1/2)O_2 \rightarrow (1-\alpha_1)CO_2 + \alpha_1 CO \quad (62)$$

with an experimentally determined α_1 between a third and a quarter.

Koltsakis and Stamatelos (1996a,b) further explore incomplete deposit oxidation and formulate the commonly used chemical balance:

$$C_{(s)} + \alpha_1 O_2 \rightarrow 2(\alpha_1 - 0.5)CO_2 + 2(1-\alpha_1)CO, \quad (63)$$

where α_1 is an index of completeness of the reaction. Typical values in the literature range between 0.8 and 0.9

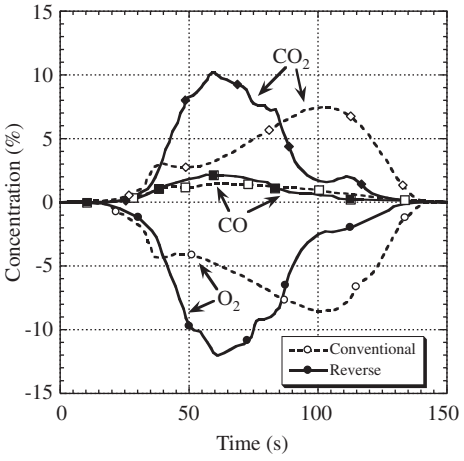

Figure 13 Comparison between conventional and reverse regenerations with regard to exhaust emissions (Aoki et al. 1993).

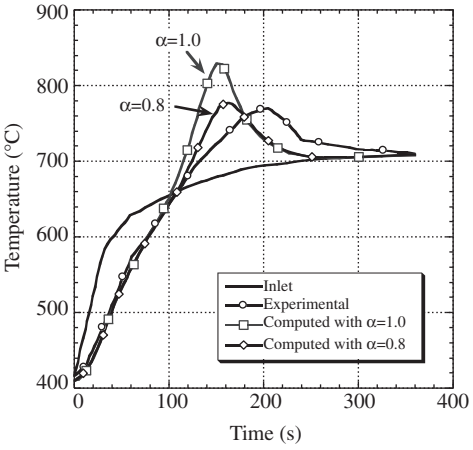

Figure 14 Influence of incomplete PM oxidation on model results (Aoki et al. 1993; Koltsakis and Stamatelos 1996a,b).

with a sample effect due to this index illustrated in Figure 14 (Aoki et al. 1993, Koltsakis and Stamatelos 1996a,b). To consider this in the model, they expand the surface species equation of Bissett [(Eq. 28)] to include this partial oxidation factor as follows:

$$\frac{\partial\left(\rho_w u_w Y_{s,O_2}\right)}{\partial y} = -\alpha_1 k_1 S_p \rho_w Y_{s,O_2}. \tag{64}$$

In another article, they use this formulation to model the catalytically induced regeneration of the PM by metal oxides (Koltsakis and Stamatelos 1996a,b).

In the following year, Jørgensen and Sorenson (1997) develop a combustion model through the PM layer that includes the effects of temperature, concentrations, velocity, and diffusion. This two-film model calculates the species and temperature profiles as a function of a flame sheet where PM oxidation occurs. In their article, they write species equations for O_2, CO, and CO_2. The important facet to take away is the incorporation of Fick's law into modeling the governing species equations through these layers. However, they accomplish this as a function of a flame sheet interpretation that does not lend itself to merging with the classic Bissett model.

Konstandopoulos and Kostoglou (1999) present the first article where the channel equations are shown at the same time as the species equations through the PM and wall layers (see also Konstandopoulos and Kostoglou 2000). However, the merging of the models has yet to occur, because the channel species equations are not present. They do expand the wall species equations by adding catalytic coating oxidation of PM to the model in multiple layers as illustrated in Figure 15. The PM layer is divided into two sections, with one layer (layer I) reacting catalytically and noncatalytically through a partial fraction and the other portion (layer II) sitting on top of the catalytic layer following the traditional thermal oxidation pathway. They also describe catalytic additive assisted oxidation of the PM with compounds either added in the fuel or sprayed in the exhaust by using a variable factor as a function of catalytic additive doses.

Extending their earlier modeling work, Konstandopoulos et al. (2000) begin to account for NO_2-assisted regeneration according to the following oxidation reaction:

$$C_{(s)} + (2-\alpha_2)NO_2 \rightarrow (2-\alpha_2)NO + \alpha_2 CO + (1-\alpha_2)CO_2. \tag{65}$$

This reaction is similarly expressed by Kandylas et al. (2002) based on the work of Jacquot et al. (2002):

$$C_{(s)} + \alpha_2 NO_2 \rightarrow \alpha_2 NO + (2-\alpha_2)CO + (\alpha_2-1)CO_2. \tag{66}$$

Through numerous engine experiments, they find that α_2 is usually in the range of 1.65 to 1.75.

The governing equation for layer II for NO_2 oxidation is similar to O_2 of Eq. (64):

$$\frac{\partial\left(\rho_w u_w Y_{w,NO_2}\right)}{\partial y} = -\alpha_2 k_2 S_p \rho_w Y_{w,NO_2}. \tag{67}$$

Layer I now includes the additional production of NO_2 from NO and O_2 because of the catalytic wash coat material:

$$\frac{\partial\left(\rho_s u_s \mathbf{Y}_s\right)}{\partial y} = \dot{\mathbf{S}}_s + \dot{\mathbf{R}}\mathbf{W}, \tag{68}$$

where the bold nomenclature indicates an array of species (O_2 and NO_2), $\dot{\mathbf{S}}_s$ is an array of PM conversion in this layer (O_2=catalytic and thermal oxidation and NO_2=thermal

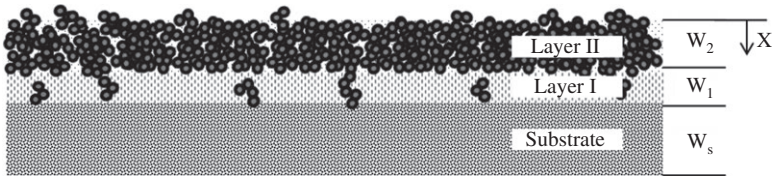

Figure 15 Konstandopoulos and Kostoglou's (1999) two-layer model.

oxidation), and $\dot{\mathbf{R}}$ is an array that accounts for gaseous catalytic reactions via the NO oxidation reaction (O_2=loss and NO_2=gain). They obtain the local NO mole fraction from nitrogen atom conservation.

It is not until the Peters et al. (Peters 2003, Peters et al. 2004) and Haralampous et al. articles (Haralampous et al. 2003, 2004a,b,c,d,e, Haralampous and Koltsakis 2004a,b) that the literature illustrates a merging of two models: channel and wall. These authors decide to include the wall species equations into the overall formulation instead of solving them separately. They accomplish this to provide the proper boundary conditions for the species equations in the channel with the Haralampous et al. version shown here:

$$\frac{\partial(u_I\mathbf{Y}_I)}{\partial z}=-\frac{u_w\mathbf{Y}_I}{df_y^2}+\frac{k_m(\mathbf{Y}_s-\mathbf{Y}_I)}{df_y} \tag{69}$$

$$\frac{\partial(u_{II}\mathbf{Y}_{II})}{\partial z}=\frac{u_w\mathbf{Y}_w}{df_y^2}+\frac{k_m(\mathbf{Y}_w-\mathbf{Y}_{II})}{df_y}, \tag{70}$$

where a geometrical parameter is defined as

$$f_y=\frac{b(y)}{d}. \tag{71}$$

The width available to the flow, $b(y)$, varies in the particulate layer and remains constant in the wall:

$$b(y)=\begin{cases} d+2y, & 0\le y\le t_d \\ d, & t_d\le y\le t_d+t_f \end{cases}. \tag{72}$$

Note, for this model, that $\mathbf{Y}_s$ is the array of species evaluated at y=0 and $\mathbf{Y}_w$ is the array of species evaluated at $y=t_m+t_d$. They include the effects of diffusing species to and from the channel to the wall similar to catalyst modeling (Depcik and Assanis 2005). This is because they find that the mass-transfer coefficients can be on the same order of magnitude as the wall-flow velocity. In comparison, recent work by Depcik uses the species equations for the channel via a concentration format instead of mass fractions:

$$\frac{\partial(\rho_I u_I\mathbf{Y}_I d_I^2)}{\partial z}=-4d_I\left[\rho_s u_s\mathbf{Y}_I-k_m(\rho_s\mathbf{Y}_s-\rho_I\mathbf{Y}_I)\right] \tag{73}$$

$$\frac{\partial(\rho_{II}u_{II}\mathbf{Y}_{II}d_{II}^2)}{\partial z}=4d_{II}\left[\rho_w u_w\mathbf{Y}_w+k_m(\rho_w\mathbf{Y}_w-\rho_{II}\mathbf{Y}_{II})\right]. \tag{74}$$

This use of concentration equations ensures that the equations properly conform to the mass equations presented earlier. This can be seen by summing both sides of the equations, taking into account that the sum of mass fractions equals one and using the dilute mixture simplification that is common in catalyst modeling (Koltsakis and Stamatelos 1997a,b). Specifically, this assumption states that the summation of the diffusing gas species concentration difference terms is too low to affect the overall mass balance of the carrier gas: $\sum k_m(\rho_I\mathbf{Y}_I-\rho_s\mathbf{Y}_s)\approx 0$ and $\sum k_m(\rho_{II}\mathbf{Y}_{II}-\rho_w\mathbf{Y}_w)\approx 0$. However, Figure 16 illustrates that Depcik found this term to be important because of the open system architecture of the channels. As a result, it should be included in the mass equations via a summation term on the right-hand side of Eq. (39). Moreover, future efforts warrant revising the mass-transfer calculations (k_m) to include the influence of porous walls similar to the heat transfer coefficients presented earlier.

For the species equations through the PM and wall layers, a transport-reactive coupling is used by both Peters et al. and Haralampous et al. In the Haralampous et al. version, the formulation for the PM and wall layer is

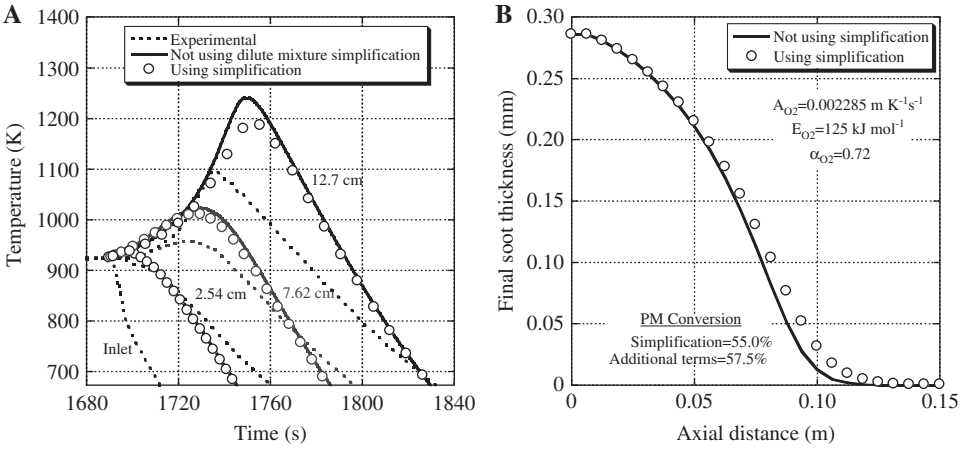

Figure 16 Impact of the dilute mixture simplification (Depcik 2010).

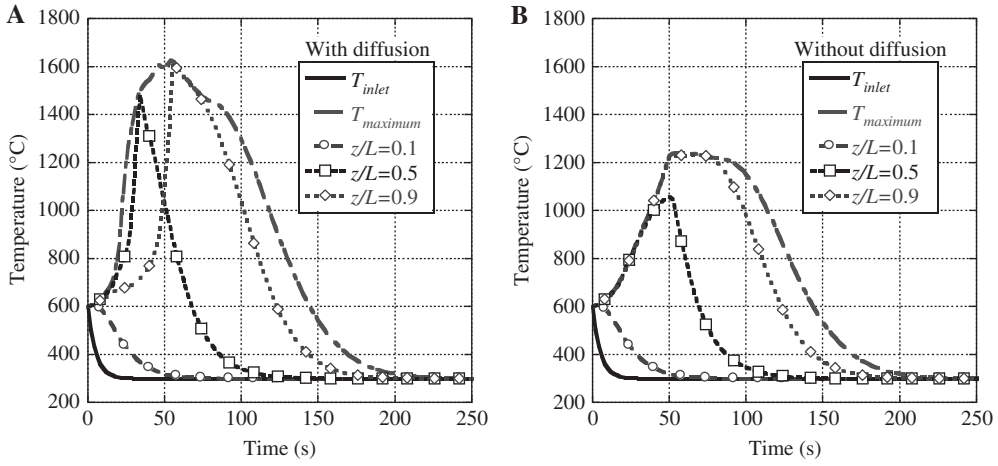

Figure 17 Comparison of temperature predictions during uncontrolled regeneration with and without O_2 diffusion. Computed temperatures along the filter for 12 kg m^{-3} initial PM mass (Haralampous et al. 2004a).

$$u_w \frac{\partial \mathbf{Y}_s}{\partial y} - \mathbf{D}\frac{\partial}{\partial y}\left(f_y \frac{\partial \mathbf{Y}_s}{\partial y}\right) = \dot{\mathbf{S}}_s \tag{75}$$

$$u_w \frac{\partial \mathbf{Y}_w}{\partial y} - \mathbf{D}\frac{\partial}{\partial y}\left(f_y \frac{\partial \mathbf{Y}_w}{\partial y}\right) = \dot{\mathbf{R}}\mathbf{W}. \tag{76}$$

In the above equations, the first term on the left-hand side accounts for the advection of the species through the layer similar to all wall models starting with Bissett and Shadman. The second term on the left-hand side accounts for diffusion through the layer. They find that because the flow velocity is very low through the wall, diffusion of the species could be on the same order of magnitude affecting the regeneration event as illustrated in Figure 17. In fact, the model must account for "back-diffusion" of NO_2 from the wall into the PM layer is prevalent (Figure 18), especially in passively regenerated DPFs. The right-hand side of the equation accounts for PM oxidation and the effects of catalyzed walls or catalytic additive assisted oxidation in the PM and wall layers, respectively.

Depcik later follows similarly through his area-conserved formulation and writes the species equations in these layers as

$$\frac{\partial(\rho_s u_s \mathbf{Y}_s A_s)}{\partial y} + \frac{\partial(\rho_s A_s \mathbf{Y}_s \mathbf{V}_s)}{\partial y} = A_s \dot{\mathbf{S}}_s \tag{77}$$

$$\frac{\partial(\rho_w u_w \mathbf{Y}_w A_w)}{\partial y} + \frac{\partial(\rho_w A_w \mathbf{Y}_w \mathbf{V}_w)}{\partial y} = A_w \dot{\mathbf{R}}\mathbf{W}, \tag{78}$$

incorporating a diffusion flux component within the derivative. In both the Haralampous et al. and the Depcik

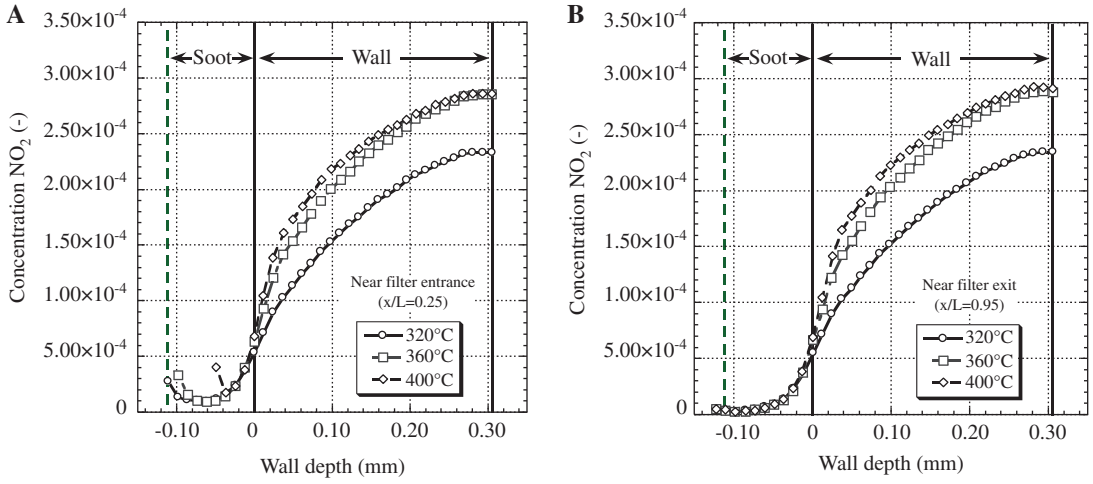

Figure 18 Computed profiles of NO_2 concentration in the PM layer and the filter wall for different time points during balance point testing (Haralampous et al. 2004e).

models, they write the right-hand side terms as a function of the historical model via Eq. (64); this would equal $\dot{S}_{O_2} = -\alpha_1 k_1 S_p \rho_s Y_{s,O_2}$ for Depcik and $\dot{S}_{O_2} = -\alpha_1 k_1 S_p \rho_w Y_{s,O_2}$ for Haralampous et al. The model then uses Eq. (63) to find the values for the partial and complete combustion products:

$$\dot{S}_{CO} = -\frac{2(1-\alpha_1) W_{CO}}{\alpha_1 W_{O_2}} \dot{S}_{O_2} \tag{79}$$

$$\dot{S}_{CO_2} = -\frac{2(\alpha_1 - 0.5) W_{CO_2}}{\alpha_1 W_{O_2}} \dot{S}_{O_2}. \tag{80}$$

The terms for incorporation resulting from NO_2 regeneration are found similarly.

These equations are subject to the following constraint:

$$\sum_{j=1}^{NM} Y_j = 1, \tag{81}$$

with the net species diffusion flux equal to zero for the Depcik model:

$$\sum_{j=1}^{NM} V_j Y_j = 0. \tag{82}$$

One approach that simplifies the computational task is to calculate only the trace species involved in the reactions to reduce the numerical burden of holding equal to the chemical species constraints of Eqs. (81) and (82). For example, Konstandopoulos and Kostoglou (2010) illustrate this approach in their article involving the analytical solutions of the chemical species equations.

The full formulation of the diffusion velocity using mixture-averaged diffusion coefficients is equal to (Coltrin et al. 1990, Reaction Design 2003):

$$\mathbf{V} = -\frac{\mathbf{D}}{\mathbf{X}}\left[\frac{\partial \mathbf{X}}{\partial y} + \frac{(\mathbf{X}-\mathbf{Y})}{p}\frac{\partial p}{\partial y}\right] - \frac{\mathbf{D}^T}{\rho \mathbf{Y} T}\frac{\partial T}{\partial y}. \tag{83}$$

In the above equation, only Depcik discusses the impact of the pressure and temperature derivative terms in the calculation of the diffusion velocity. The energy equation section illustrates that the gas temperature is effectively equal to the filter temperature; hence, the temperature impact on diffusion is nonexistent. However, because the pressure differential between the inlet channel and the outlet channel may be significant, Depcik finds that it has a small impact on the results. Figure 19 illustrates this effect on exit oxygen levels during a regeneration event when using one diffusion constant for all species and individual diffusion constants and incorporating the pressure differential.

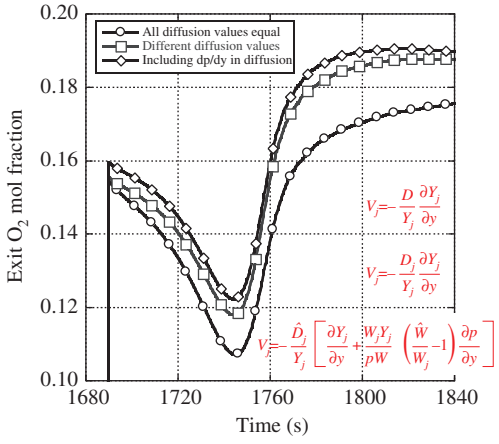

Figure 19 Exit oxygen mole fraction during an oxidation test comparing three different diffusion velocity options (Depcik 2010).

Changing the equation from mole fraction to mass fraction derivatives and assuming that the molecular weight change in the *y*-direction is negligible (assumed by Bissett and Shadman and later validated by Depcik) the diffusion velocity equals

$$\mathbf{V} = -\frac{\mathbf{D}}{\mathbf{Y}}\left[\frac{\partial \mathbf{Y}}{\partial y} + \frac{\mathbf{W}\mathbf{Y}}{p\hat{W}}\left(\frac{\hat{W}}{\mathbf{W}} - 1\right)\frac{\partial p}{\partial y}\right]. \tag{84}$$

Note that if the pressure derivative term was omitted, incorporating this equation into the PM and wall species equations of (77) and (78) would result in the same formulation as Haralampous et al. but on a concentration instead of mass fraction basis. Recently, Konstandopoulos and Kostoglou (2010) presented a work on the coupling of convection diffusion and reaction phenomena using the above equations. They derived analytical solutions for simplified cases leading to approximations applicable to the classic channel model for faster calculation.

The diffusion values used here must take into account the porosity of the wall because of its close proximity. As a result, calculation of an effective diffusivity in the PM and wall layers use the Knudsen and bulk diffusivities along with the tortuosity of the flow (Smith 1970, Reif 1975, Ho and Strieder 1980, Mason and Malinaukus 1983, Cussler 1995):

$$\frac{1}{\mathbf{D}} = \frac{1}{\varepsilon_p}\left(\frac{\tau_{Kn}}{\mathbf{D}_{Kn}} + \frac{\tau_g}{\mathbf{D}_g}\right). \tag{85}$$

In this equation, the binary diffusion constants are

$$\mathbf{D}_g = \frac{1 - Y_j}{\sum_{l \neq j}^{NM} X_j / D_{lj}}, \tag{86}$$

with the Knudsen and bulk tortuosities assumed to depend only on the porosity,

$$\tau_{\mathrm{Kn}}=\frac{9}{8}\text{-}\frac{1}{2}\ln\varepsilon_p+\left(\frac{13}{9}-\frac{9}{8}\right)\varepsilon_p^{2/5} \text{ and } \tau_b=1\text{-}\frac{1}{2}\ln\varepsilon_p, \quad (87)$$

and the Knudsen diffusivity for each species is calculated as

$$\mathbf{D}_{\mathrm{Kn}}=\frac{d_p}{3}\sqrt{\frac{8R_uT_f}{\pi\mathbf{W}}}. \quad (88)$$

The values of porosity (ε_p), tortuosity (τ), and mean pore size (d_p) are based on the microstructure properties of the PM layer and the filter wall.

Experimental determination of tortuosity in the PM layer and the porous wall is not straightforward, especially in porous media with nonuniform pore distribution. Different techniques facing this issue are discussed in a recent work of Kolaczkowski (2003) dealing with measurements of effective diffusivity in catalyst-coated monoliths. In the case of catalytic coatings in flow-through catalysts, typical values for the tortuosity factor range from 1 to 10 (Hayes et al. 2000).

It is worth noting that the species boundary conditions shown above are derived using a methodology consistent to the energy equations. The bulk inlet channel species, $\mathbf{Y}_i$, are used for the suction term in the inlet channel, whereas $\mathbf{Y}_w$ is used for the injection in the outlet channel. The discussion concerning the energy boundary conditions is directly relevant to the species although with additional difficulties. The reaction rates in the wall cannot serve as a mechanism for the instant transition of $\mathbf{Y}_i$ to another expression, similar to the extremely high levels of heat transfer between gas/wall in the solid phase. As a result, $\mathbf{Y}_i$ is considered by the authors appropriate for the suction boundary condition together with a sufficiently detailed modeling of diffusion/reaction phenomena in the porous media.

2.5 Particle mass balance

When particulates flow into a DPF, they first load within the wall layer where the pores are small enough for typical diesel aerosol to be captured by interception and Brownian diffusion (Konstandopoulos and Johnson 1989). After the wall has filled with PM, it then loads on the inlet channel surface in a growing cake layer. In Bissett's original article, he only models the soot cake layer via Eq. (18) as a function of deposit thickness on the surface and oxidation only occurs through thermal oxidation via O_2. To capture the complete PM loading and regeneration profile, it is important to simulate

1. The collection efficiency of the filter;
2. Thermal and catalytic oxidation of the PM through oxygen, NO_2, metal additives, and surface catalysis; and
3. The impact on particulate properties, specifically the permeability for pressure drop calculations.

This section provides a historical summary of these additions to Bissett's original model.

2.5.1 Collection efficiency

Konstandopoulos and Johnson (1989) begin modeling the initial stages of filtration by employing the "unit collector" concept to unloaded DPFs as demonstrated in Figure 20. In their article, they use the following expression for the collector efficiency due to Brownian diffusion:

$$\eta_d=c\cdot g\left(\varepsilon_p^0\right)\cdot \mathrm{Pe}^{-2/3}, \quad (89)$$

where c is a constant equal to 3.5 or 4 depending on the method of diffusion boundary layer analysis (they use 3.5) and $g\left(\varepsilon_p^0\right)$ is a geometric factor that accounts for the proximity effects of unit-cell collectors,

$$g\left(\varepsilon_p^0\right)=\left[\frac{\varepsilon_p^0}{2\text{-}\varepsilon_p^0\text{-}\frac{9}{5}\left(1\text{-}\varepsilon_p^0\right)^{1/3}\text{-}\frac{1}{5}\left(1\text{-}\varepsilon_p^0\right)^2}\right]^{1/3}, \quad (90)$$

and the mass transfer from the particle-laden stream to the surface of the collector depends on the Peclet number:

$$\mathrm{Pe}=\frac{u_w d_c^0}{\varepsilon_p^0 D_d}, \quad (91)$$

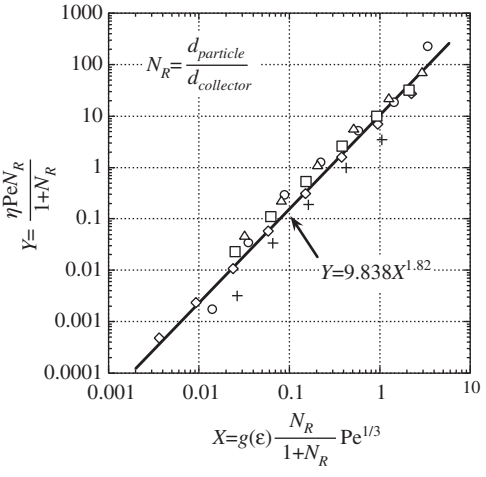

Figure 20 Correlation for the "collection" efficiency of ceramic monoliths (Konstandopoulos and Johnson 1989).

where u_w/ε_p^0 is an interstitial or pore velocity.

Their model computes the Peclet number based on a characteristic dimension of a unit spherical collector:

$$d_c^0=\frac{3}{2}\frac{\left(1-\varepsilon_p^0\right)}{\varepsilon_p^0}d_p, \tag{92}$$

where d_c^0 is the initial value for an unloaded wall. The particle diffusion coefficient in the Peclet number equation,

$$D_d=\frac{k_B T_f}{3\pi\cdot\mu\cdot d_d}SCF, \tag{93}$$

uses Boltzmann's constant (k_B) while depending on slip-flow effects,

$$SCF=1+\mathrm{Kn}(1.257+0.4e^{-1.1/\mathrm{Kn}}), \tag{94}$$

with the local Knudsen number a function of the particulate diameter (d_d),

$$\mathrm{Kn}=\frac{2\ell}{d_d}. \tag{95}$$

From their experiments, the primary particle diameter considered was equal to 0.0178 μm. The exhaust gas mean free path is computed from classic kinetic theory,

$$\ell=\frac{\mu}{p}\sqrt{\frac{\pi R_u T_f}{2\hat{W}}}, \tag{96}$$

with the pressure taken to be the average pressure in the filter wall, often a standard average of p_I and p_{II} at the axial location.

They write the interception efficiency as a function of the same variables:

$$\eta_r=1.5\left(\frac{d_d}{d_c^0}\right)^2\frac{g\left(\varepsilon_p^0\right)^3}{\left[1+\left(d_d/d_c^0\right)\right]^{\frac{3-2\varepsilon_p^0}{3\varepsilon_p^0}}}. \tag{97}$$

By assuming the two mechanisms are independent of each other, they determined the composite collection efficiency of the filter when PM is flowing into an unloaded wall:

$$\eta_f=\eta_d+\eta_r-\eta_d\eta_r. \tag{98}$$

Konstandopoulos et al. (2000) follows up this earlier work by applying the above formulation to a transient filtration model that tracks the accumulation of particulate mass in the filter wall. In this model, the particulate mass deposited in the filter satisfies

$$\frac{\partial m_d}{\partial t}+\frac{\partial \dot{m}_d}{\partial y}=0, \tag{99}$$

where the first term indicates the time rate of change of the particulate deposited per unit collector and the second accounts for the particulate mass flow per unit collector. As mass enters the filter, it distributes according to the local collection efficiency as illustrated in Figure 21:

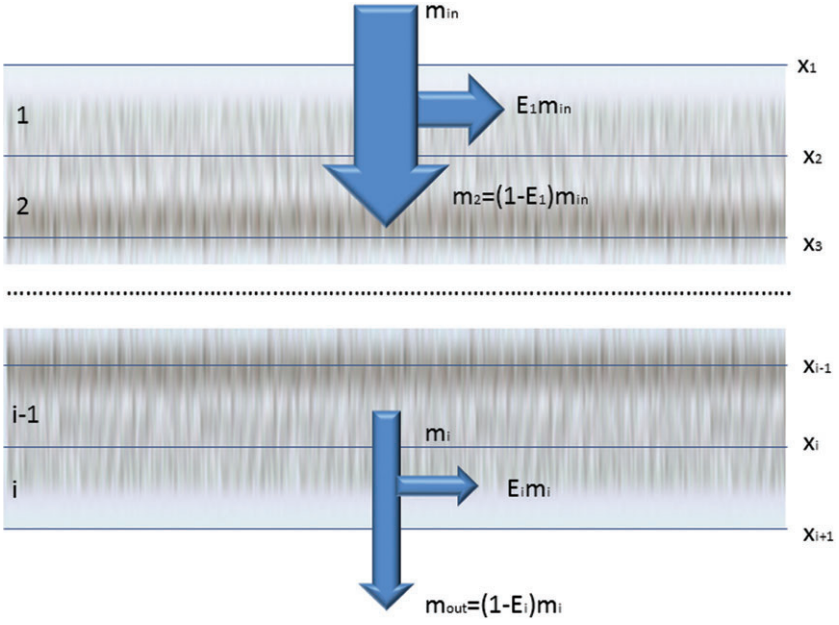

Figure 21 Schematic representation of filter wall discretization into slabs of "unit collectors" (Konstandopoulos et al. 2000).

$$\eta_c = 1 - \exp\left[-\frac{3\eta_{ff}\left(1-\varepsilon_p t\right)}{2\varepsilon_p d_c^0} \right]. \quad (100)$$

The mass deposited at each slab modifies the local unit collector size as follows:

$$d_c = 2\left[\frac{3}{4\pi}\frac{m_d}{\rho_d} + \left(\frac{d_c^0}{2}\right)^3 \right]^{1/3}, \quad (101)$$

where m_d is the mass of deposit and ρ_d is the particulate packing density in the cake deposit and filter wall, respectively, at time t. This influences the local porosity as follows:

$$\varepsilon_p = 1 - \left(\frac{d_c}{d_c^0}\right)^3 \left(1-\varepsilon_p^0\right). \quad (102)$$

The geometric factor of Eq. (90) and Peclet number of Eq. (91) then use the updated porosity and unit collector size in computing the Brownian collection efficiency of Eq. (89) and interception efficiency of Eq. (97).

They compute the second term in Eq. (99) using Eq. (100) by replacing the wall thickness with a differential distance (i.e., replace t_f with Δy) and the evolution of deposited mass via Eqs. (101) and (102):

$$\frac{\partial \dot{m}_d}{\partial y} = -\eta_c \dot{m}_d. \quad (103)$$

At this point, the model is able to explain the collection of PM within the filter wall often called deep-bed filtration. The extension to the cake layer comes by defining a partition coefficient to determine the fraction of mass collected in the first "slab" that contributes to cake formation. Based on geometrical grounds, this value depends on a dimensionless blocked-area fraction expressed as

$$\Phi = \frac{\left(d_c|_{y=0}\right)^2 - \left(d_c^0\right)^2}{\left(\omega b\right)^2 - \left(d_c^0\right)^2}, \quad (104)$$

where $d_c|_{y=0}$ represents the characteristic dimension of a unit spherical collector in the first differential area of the wall, d_b is a "unit cell" diameter:

$$d_b^3 = \left(1-\varepsilon_p\right) d_c^3, \quad (105)$$

and ω is a dimensionless "percolation" factor ($0<\omega<1$) that determines how close the diameter of a loaded collector can approach that of a unit cell before filtration occurs only through the PM cake layer. This parameter allows calibration of the model to an experimental time-history loading profile. Later work by Mohammed et al. (2006) indicate that a deficiency of this model is using the partition coefficient, which is a function of filter wall parameters, as a filtration parameter for the PM cake layer when the cake layer becomes a filter for the particles.

Konstandopoulos et al. (2002) revisit this model and investigate the impact of velocity for the porosity via Eq. (102). In particular, they find that, for high Peclet numbers, the deposit porosity is independent of this number and an asymptotic constant is the result. At low Peclet numbers in the diffusion-dominated regime, a power law describes the porosity when Pe>0.3:

$$\varepsilon_p = A\mathrm{Pe}^{-B} + C, \quad (106)$$

where A, B, and C are constants that depend on particle morphology and deposition surface.

A few years later, Konstandopoulos et al. (2005) revisit this model to generalize the results down to the diffusion limited deposition limit:

$$\varepsilon_p = 1 - \left(1-\varepsilon_p^{\infty}\right)\left(1+\frac{\mathrm{Pe}^{\infty}}{\mathrm{Pe}}\right)^{-n}, \quad (107)$$

with ε_p^{∞} as the Peclet number asymptote of the porosity and Pe^{∞} as the characteristic crossover Pe number defining the scale beyond which the convective mechanism will take over the diffusive mechanism of deposition. This allows a correlation between PM porosity and the flow through the wall as illustrated in Figure 22.

Fukushima et al. (2007) revisit the filtration efficiency of Eq. (100) to write it as a function of an effective length scale for deposition:

$$d_{eff} = \left(\frac{1}{d_p} + \frac{1}{d_c} + \frac{1}{d_{cdl}}\right)^{-1}, \quad (108)$$

where d_{cdl} is a characteristic decay length measured quantitatively from different filter material images:

$$\eta_c = 1.2343 - 0.5106\left[\frac{\left(d_{eff}-1.081\right)^{2/3}}{g\left(\varepsilon_p\right)}\right]. \quad (109)$$

This functional dependence includes a lower cutoff effective length approximately the image resolution scale (1.081 μm).

To summarize, this model is able to simulate the PM evolution within the wall layer by applying continuity Eq. (99) and including local collection efficiency through Eqs. (98), (100) and (103) to determine the amount that stores

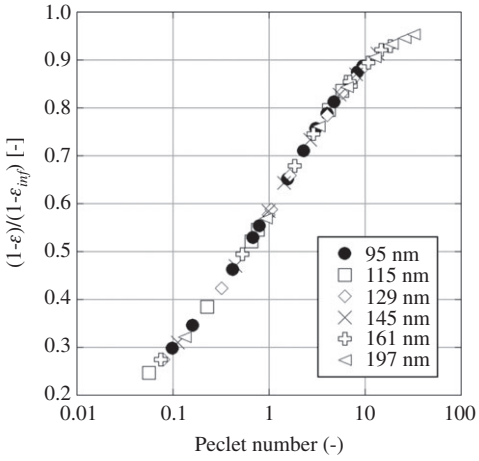

Figure 22 Dependence of the PM cake porosity for different PM aggregate sizes at the prevailing Peclet number (Konstandopoulos et al. 2005).

in each differential volume as illustrated in Figure 21. As the wall evolves, recalculation of the porosity and unit collector size occurs via a function of loading within the layer and the local wall velocity represented through the Peclet number. The extension of the model to a cake layer happens by calibrating a percolation factor in Eq. (104) to an experimental loading test and applying it to the boundary cell in the wall that borders the cake layer. A calculation of its particulate evolution then occurs via the same wall mechanism again using continuity Eq. (99).

2.5.2 Particulate combustion

At the same time as Konstandopoulos et al. were investigating filtration efficiency, Koltsakis and Stamatelos (1996a,b) expand the classic PM thickness model of Bissett by including the partial oxidation factor of Eq. (63) by replacing Eq. (28) with Eq. (64) when formulating the transient thickness evolution:

$$\rho_d \frac{\partial t_d}{\partial t} = -\left[W_{C_{(s)}} / \left(\alpha_1 W_{O_2}\right)\right] \rho_w u_w Y_{I,O_2} \left[1-\exp\left(-\alpha_1 k_{O_2} S_p t_d / u_w\right)\right], \quad (110)$$

where k_{O_2} is the specific rate constant for the O_2 soot oxidation reaction coming originally from Eq. (28).

At this point, researchers start investigating alternative methods of regeneration to reduce the high temperatures needed to combust diesel particulate relative to light-duty diesel engine exhaust. The idea is to prevent significant pressure drops that can occur at high loadings possibly leading to the thermal runaway of the device. As a result, the first articles begin to appear in the early 1990s regarding the use of fuel additives for lowering the regeneration temperature of diesel particulate through catalysis (Harvey et al. 1994, Tan et al. 1996). Koltsakis and Stamatelos (1996a,b) take these concepts and further expand their model to account for catalytic reduction of PM due to metal oxide fuel additive combustion (clarified the following year by Koltsakis and Stamatelos 1997a,b):

$$\rho_d \frac{\partial t_d}{\partial t} = -\left[W_{C_{(s)}} / \left(\alpha_1 W_{O_2}\right)\right] \rho_w u_w Y_{I,O_2} \left[1-\exp\left(-\alpha_1 k_{O_2} S_p t_d / u_w\right)\right] - \frac{\rho_d t_d \xi R_{red}}{2\alpha_{cat}}, \quad (111)$$

where ξ are the moles of metal oxides present in the PM compared with the carbon moles present in the PM, R_{red} is an Arrhenius-type expression that is a function of oxidation state of the metal component, and α_{cat} is an index of completeness similar to carbon oxidation:

$$C_{(s)} + 4\alpha_{cat} MeO \rightarrow 2\alpha_{cat} Me_2O + 2(\alpha_{cat} - 0.5) CO_2 + 2(1-\alpha_{cat}) CO. \quad (112)$$

Around the same time, Awara et al. (1997) summarize previous efforts in regards to activation energies and reaction rates for diesel PM reactions with and without fuel additives. In addition, Gantawar et al. (1997) perform a study of regeneration characteristics for SiC and cordierite using fuel additives.

Konstandopoulos and Kostoglou (1999) follow in 1999 with one of the first modeling efforts regarding a catalytically coated DPF and model deposit evolution using a local collection efficiency,

$$\frac{\partial(\rho_d t_d)}{\partial t} = \eta_f \rho_w u_w Y_d, \quad (113)$$

where Y_d is the local PM mass fraction, and the authors infer that the collection efficiency refers to the previous section involving Eq. (98). In addition, this article involves PM thermal oxidation including an index of completeness similar to Koltsakis and Stamatelos and oxidation via a catalytically coated surface and through fuel additives in the different layers indicated in Figure 15 (also seen in Kostoglou et al. 2003). The authors leave the functional form of the adaption to Eq. (64) and its refinement into the equation for the time rate change of PM thickness to the reader because of the different nomenclature involved in the Konstandopoulos and Kostoglou article. Of interest, they do not show both the deposit evolution term and the PM oxidation components in the same equation for $\partial(\rho_d t_d)/\partial t$; however, the reader can infer an additive dependence on the right-hand side of the equation.

In the following year, Konstandopoulos et al. (2000) expand this work to incorporate NO_2 passively regenerated DPFs by modifying their particulate evolution equation using Eq. (65) and rewrite the evolution equation as a function of mass instead (dm_d/dt) of thickness in each layer. In their article, they state the relationship between mass of PM and its thickness as

$$t_d = \frac{1}{2}\left(d - \sqrt{d^2 - \frac{m_{d,t}}{N_{ic} L \rho_d}}\right), \tag{114}$$

where $m_{d,t}$ is the total PM mass in the DPF, N_{ic} is the total number of inlet channels, and L is the effective channel length.

Kandylas and Koltsakis (2002) follow this work a couple years later by expanding Eq. (110) to include NO_2 regeneration through Eqs. (66) and (67):

$$\rho_d \frac{\partial t_d}{\partial t} = -\sum_{k=O_2,NO_2} \left\{\left[W_{C_{(s)}}/(\alpha_k W_k)\right]\rho_w u_w Y_{I,k} \left[1-\exp\left(-\alpha_k k_k S_p t_d/u_w\right)\right]\right\}. \tag{115}$$

Again, the difference between the Konstandopoulos et al. and the Koltsakis et al. models is a matter of nomenclature and presentation of the equations, but the physics are similar and both follow Bissett and Shadman's initial effort.

In the following 2 years, Peters et al. (Peters 2003, Peters et al. 2004) simulate the PM mass per unit length on the surface by including a flow of PM to the surface:

$$\frac{\partial m_d}{\partial t} + c_m \frac{\partial (u_I m_d)}{\partial z} = 4 u_w d_I \rho_{dc}, \tag{116}$$

where c_m is a migration constant that accounts for drag forces that result when PM translates along the channel (Figure 23) and ρ_{dc} is the PM density in the channel. PM oxidation is included in their model by writing an equation for PM mass fraction and using an Arrhenius expression to account for the oxidation components. However, their articles do not illustrate a merging of this mass fraction equation and Eq. (116).

Haralampous et al. (2003) convert the thickness-based expression of Eq. (115) into a mass-based expression written as a function of PM mass per unit volume:

$$\frac{\partial m_d}{\partial t} = -s_F \sum_{k=O_2,NO_2} \left\{\left[W_{C_{(s)}}/(\alpha_k W_k)\right]\rho_w u_w Y_{I,k} \left[1-\exp\left(-\alpha_k k_k S_p t_d/u_w\right)\right]\right\}, \tag{117}$$

where s_F is the specific area of the filter that depends on the number of cells per square inch converted into the proper units:

$$S_F = 2d \cdot 1550 \cdot cpsi. \tag{118}$$

It is important to note that if the bulk density of the PM is constant, the formulations via soot thickness and mass of soot cake are the same. As the next section illustrates, by writing in a mass-based manner, the model can take into account how the properties inside the soot cake can vary. Hence, future efforts can include modeling soot property changes during oxidation.

They modify this formulation on the following year (Haralampous and Koltsakis 2004a,b, Haralampous et al. 2004a,d,e) by simplifying the right-hand side:

$$\frac{1}{m_d}\frac{dm_d}{dt} = -\sum_{k=O_2,NO_2} S_p k_k p_k \tag{119}$$

as a linear dependence on the partial pressure of the oxidation species.

Recent work by Depcik and Assanis (Depcik and Assanis 2008, Depcik 2010) use these earlier efforts to simulate the propagation of PM along the filter with regeneration occurring only via traditional thermal oxidation from O_2 in a cake layer. An equation for PM mass per unit length on the surface simulates the amount of PM in each numerical cell in one channel,

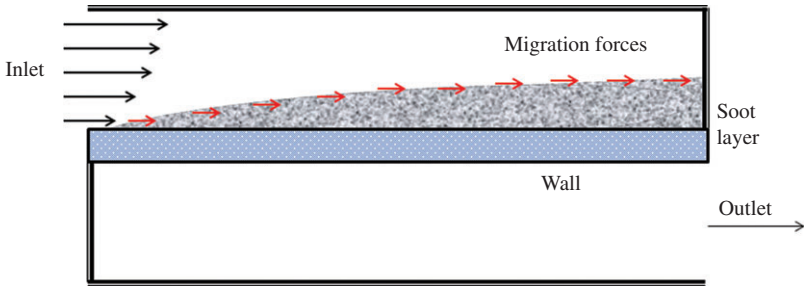

Figure 23 Forces on PM particles in the Peters et al. models (Peters 2003; Peters et al. 2004).

$$\frac{dm_d}{dt}=\varsigma-\chi m_d, \tag{120}$$

which gives the total PM mass in the filter by multiplying this value by the total number of inlet channels. In this equation, the PM mass flow rate per mesh interval, s, is determined as a function of changing surface area similar to Peters et al.:

$$s=4\rho_s u_s d_I Y_d \tag{121}$$

using the assumption that a constant mass fraction of PM occurs in the inlet channel:

$$\frac{dY_d}{dz}=0. \tag{122}$$

The mass fraction of PM into the filter comes from the mass flow rate of PM into the DPF as compared with the total flow rate of gas:

$$Y_d=\frac{\dot{m}_{PM}}{\dot{m}_{in}}. \tag{123}$$

They calculate a PM combustion time scale from the historical efforts via Eq. (64):

$$\chi=-\frac{W_{C_{(s)}}}{W_{O_2}}\frac{k_1 S_p \rho_s Y_{s,O_2}}{\rho_d} \tag{124}$$

using the localized gas density and mass fraction of oxygen in the cake layer. The relationship between PM mass per unit length and its thickness are a function now of the local PM mass:

$$t_d=\frac{1}{2}\left(d-\sqrt{d^2-\frac{m_d}{\rho_d}}\right). \tag{125}$$

The result of these efforts is an investigation into the PM loading profile during constant and random loading events (as shown in Figure 24), which illustrate that changing the flow rate does not significantly impact the loading profile along the filter and subsequent regeneration.

This historical summary illustrates a number of different models in the literature that simulate similar physical concepts. One version of the model simulates a 1D particulate loading equation in the axial direction with the wall phenomenon lumped into source terms on the right-hand side:

$$\frac{\partial m_d}{\partial t}+\frac{\partial\left(u_d m_d\right)}{\partial z}=\dot{m}_d^s+\dot{m}_d^r, \tag{126}$$

where the time rate of change of particulate mass at each axial location (point in z) is impacted by the flow of particulate down the channel (possibly a function of channel velocity and/or migration), the amount stored on the surface that may include a storage efficiency component $\left(\dot{m}_d^s\right)$, and the thermal and catalytic oxidation reactions occurring on the surface $\left(\dot{m}_d^r\right)$. Of interest, researchers only model the PM flow to the surface a function of wall-flow rates (u_w); however, as indicated in the species equation section, diffusion between the gas and the surface might also be important and need to be included.

Alternatively, researchers simulate the time rate of change at each axial location in the cake and wall layers also in 1D (normal direction):

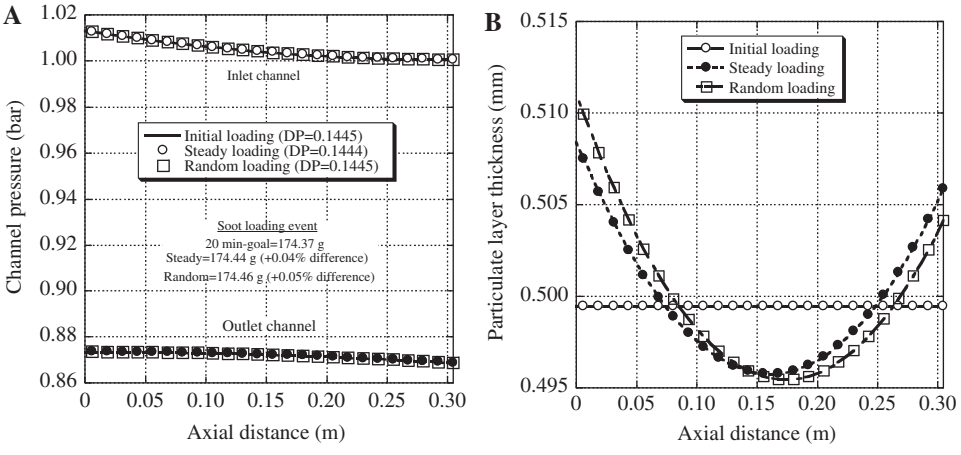

Figure 24 Comparison of three different PM loading events with respect to (A) pressure and (B) particulate layer thickness (Depcik and Assanis 2008).

$$\frac{\partial m_d}{\partial t}+\frac{\partial\left(u_d m_d\right)}{\partial y}=\dot{m}_d^s+\dot{m}_d^r, \tag{127}$$

which include the same components but now as a function of local thermodynamic components in the *y*-direction. This history shows that alternative versions of these equations exist as a function of PM density or thickness. These then allow for the simulation of the change in the specific surface area of the deposit. One potential future option is to merge the models into a 1+1D type of model, similar to the species equations, where Eq. (126) propagates the PM to the boundary of the wall or cake layer at each axial location and then Eq. (127) simulates its flow within these layers and the oxidation (thermal/catalytic) events that the PM undergoes. Of importance, the merging of the chemical species equations into the 1+1D model as previously discussed is a good place to start if attempting to undertake this integration.

2.5.3 PM properties

The density and permeability of the wall and PM layers are probably the most important governing parameters affecting the pressure drop in the DPF. Because most commercial DPF systems base their control on a pressure drop measurement, a deeper knowledge of this information becomes increasingly important. Moreover, the PM layer properties are fundamental to the simulation of the loading and regeneration process in the DPF as the previous section illustrates.

In the early stages of DPF technology and modeling development, most models use a simple approach to describe the PM layer, mostly assuming a constant value for density and permeability (Bissett 1984, Koltsakis and Stamatelos 1996a,b, 1997a,b). Konstandopoulos and Johnson (1989) were the first to simulate the permeability as a function of porous media theory for an unloaded DPF. Through their unit spherical collector model, they formulate that the permeability as

$$\mathrm{K}_f=f\left(\varepsilon_p\right)d_c^2, \tag{128}$$

using the Kuwabara model for beds of spherical particles:

$$f\left(\varepsilon_p\right)=\frac{2}{9}\frac{\left[2-\frac{9}{5}\left(1-\varepsilon_p\right)^{1/3}-\varepsilon_p-\frac{1}{5}\left(1-\varepsilon_p\right)^2\right]}{\left(1-\varepsilon_p\right)}. \tag{129}$$

In the next decade, Sorenson et al. (1994) experimentally measure the PM layer density, whereas Pattas et al. (1997) employ pressure drop measurements on a vehicle combined with modeling to derive the product ($\rho_d \mathrm{K}_d$) and find that this product increases with temperature. Versaevel et al. (2000) later validate this temperature dependency based on small-scale filter testing and propose the slip-flow effect, mentioned in Section 2.5.1, as an explanation. They create a formula that correlates this product with the mean free path length and a constant calibrated with experiments:

$$\rho_d \mathrm{K}_d=c\frac{\ell}{\ell_{ref}}, \tag{130}$$

where *c* equals 0.55 Da kg m^{-3} and ℓ_{ref} is the reference gas mean free path at 1 bar and 300 K.

The use of pressure drop modeling as a tool for the assessment of PM permeability was also presented (Konstandopoulos et al. 2000, Masoudi et al. 2001). The article by Konstandopoulos et al. uses the parabolic growth of pressure drop at extremely high PM loadings to estimate indirectly the PM layer density. At the same time, they enhance their original permeability calculation Eq. (128) by also including slip-flow effects:

$$\mathrm{K}_f=SCF\cdot f\left(\varepsilon_p\right)d_c^2, \tag{131}$$

where the permeability of the wall changes as a function of PM loading via the changing unit collector size and porosity in Section 2.5.1.

Konstandopoulos et al. (2002) revisit this formulation and replace the unit collector size in the above calculation with the primary size of the particles that deposit and compose the PM layer:

$$\mathrm{K}_d=SCF\cdot f\left(\varepsilon_p\right)d_d^2, \tag{132}$$

with a size in the range of 25–40 nm. They calculate the slip flow coefficient in Eq. (94) now as a function of this variable and compute the particulate density based on the density of the solid PM (ρ_{solid}) and the porosity:

$$\rho_d=\rho_{solid}(1-\varepsilon_p). \tag{133}$$

In the following year, Konstandopoulos (2003) extends the model to the Forchheimer coefficient by basing it as a function of the permeability of the medium:

$$\beta_f=\frac{c}{\varepsilon_p^{1.5}\sqrt{\mathrm{K}_f}}, \tag{134}$$

where *c* is a constant between 0.134 and 0.298 depending on the wall.

Most experimental studies up to this point are focusing on an indirect assessment of the product ($\rho_d K_d$) with the aid of pressure drop models. With the aid of targeted engine experiments, it is possible to calibrate reliably the product of PM density and permeability when the performing loading events under steady-state conditions (Haralampous et al. 2004b,c). Regarding the density of the soot cake layer, literature data on its value appear in the pioneering work of Howitt and Montierth (1981). They report values between 50 and 60 kg m^{-3} by weight and layer thickness measurements in cordierite filters with pressure drops below 150 mbar. Many years later, Sorenson et al. (1994) measure similarly the soot layer density in cordierite filters operating to a maximum pressure drop of 450 mbar and obtain a value of 120 kg m^{-3}. A similar measurement on a SiC filter operating to a maximum pressure drop of 250 mbar gives a value of 90 kg m^{-3}. The Ph.D. efforts of Stratakis (2004) measure PM layer density at 93.6 kg m^{-3} using a scanning electron microscope. In the above literature references, it is not clear whether the authors account for the soot mass in the wall when calculating the layer density. In 2005 a single-channel methodology is adopted for PM collection and examination using X-ray scattering techniques (Gallant 2005). The results show that the local density is approximately three times higher close to the wall compared with the values measured close to the surface.

Indirect methods to obtain the layer density at different loading conditions based on pressure drop modeling and theoretical porosity-permeability correlations indicate values between 40 and 135 kg m^{-3} depending on the Peclet number for pressure drops below 250 mbar (Konstandopoulos et al. 2002). Recent efforts calculate the indirectly assessed solidosity of the soot layer as between 0.06 and 0.075 in uncompressed state and from 0.07 to 0.085 after compression above 200 mbar (Konstandopoulos et al. 2008). Assuming a commonly used solid-state density of 2000 kg m^{-3}, the above values translate to between 120 and 170 kg m^{-3}.

In another research study, Koltsakis et al. use realistic exhaust conditions and direct optical methods to measure the soot layer density independently from the permeability (Koltsakis et al. 2006). The experimental results reveal a clear dependency of soot cake density on filtration velocity as well as on the soot loading itself as shown in Figures 25 and 26, respectively. In this experiment, measured values of the soot layer density vary between 25 and 100 kg m^{-3}. Partial explanation of these findings occurs through soot compaction effects occurring at high backpressures, and the authors suggest additional mechanisms related to the depth of filtration within the

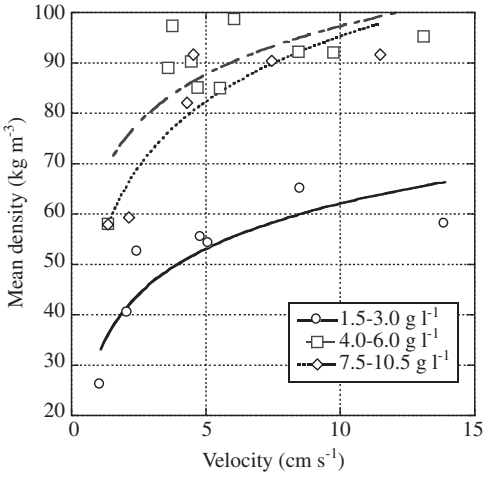

Figure 25 Soot layer density versus flow velocity for different soot loadings (Koltsakis et al. 2006).

soot cake layer. From this experimental data, they develop expressions for soot cake density and permeability variation as a function of compressive stress. In their model, the cake solidosity, ε_s, and permeability are functions of the compressive stress, p_c, only as shown below:

$$\varepsilon_s = \varepsilon_s^0 \left(1 + \frac{p_c}{p_a}\right)^{c_1} \tag{135}$$

$$K_d = K_d^0 \left(1 + \frac{p_m}{p_a}\right)^{-c_2}, \tag{136}$$

where ε_s^0 and K_d^0 refer to the uncompressed state of these variables, p_a is a compressibility pressure that is indicative of soot cake layer strength, and c_1 and c_2 are constant

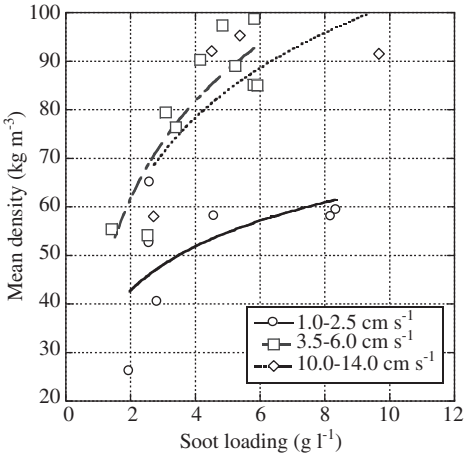

Figure 26 Soot layer density versus soot loading (Koltsakis et al. 2006).

exponents. The relationship between the gas pressure in the layer and the compressive stress is

$$p_l = p_m + p_c. \tag{137}$$

This model enables the prediction of intralayer density fields inside the cake during compression events caused by highly transient flow conditions, as shown in Figure 27. It is important to mention that there can be one porosity for the wall (ε_p) and one for the soot cake layer (ε_s) or an effective porosity that takes into account both layers. The discussion of both of these variables in this document should help elucidate what approach the researcher mentioned is taking.

Figure 28 presents the predicted soot layer density in steady-state conditions as a function of filtration speed and soot loading based on the above model. The same plot includes measured densities grouped in terms of soot loading. The model captures the main trends; however, the authors conclude that this indirect mechanism alone is not sufficient to explain all experimental observations. They suggest that a more sophisticated modeling approach would have to include a filtration model within the soot layer, which would calculate the penetration of incoming particles in the existing layer as a function of the prevailing filtration parameters. Note that although the model does not fit perfectly with the measured values (e.g., medium and high loadings are similar in magnitude), the additional results presented in the corresponding reference proved that the compression effects can be predicted reasonably well.

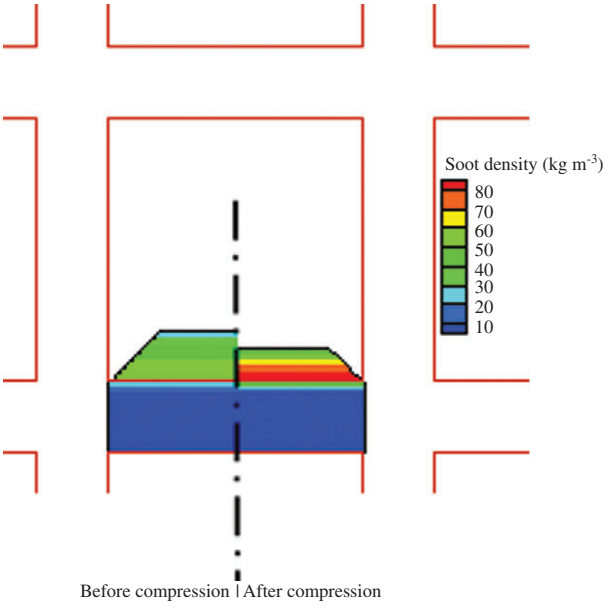

Figure 27 Intralayer density field before and after compression (Koltsakis et al. 2006).

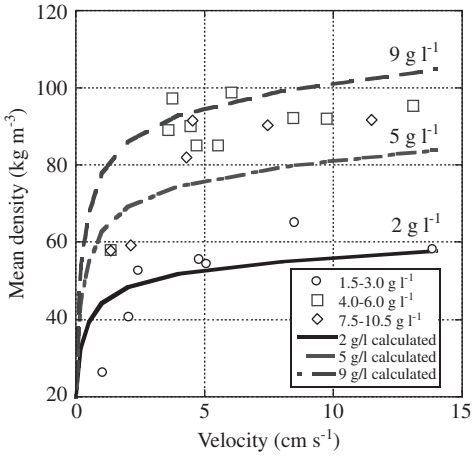

Figure 28 Model predicted layer density versus experimental data (Koltsakis et al. 2006).

To predict the soot layer density, Konstandopoulos and Kostoglou (2004) present a model to simulate the time change in PM layer density and the specific surface area as a function of microstructural aspects (summarized the next year by Konstandopoulos et al. 2005). The density evolution is a function of the rate of movement of the deposit through the cake and wall layers along with its oxidation:

$$\frac{\partial \rho_d}{\partial t} + \dot{y}\frac{\partial \rho_d}{\partial y} = \varphi R_{ox}. \tag{138}$$

In this equation, $\dot{y}$ is the velocity of the deposit through the layers:

$$\dot{y} = \int_0^y (1-\varphi)\frac{R_{ox}}{\rho_d} dy, \tag{139}$$

which is a function of the PM oxidation along with a parameter, φ, that has a value between 0 and 1 to represent a general continuum description of the deposit microstructure. The local PM oxidation rate, R_{ox}, is a function of thermal and catalytic reactions of the PM:

$$R_{ox} = -\left[(1-\kappa)k_{thermal} + \kappa k_{catalytic}\right] S_p \rho_w \rho_d Y_{w,O_2} \left(W_{C_{(s)}}/W_{O_2}\right), \tag{140}$$

where κ is another variable, between 0 and 1, which also represents the continuum description of the deposit microstructure.

They write the change in specific surface area as

$$\frac{\partial S_p}{\partial t} + \dot{y}\frac{\partial S_p}{\partial y} = S_p^0 \kappa \left(\rho_d^0\right)^{\kappa} \left(\rho_d\right)^{1-\kappa} \frac{\partial \rho_d}{\partial t}, \tag{141}$$

where the superscript^0 indicates the initial value of that parameter. Of importance, the problem of determining

the permeability of the soot-loaded filter wall is more complicated than compared with the soot cake permeability. The penetrating soot by depth filtration inside the wall micropores has a dramatic effect on wall permeability that is responsible for the steep pressure drop increase at the early stage of DPF loading before the soot cake layer starts to form. The literature illustrates other formulations for the permeability of a loaded filter wall using the concepts in the previous two sections (Mohammed et al. 2006):

$$\frac{K_d}{K_f}=\left(\frac{d_c|_{y=0}}{d_c^0}\right)^2\left[\frac{f(\varepsilon_p)}{f(\varepsilon_p^0)}\right]\left(\frac{1-\varepsilon_p^0}{1-\varepsilon_p}\right). \quad (142)$$

Obviously, the loaded wall permeability is a function of the amount of soot trapped in the wall, which depends on the filtration mechanisms, that is, the wall microstructure, the size of the particles, and the flow conditions. Typical reported values of accumulated soot mass in conventional wall-flow filters may range between 0.3 and 1.0 g l^{-1} (Koltsakis et al. 2009a). The lower values correspond to normal porosity filters operating at low filtration velocities and the higher values correspond to higher porosity filters operating at high flow velocities. Higher amounts of soot in the wall are shown to be a function of low initial filtration efficiency and low permeability of the loaded wall. Therefore, there is an increasing interest in developing technologies to minimize the depth filtration effect (Li et al. 2008, Ogyu et al. 2008, Johnson 2009, Lee and Yang 2010). Such technologies offer the additional advantage of an increasingly linear correlation between accumulated soot mass and pressure drop making onboard management of the DPF operation control much simpler.

2.6 Filter energy equations

To calculate the temperature of the filter, Bissett and Shadman used the energy equation to describe its time history in the wall direction. Because the results indicated only a small variation, this allowed Bissett in his 1984 article to neglect this component and only present its evolution in the axial direction for the channel model. As a result, most researchers follow this tactic; however, understanding its formulation in the wall direction is important in discussing the assumptions involved with DPF modeling. As a result, this section describes the history of both formulations along with an explanation of the modifications that they underwent.

2.6.1 Axial filter energy equation

In the axial direction model, Bissett assumes that the filter wall and PM layer have the same temperature due to their proximity to each other and the fact that PM is present within the filter wall due to deep-bed filtration. His model includes the effects of axial conduction in the wall, heat transfer from the gases in the channel, and the effects of PM oxidation on the energy of the wall. He does include an enthalpy flow through the wall in the initial steps of his formulation, but the terms involved cancel each other out and do not appear in the final resultant equation.

Traditionally, researchers write this equation as a function of wall and PM thicknesses or using relative surface area terms; however, Depcik and Assanis wrote it as a function of volumetric terms intended to account for the entire filter volume based on a 1D representation. This is similar to the methodology for modeling the monolith energy equation in catalyst modeling (Depcik and Assanis 2005). Because the literature, most notably Konstandopoulos et al. and Koltsakis et al., write this equation slightly differently, the authors use the volumetric interpretation here to describe the equation for commonality between all formulations.

The current version of the axial filter energy equation is

$$\left(\rho_f c_f V_f+\rho_d c_d V_d\right)\frac{\partial T_f}{\partial t}=\dot{Q}_{cond}+\dot{Q}_{multi}+\dot{Q}_{conv}+\dot{Q}_{wall}+\dot{Q}_{supply}+\dot{Q}_{rad}+\dot{Q}_{reac}+\dot{Q}_{cat}+\dot{Q}_{inner}, \quad (143)$$

where researchers may not include all of the terms on the right-hand side and the volume terms indicated are per unit length. In the Konstandopoulos et al. versions, they replace the volume terms with the thickness of the PM and wall layers, whereas Koltsakis et al. omit these terms and use an effective heat capacity and density along with including a filter-specific filtration area term on the right-hand side to account for the surface area to volume factor.

The heat transfer due to conduction incorporates variable PM loading in the axial direction:

$$\dot{Q}_{cond}=\lambda_f V_f\frac{\partial^2 T_f}{\partial z^2}+\lambda_d\frac{\partial}{\partial z}\left(V_d\frac{\partial T_f}{\partial z}\right). \quad (144)$$

Taking into account external heat losses and flow maldistributions requires extending the model into a second dimension and possibly a third dimension. Because the focus of this article is modeling involving the classic Bissett versions, the authors do not include a description of other multidimensional models in the literature that do not follow the Bissett energy equation approach (Aoki

et al. 1993, Jørgensen and Sorenson 1997, Romero et al. 1997, Opris and Johnson 1998a,b, Miyairi et al. 2001). The first instance of 2D adaption of the classic Bissett model is by Konstandopoulos et al. (2001), who simplify a multidimensional DPF model by using a continuum description of the filter (Gropi and Tronconi 1996). This formulation involves implementing an effective thermal conductivity tensor (Haralampous et al. 2003, Konstandopoulos et al. 2003a, Kostoglou et al. 2003):

$$\dot{Q}_{multi}=\frac{1}{r}\frac{\partial}{\partial r}\left[r\lambda_{eff}\left(V_f+V_d\right)\frac{\partial T_f}{\partial r}\right], \tag{145}$$

where λ_{eff} is an effective radial conductivity that depends on the honeycomb bulk thermal conductivity as well as its geometrical details (wall thickness, diameter, and unit porosity). They modify this expression to account for the contribution of the PM layer:

$$\lambda_{eff}=\frac{1-\sqrt{\varepsilon_p}}{1+\varepsilon_p-\sqrt{\varepsilon_p}}\left[\frac{\left(d+t_f\right)^2-d^2}{\left(1-\varepsilon_p\right)\left(d+t_f\right)^2}\lambda_f+\frac{d^2-\left(d+2t_d\right)^2}{2\left(1-\varepsilon_p\right)\left(d+t_f\right)^2}\lambda_d\right], \tag{146}$$

where the instantaneous value of the macroscopic honeycomb structure porosity is

$$\varepsilon_p=\frac{d^2+d_I^2}{2\left(d+t_f\right)^2}. \tag{147}$$

The multidimensional version of the filter energy equation effectively eliminates Bissett's original assumptions of an adiabatic device with spatially uniform inlet conditions using ambient heat transfer boundary conditions and zones of different inlet flow conditions. The Koltsakis et al. version involving a filter-specific filtration area term is similar and seen in Haralampous and Koltsakis (2004a,b) and Haralampous et al. (2003, 2004a).

The heat transfer from the gases in the channel remains relatively constant until Depcik and Assanis modify it to include the impact of varying surface area:

$$\dot{Q}_{conv}=\left(\frac{N_c}{2}\right)\left[4h_g d_I\left(T_I-T_f\right)+4h_g d_{II}\left(T_{II}-T_f\right)\right], \tag{148}$$

where the heat transfer coefficient is a function of local injection or suction due to the wall-flow velocity.

The discussion involving the energy flux through the wall starts when Pattas and Samaras (1989) formulate a discretized version of the energy equation and find this term not included in the original Bissett model. This relates back to the discrepancy in the literature regarding the channel energy equations (see previous discussion and Koltsakis and Stamatelos 1997a,b, Konstandopoulos et al. 2001, 2005, Kostoglou et al. 2003). Based on the original channel energy equations, the enthalpy flow through the wall cancelled itself out and, as a result, did not appear in this equation. A few years later, this equation was written in differential format including this term (Koltsakis and Stamatelos 1997a,b). Depcik and Assanis later modify this expression to account for the local density and velocity along with the impact of varying surface area:

$$\dot{Q}_{wall}=\left(\frac{N_c}{2}\right)\left(4\rho_s u_s h_I d_I-4\rho_w u_w h_w d_{II}\right). \tag{149}$$

The energy flow through the wall is often written as a function of constant pressure-specific heat times a temperature difference; that is, $h_I-h_w=c_p(T_I-T_w)$. Because the chemical species modeled has different heats of formation and sensible components, a more rigorous interpretation requires the use of enthalpies. Depcik found that making the constant pressure assumption underpredicts the PM conversion during an oxygen regeneration case by approximately 3%. In the case of models that do not calculate the flow profiles through the wall, the wall average density and velocity will replace the respective terms in the above equation.

Because active heating is a possible method of regenerating the filter, Romero et al. (1995) illustrate how to include this ability in the model formulation:

$$\dot{Q}_{supply}=\dot{q}\left(V_f+V_d\right), \tag{150}$$

where $\dot{q}$ is a volumetric energy source in each zone.

Bissett originally neglected radiative heat transport, but Konstandopoulos et al. (2001) incorporate it in their original multidimensional formulation for completeness. However, in this article, they mention that this term is insignificant for typical regeneration applications and it does not appear in their later continuum-based modeling articles (Konstandopoulos et al. 2003a). A few years later, Haralampous et al. state that, during regeneration, high temperatures can develop as well as significant axial temperature gradients (Haralampous et al. 2003, 2004a, Haralampous and Koltsakis 2004a,b). In this case, they believe that radiative heat exchange may become important and model this phenomenon by assuming black body behavior of the wall surface:

$$\dot{Q}_{rad}=\left(\frac{N_c}{2}\right)\left[4d_I\sigma\left(T_f^4-\frac{\int_I T_f^4 FdA}{d_I^2}\right)+4d_{II}\sigma\left(T_f^4-\frac{\int_{II} T_f^4 FdA}{d_{II}^2}\right)\right], \tag{151}$$

where F is the view factor of the channels with the above equation modified to remain consistent with the volumetric model description. Model results illustrate that the effect of radiation becomes important above approximately 600°C–700°C; hence, it can improve model accuracy during uncontrolled regeneration events.

The contribution due to reaction of the particulate develops from the historical summary described in Sections 2.4 and 2.5.2. Skipping ahead to recent efforts, Depcik and Assanis express the contributions due to PM combustion as

$$\dot{Q}_{reac} = -\left(\frac{N_c}{2}\right)\left(\frac{m_d \Delta H_{reac}}{\rho_d}\right)\dot{S}_{C_{(s)}}, \tag{152}$$

with oxidation only occurring on half the number of total channels because of the lack of PM in the outlet channel.

This expression includes the heat of reaction that is a function of the combustion reaction modeled. Section 2.4 indicates the derivation of the gaseous amount of oxygen lost as $\dot{S}_{O_2} = -\alpha_1 k_1 S_p \rho_s Y_{s,O_2}$. Because the mass added to the gas equals the mass of PM reacted, the generalized oxygen combustion Eq. (63) can be used to calculate the respective PM loss. Incorporating both oxidation options, the source term for heat addition equals

$$\dot{S}_{C_{(s)}} = -\frac{W_{C_{(s)}}}{W_{O_2}} k_1 S_p \rho_s Y_{s,O_2} - \frac{W_{C_{(s)}}}{W_{NO_2}} k_2 S_p \rho_s Y_{s,NO_2}. \tag{153}$$

This value is equal to the total amount of PM that undergoes combustion requiring a modification for use in the mass equations through the PM and wall layers of Eq. (40) or Eq. (41) based on the number of discretizations in the respective layer:

$$\dot{S}_{mass} = \frac{\dot{S}_{C_{(s)}}}{N_s\text{-}1}. \tag{154}$$

Note that the above discretization is for the Depcik and Assanis model where PM loading only happens in a cake layer on the surface.

Koltsakis and Stamatelos (1996a,b) modify the Bissett and Shadman (1985) model by accounting for incomplete PM oxidation. In the energy equation formulation, this only influences the reaction enthalpy in Eqs. (21) and (152) by including a reduction in exothermic energy from the partial production of CO. In the same year, they modify the perturbation analysis involving this equation to include a metal additive catalytic reduction component and the reaction enthalpy that results (Koltsakis and Stamatelos 1996a,b). However, its inclusion does not appear in the dimensional version of this equation, but its importance is noted with respect to the axial filter energy equation.

In the previously mentioned literature, researchers write the expression for the heat of reaction added to the filter energy equation a number of different ways. This all depends on how they express the reaction rate equations; for example, Haralampous et al. deviate from the traditional Bissett version, whereas Konstandopolous et al. follow Bissett's method with a few differences in their molar PM combustion reactions. Compiling and analyzing these versions is beyond the scope of this article; however, their contributions are noted. Of interest, Depcik and Assanis use average values for the density and oxygen mass fraction within their calculation of Eq. (153). However, Haralampous et al. correctly note that this expression should include integration in the y-direction over the cake layer and deep-bed filtration to capture the heat released as a function of local oxidation mass fractions. This was done originally by Bissett as he solved for the local O_2 profile analytically in his efforts.

The catalytic reaction term involves the impact of direct PM conversion through a catalyzed surface (Konstandopoulos and Kostoglou 1999), metal additives interacting with the PM in the cake and wall layers (Koltsakis and Stamatelos 1996a,b), and any gaseous phase reactions occurring in the wall (Konstandopoulos and Kostoglou 2000, Konstandopoulos et al. 2000, Kandylas et al. 2002). Summarizing the first two into a generalized format for incorporation is difficult because of the different versions in the literature. However, one can look toward catalyst modeling to express the reaction rate through the wall layer (Depcik and Srinivasan 2011):

$$\dot{Q}_{cat} = \dot{R}_{\text{direct PM}} + \dot{R}_{\text{additives}} + \frac{S_{ca} N_c}{t_f} \sum_{j=1}^{NM} \left(\int_{y=t_d}^{t_d+t_f} \dot{R}_j \bar{h}_j dy \right). \tag{155}$$

Assuming that catalytic reactions only occur in the wall layer, its impact includes a summation through this layer as a function of local rates that is averaged over the thickness of the wall (effectively an average heat of reaction over the wall later). The term S_{ca} is the catalytic surface area of the reactive material in the wall.

The last term is only important when computing the gas temperature profile through the wall as in Section 2.3

via Eqs. (57) and (58). Depcik and Assanis omitted the corresponding heat transfer from the gas to the wall in their model:

$$\dot{Q}_{inner}=\frac{\tilde{a}\left[h_c V_d\left(\overline{T}_s-T_f\right)+h_c V_f\left(\overline{T}_w-T_f\right)\right]}{1-\varepsilon_p}, \tag{156}$$

which uses average gas temperature values in the PM $\left(\overline{T}_s\right)$ and wall $\left(\overline{T}_w\right)$ layers, respectively. Because the gas temperature becomes the filter temperature nearly instantaneously, this term is not important but is required in this review for completeness.

2.6.2 Temperature gradients across the soot cake and the wall

Haralampous and Koltsakis (2002) explicitly indicate the porosity of the layers in the calculation of the density and thermal conductivity. The apparent density of the PM layer is then a factor of the solid phase properties assumed as solid carbon:

$$\rho_d=\left(1-\varepsilon_p\right)\rho_{C_{(s)}}, \tag{157}$$

with the conductivity a weighted factor between the air and carbon properties:

$$\lambda_d=\varepsilon_p\lambda_{air}+\left(1-\varepsilon_p\right)\lambda_{C_{(s)}}. \tag{158}$$

Of importance, Bissett and Shadman explicitly indicate these variables as bulk values, taking into account the porosity of the medium; hence, the variables in Eq. (21) are equivalent to these above equations.

As noted by Bissett and Shadman, the following dimensionless number is an indication for the temperature uniformity in the PM layer:

$$\Xi=\frac{c_p\rho_w u_w t_d}{A_{flt}\lambda_d}, \tag{159}$$

where A_{flt} is the filtration area and Ξ is the Peclet number calculated for the particulate layer width. When Ξ has a sufficiently small value, the thermal gradient is negligible. Therefore, temperature gradients might occur under the conditions of high flow rates per filtration area as well as the presence of large deposit layer thickness. Moreover, temperature gradients can occur when localized processes (e.g., reactions) produce gradients on a length scale smaller than A_{flt}/t_d.

Bissett and Shadman assumed a bulk density of 550 kg m^{-3} and a bulk PM conductivity of 0.84 W mK^{-1}. As mentioned above, these early estimations of PM properties have been since then revised by the increasing knowledge of the structure of the deposited PM. It would be reasonable to use a typical average soot cake density of 75 kg m^{-3}, which corresponds a porosity value of 0.97. For this porosity value, the bulk thermal conductivity is 0.108 W mK^{-1}. Using these values, the parameter Ξ is expected to be almost two orders of magnitude higher than the values assumed in the justification of the Bissett and Shadman model.

Haralampous and Koltsakis solve for the advection-conduction energy equations of Eqs. (21) and (22) to calculate for the temperature field within the soot cake for various regeneration modes (Figure 29). The calculated temperature gradients result from the inability of the low-conductivity PM to diffuse the heat generated in the layers close to gas entrance. Bearing in mind that the reaction rate depends exponentially on temperature, the front PM layers will react faster than the layers close to the wall. Consequently, the overall PM consumption rate is always higher compared with what would be expected from uniform soot cake temperature model. They conclude that the differences could be significant in the case of regenerations under extreme soot loadings of the order of 10 g l^{-1} or more, as demonstrated in Figure 30. The same figure shows a critical effect of soot porosity.

2.7 Numerical methods

In Bissett's 1984 article, he nondimensionalizes the governing equations and uses the differential algebraic solver

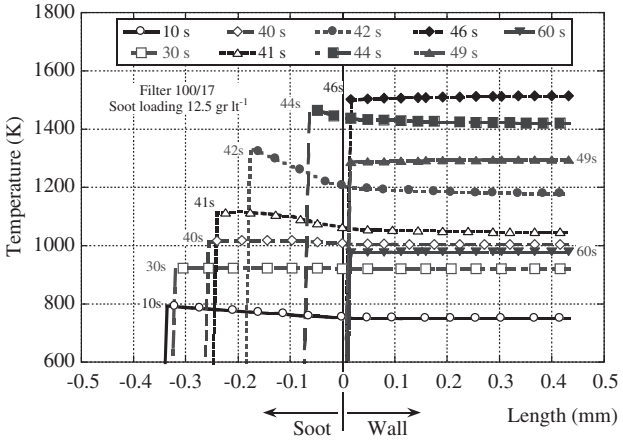

Figure 29 Computed temperature profiles inside the soot layer and the ceramic wall as a function to time (Haralampous and Koltsakis 2002).

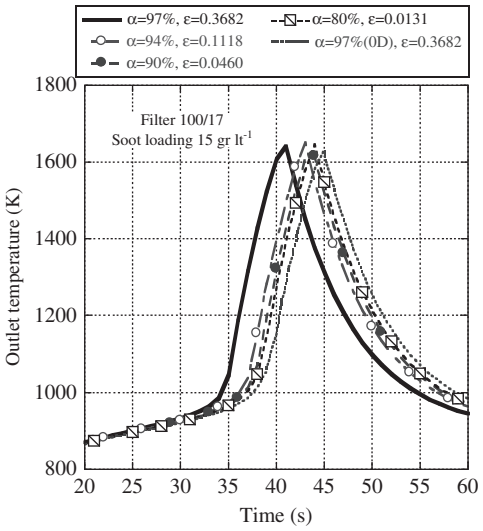

Figure 30 Effect of soot porosity on the regeneration behavior (Haralampous and Koltsakis 2002).

LSODI to solve the fluid dynamics and ideal gas law equations simultaneously (Hindmarsh 2002). This solver is still in use today as evidenced by the Depcik and Assanis articles. Koltsakis and Stamatelos (1997a,b) use a different approach starting with their 1997 article by using time marching via a fourth-order Runge-Kutta technique and employing a computationally efficient iterative approach to solve the flow field in the inlet and outlet channels. The models of Konstandopoulos et al. solve for the equations using the combination of a two-point boundary value problem for the mass, momentum, and energy equations along with incorporating the method of lines via a second-order finite difference approximation and a variable step, prespecified accuracy explicit Runge-Kutta integrator for the particle mass balance (Konstandopoulos and Kostoglou 1999). They employ the implicit Nyström method to solve for the flow equations and incorporate a Netwon-Raphson method for convergence.

Recent work by Sprouse et al. (2011) includes two different numerical solvers incorporated in MATLAB: one for the differential algebraic equation (DAE) system of equations and one through the differentiation of the algebraic constraint equation (ideal gas law) to complete an ordinary differential equation (ODE) system:

$$\frac{d\rho}{dz}=\frac{1}{RT^2}\left(T\frac{dp}{dz}-p\frac{dT}{dz}\right). \tag{160}$$

In the numerical code within MATLAB, the ode15i option (solves implicit equations using backward differentiation formulas) is employed for the DAE solver, whereas the ode15s (variable-order numerical differentiation formulas) option is employed for the ODE solver. The method of transforming a DAE system to a system of ODEs by differentiating the algebraic equation is a common procedure for numerical integration of DAE sets (Shampine et al. 1999). Both model solutions produced nearly identical results; however, the ODE solver methodology required approximately 40% more time.

3 Using the DPF model

A thorough history of the DPF model based on Bissett and Shadman's early work illustrates that the model now includes a greater ability to simulate active and passive regeneration events along with soot loading within the filter wall and on the cake layer. This section indicates the lessons learned from using the model and how this allows researchers to advance the DPF field of practical usage.

3.1 NO_2 impact on regeneration

Filter regeneration with oxygen occurs with noticeable rates at temperatures above 500°C–550°C, which are rarely met under typical operating conditions. On the other hand, NO_2 is highly reactive with soot (Cooper and Thoss 1989). NO_2 is able to oxidize soot at temperatures as low as 250°C, which can be encountered in diesel exhaust during normal driving cycles. However, NO_2 is present in diesel raw exhaust at very low concentrations (5–15% of total NO_x or <50 ppm), which are not sufficient to provide the required reaction rates.

The concentration of NO_2 in the exhaust gas entering the filter can be increased by placing upstream of the filter an oxidation catalyst, which oxidizes NO to NO_2. This is the main idea underlying the continuously regenerating trap concept, which is the trade name of a system composed of a selective oxidation catalyst placed directly upstream of the particulate filter (Cooper et al. 1990). At temperatures of 300°C–350°C, the oxidation catalyst oxidizes a proportion of the NO in the exhaust stream to form NO_2, increasing the NO_2 fraction to approximately 50% of total NO_x (Hawker et al. 1997, Allansson et al. 2002).

To model efficiently catalyzed and uncatalyzed DPF systems, the knowledge of the rate laws for the uncatalyzed soot reactions is necessary. The published works deal mostly with reaction rate studies at laboratory scale using synthetic soot or synthetic gas. A comprehensive study dealing with the reaction kinetics of various soot

types under a wide range of laboratory conditions was recently published by Tighe et al. (2011). Kandylas et al. (2002) presented an *in situ* methodology to determine the kinetics of soot oxidation with O_2 and NO_2 in real engine conditions. The rate laws for soot oxidation with O_2 and NO_2 were derived from measurements of soot consumption during steady-state operation at various conditions and filter configurations. The soot consumption was calculated based on a methodology to calculate the soot mass as a function of the measured pressured drop, mass flow rate, and temperature, as described in Haralampous et al. (2004b,c). NO_2 was additionally produced by an oxidation catalyst placed in front of the filter. The results of these measurements can be summarized in the form of an Arrhenius plot, as shown in Figure 31.

3.2 Oxygen diffusion impact on regeneration

"Uncontrolled" regenerations typically occur at conditions of low flow rate and high oxygen content with high initial filter temperatures. These situations happen when the engine switches to idle mode after a period of high-temperature operation. The simulation work presented in Haralampous and Koltsakis (2004a,b) discusses the importance of including the transport-reaction coupling Eqs. (69), (70), (75) and (76) for the calculation of species concentration in the DPF channels. To simulate an "uncontrolled" regeneration condition of a filter 2.5 l in volume, the researchers assumed that the initial filter temperature is uniform at 600°C along with a constant mass flow rate at 0.01 kg s^{-1} and oxygen content in the incoming gas equal to 15%. The inlet gas temperature decreases

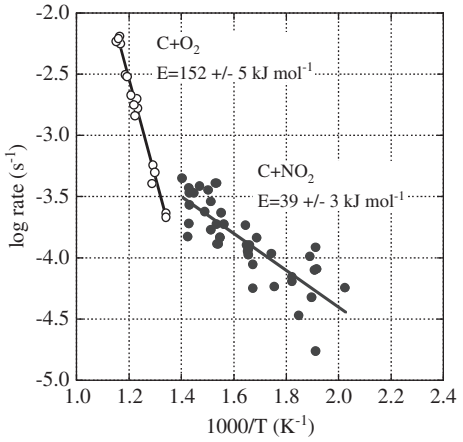

Figure 31 Arrhenius plots for uncatalyzed reaction of soot with O_2 and NO_2 obtained from experiments on the engine bench (Haralampous et al. 2004e).

asymptotically from 600°C to 300°C with a response time of the order of 20 s.

Figure 17 presents the computed wall temperatures at different axial positions in the filter channel, assuming an initial PM loading of 12 kg m^{-3} with and without inclusion of O_2 diffusion effects. Notably, this loading corresponds to an extreme case, whereas most researchers study loadings that range up to 7 g l^{-1} for production cases. The oxygen diffusion phenomenon affects the evolution of filter temperatures, especially the maximum temperature with a difference indicated between the two simulations of approximately 400°C. Such deviations are critical for model applications concerning the ability of the filter material to withstand severe regeneration conditions

The computed profiles of O_2 concentration along the filter for the two modeling assumptions presented in Figure 32 reveal the O_2 diffusion impact. The results correspond to the time of maximum reaction rate, and in the left graphs, the inlet channel O_2 concentration at the specific time drops suddenly from 15% to almost zero at an axial position approximately 100 mm from entrance. The concentration again increases slightly toward the rear part of the filter because of diffusion from the outlet back to the inlet channel. The figure also illustrates that O_2 diffusion enhances the reaction rate in the middle part of the channel. It is also interesting to note that a higher O_2 concentration of the outlet channel near the filter exit exists with respect to the corresponding concentration in the inlet channel. This concentration difference drives O_2 diffusion back from the outlet channel to the PM layer, thus enhancing the overall reaction rate.

Moreover, Figure 32 illustrates the effect of O_2 diffusion on the evolution of PM layer thickness along the filter channel during regeneration starting with a high PM loading. The left graph shows that the diffusion-induced increase of O_2 availability at the middle part of the filter results in a preferential PM consumption compared to the rear part of the filter. This is not the case in the simulation result without O_2 diffusion. Examining the O_2 intralayer profiles at different axial points along the filter, as predicted by the two models, demonstrates the implications due to oxygen availability. The oxygen gradients in the diffusion model imply oxygen transfer from both the inlet and the outlet channels. As expected, close to filter exit (z/L=0.9), the concentration of oxygen is lower to that expected by the reaction-only model, because diffusion results in overall increased oxygen consumption up to that axial point. The authors performed preliminary validation of this reaction-diffusion model using the Miyairi et al. (2001) experimental efforts. Their experiment involved the regeneration of a cordierite filter with a 200 cpsi (31 cells cm^{-2}) structure and

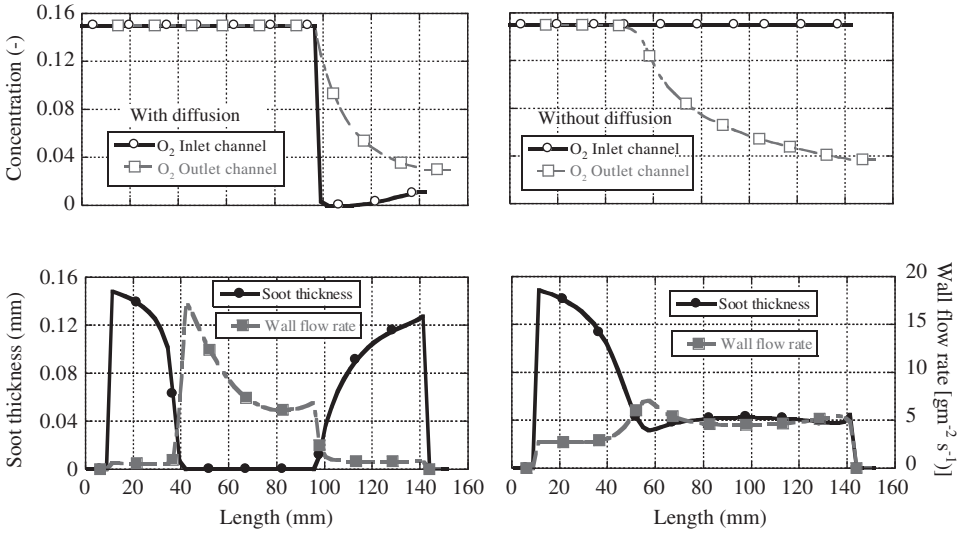

Figure 32 Profiles of O_2 concentration in the inlet and outlet channels during uncontrolled regeneration with 12 kg m^{-3} initial PM mass at time=42 s.
Also shown is the wall-flow velocity and the PM layer thickness at the same time (Haralampous and Koltsakis 2004a,b).

12 mils (0.3048 mm) wall thickness in a propane burner. The regeneration temperature was 600°C and the flow rate equal to 0.014 kg s^{-1}. The regeneration events involved different PM loadings and the data include measuring 20 different axial and radial positions for the filter temperature. To simulate these experiments, it was necessary to employ the extended 2D regeneration model (Haralampous et al. 2003) involving Eq. (145) in the axial filter energy equation. Figure 33 provides the results of two different simulations with and without diffusion effects. For comparison, the figure presents the maximum computed filter temperature versus the respective measurement as a function of initial PM loading. When neglecting diffusion, the calculated maximum temperature agrees with the measured values for low to medium PM loadings up to 8 kg m^{-3}. At higher PM loadings, which are namely of interest for filter integrity in uncontrolled regenerations, the discrepancy is critical. On the other hand, the inclusion of oxygen diffusion modeling provides a very good agreement with the respective measured data for the complete range of PM loadings.

3.3 Catalytic regeneration

Due to the relatively low temperatures of the diesel exhaust gas, catalytic assistance in the form of fuel-borne catalysts (FBCs) (Salvat et al. 2000) or catalytic filter coatings (catalytic DPF or CDPF) (Suresh and Johnson 2001) is currently the state-of-the-art for commercial systems. In these cases, diesel engine fuel injection and control systems continue to support the regeneration system by increasing the exhaust gas temperature through postinjection to initiate the regeneration process. FBCs act to accelerate the reaction of oxygen with soot by reducing the regeneration temperature to approximately 500°C instead of 600°C in the case of noncatalytic systems. The situation is somewhat different in the case of catalytically coated filters. Most commercial technologies involve coating or impregnating the filter wall with platinum-based catalysts that are effective in promoting the oxidation reaction of NO, which is present in the raw diesel exhaust, to NO_2. As mentioned previously, the latter is a strong oxidizing agent and is able to react with deposited soot at temperatures as low as 250°C. However, because NO_2 forms on the catalytic wall, which is downstream of the

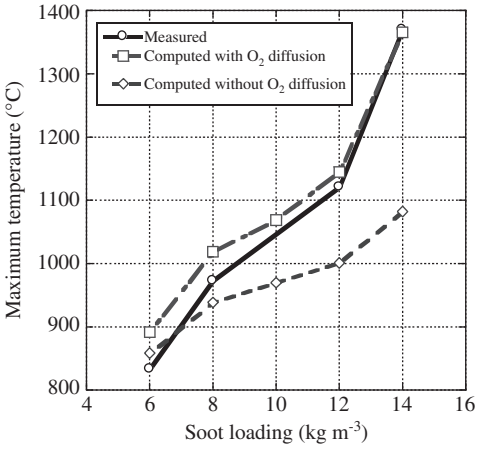

Figure 33 Comparison of experimental and predicted maximum temperatures during regeneration as a function of PM loading (Haralampous et al. 2003).

soot cake layer, the reaction of this species with soot would not be possible unless NO_2 is able to diffuse back into the cake layer driven by a concentration gradient. Moreover, one has to take into account that, in typical filter wall structures, soot partially fills the pores in the wall during loading events. Therefore, a certain amount of soot will actually be downstream of the catalytic sites for NO_2 generation (Konstandopoulos and Kostoglou 1999, 2000, Konstandopoulos and Kladopoulou 2004).

Soot oxidation studies using real exhaust conditions have proven that the reaction rates are proportionally increased by the concentration of FBC in the soot (Haralampous et al. 2004b,c), which linearly increases with additive concentration in the fuel. Moreover, FBC concentration affects the soot emissions rate and fuel consumption, both of which may vary as a function of engine operating point. Testing the potential of a FBC or CDPF to reduce the regeneration temperature traditionally happens via a so-called "balance-point" test in which the engine operates at constant speed and the operator increases torque in a stepping manner resulting in a rise in inlet gas temperature. Figure 34 illustrates a typical example that presents the pressure drop evolution of a preloaded CDPF in a temperature range between 300°C and 400°C. The definition of the balance point temperature is the value of temperature at which the pressure drop is nearly constant over time. From indicative literature (Haralampous et al. 2004b,c), the balance point temperature for an uncatalyzed filter measured on a mid-sized diesel engine has been reported equal to 470°C, whereas a FBC system will lower the balance point to 370°C and 350°C with a 1% or 2% Ce-based additive concentration in soot, respectively. In comparison, a catalyzed filter lowers this temperature closer to 320°C.

The low balance point temperature of the catalyzed filter is due to its ability to form NO_2 at temperatures between 300°C and 400°C. Although the NO_2 is mainly formed downstream of the soot cake layer, it may diffuse back into this layer and contribute substantially to the regeneration rate. This has important implications, because temperatures of the order of 350°C can often occur in real-world driving scenarios leading to partial filter regenerations and less frequent fuel-consuming forced regenerations due to postinjection. At higher temperatures (>500°C), NO_2 does not form effectively in the catalyzed filter due to thermodynamic equilibrium limitations of the NO and O_2 reaction. Therefore, the reaction rate of the catalyzed filter in a high-temperature regeneration situation is much lower compared with the case of a FBC regeneration system and almost equal to the uncatalyzed system. The regeneration mechanisms and the respective

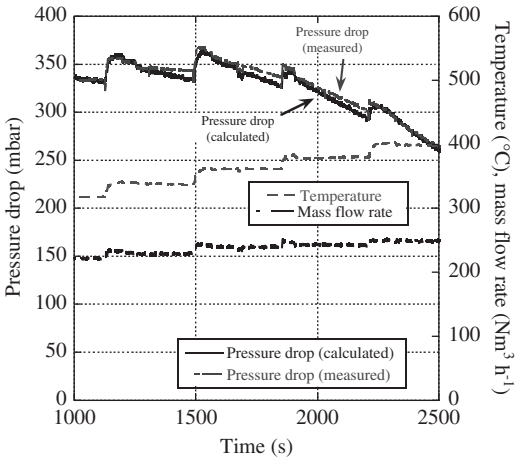

Figure 34 Measured versus computed pressure drop during testing with step temperature increase (Haralampous et al. 2004e).

necessary modeling detail may vary considerably depending not only on the catalyst used but also on the regeneration mode and operating conditions. Table 1 summarizes a number of regeneration mechanisms and indicates which phenomena are dominant in FBC and CDPF systems for the different regeneration modes.

With the aid of modeling and experiments, it is possible to analyze this impact of NO_2 back-diffusion within the soot cake layer and filter wall for catalyzed filters. For a typical catalyzed filter and a medium size car engine, operating at favorable conditions (350°C) of moderate to high speed and load, NO_2 can be generated in the filter to react with soot. Figure 35 shows the computed soot mass in the filter during the steady-state test with and without considering diffusion effects. For a better understanding of the NO_2 diffusion phenomena during regeneration, Figure 36 shows the computed axial profiles of NO_2 in the inlet channel at the initiation of the test. As expected, for the reaction-only model, the NO_2 concentration in the inlet channel remains constant, whereas the reaction-diffusion model predicts a slow exponential decrease across the inlet channel. This is because, for the reaction-only model, a one-way flow propagation through the wall is occurring resulting in an analogous outcome to Bissett's early constant O_2 concentration levels in the inlet channel via Eq. (11). The concentration profile of NO_2 in the soot layer and the wall is shown in Figure 37 at two different axial points at test commencement. Focusing on Figure 37A (near filter entrance) and the reaction model, the NO_2 concentration is initially decreasing as the flow enters the soot layer due to reaction with soot until it reaches full consumption. After entering the wall region, the concentration rises steeply in the beginning and then more

Table 1 Evaluation of the importance of regeneration mechanisms for different catalyst-based systems depending on the regeneration mode (Haralampous et al. 2004a).

Mechanism/model feature	FBC system				CDPF system			
	Controlled		Uncontrolled		Controlled		Uncontrolled	
	<450°C	>450°C	Low m_{soot}, T	High m_{soot}, T	<450°C	>450°C	Low m_{soot}, T	High m_{soot}, T
$C+O_2$	o	+	+	o	o	++	++	+
$C+NO_2$	+	o	o	o	++	+	o	o
O_2 diff	o	o	o	++	o	o	o	+
NO_2 diff	+	o	o	o	++	o	o	o
C+FBC	++	++	++	+	-	-	-	-
$NO \leftrightarrow NO_2$	-	-	-	-	++	+	o	o

o, not important; +, important; ++, very important. Controlled regeneration: steady inlet conditions, medium to high flow rate; uncontrolled regeneration, low flow rate, initial DPF temperature>>BPT. All cases assume upstream DOC.

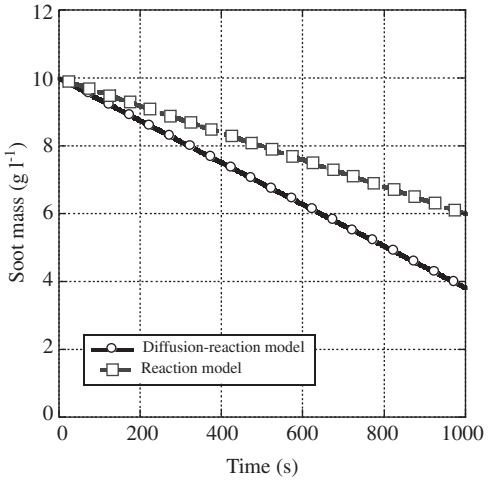

Figure 35 Calculated PM mass in the filter with and without accounting for diffusion (Haralampous and Koltsakis 2004a,b).

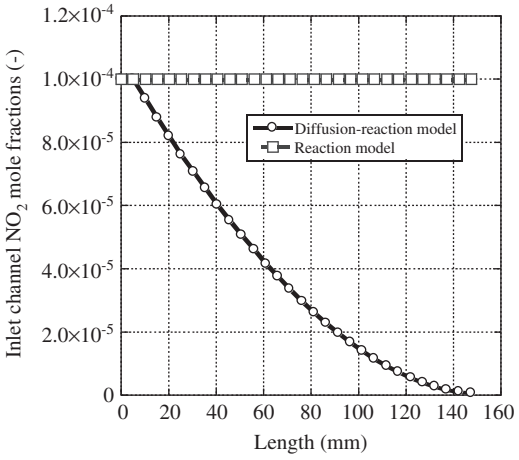

Figure 36 Computed profiles of NO_2 concentration in the filter inlet channel with and without accounting for diffusion (Haralampous and Koltsakis 2004a,b).

slowly, approaching chemical equilibrium at wall exit as the entering NO undergoes an oxidation reaction that is equilibrium limited, for example, $NO+1/2O_2 \Leftrightarrow NO_2$.

In the diffusion-reaction model, the NO_2 produced in the wall is "back diffused" in the soot layer and a slow increase in NO_2 concentration is evident from the soot layer region. Meanwhile, a reduction of the concentrations in the wall is observed due to the same phenomenon additionally resulting in smaller concentrations for the outlet channel. An added NO_2 flow is induced due to the concentration gradient between the inlet channel and the soot layer resulting in the axial profile outcome of Figure 36. Moreover, similar behavior is observed in Figure 37B (near filter exit). Because the inlet NO_2 concentration is very low from the engine (as also shown in Figure 36), back-diffusion is responsible for supplying the soot layer with additional NO_2.

Figure 38 presents the regeneration rate as a function of temperature for two different initial soot loadings. The reaction rate increases with temperature as expected, although not in an exponential manner. This is because the overall soot consumption rate is controlled by the rate of soot oxidation with NO_2 along with NO_2 production in the wall, which is limited by thermodynamic equilibrium at higher temperatures. Figure 39 presents the percentile contribution of back-diffusion phenomena to overall reaction rate. This shows that the reaction-only model predicts reaction rates that are 25–35% lower compared with those predicted by the reaction-diffusion model with the discrepancy larger at lower temperatures. The effect of flow rate and NO_x concentration in terms of the mean reaction rate is indicated in Figure 40. This figure finds that the impact of the diffusion phenomena is more pronounced at lower flow rates. This is to be expected because back-diffusion

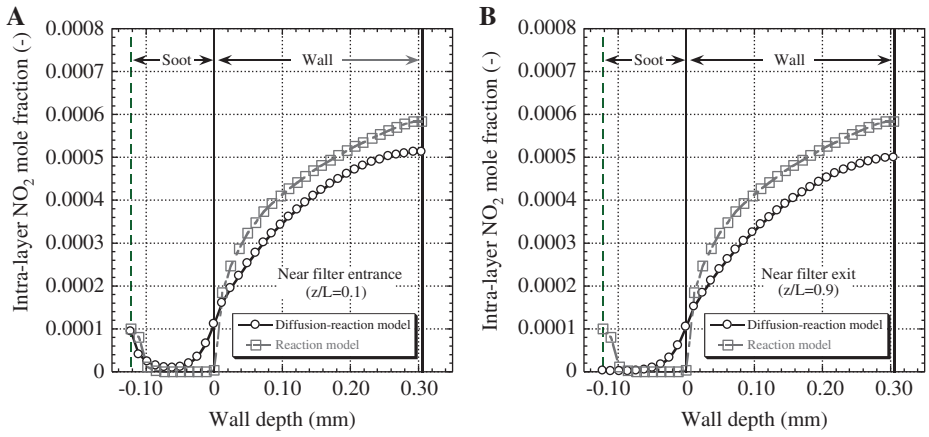

Figure 37 Computed profiles of NO_2 concentration in the PM layer and the filter wall with and without accounting for diffusion: (A) near filter entrance and (B) near filter exit (Haralampous and Koltsakis 2004a,b).

in the soot layer is dependent on the Peclet number of the flow through the porous layer and wall. The results demonstrate that there is not a large dependency on initial NO concentration. In Figure 41, the effects of tortuosity on the percentile contribution of diffusion are shown for tortuosity values ranging from 1 to 10. The sensitivity of the results on tortuosity is very important, especially for values below 3. These results emphasize the importance of accurate determination of the species effective diffusivity in the porous wall and the soot layer.

3.4 Use of DPF as an oxidation catalyst

The installation of most commercial DPFs occurs downstream of a diesel oxidation catalyst (DOC). The presence of the oxidation catalyst upstream to the DPF ensures the efficient reduction of CO and hydrocarbons during normal operation as well as during forced regeneration with postinjection (Banno et al. 2004). In the latter case, the exothermic reactions in the oxidation catalyst subsequently transfer energy to the DPF through the exhaust gas enthalpy and aid in regeneration of the DPF. In comparison, the purpose of a CDPF is to facilitate regeneration while minimizing the CO emissions during this regeneration event. Therefore, because catalyzed filters are efficient in oxidizing CO and hydrocarbons, it is theoretically possible to completely eliminate the oxidation catalyst (Maly et al. 2004, Mizutani et al. 2004).

Modeling of the combined mass-transfer and reaction phenomena in a CDPF was done originally by

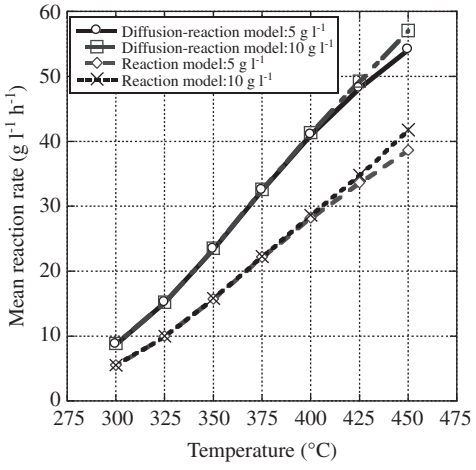

Figure 38 Mean reaction rate as a function of temperature for two different initial PM loadings (Haralampous and Koltsakis 2004a,b).

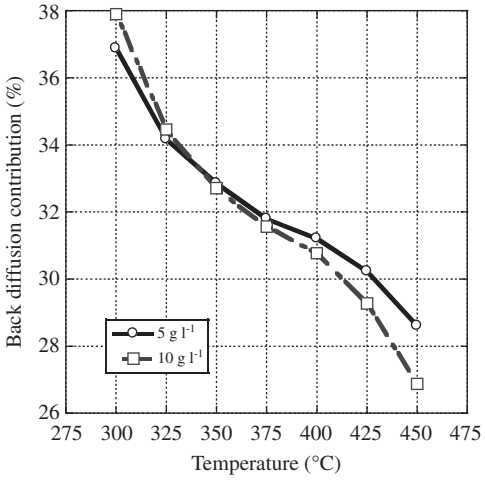

Figure 39 Percentile contribution of back-diffusion phenomena to overall reaction rate as a function of temperature for two different initial PM loadings (Haralampous and Koltsakis 2004a,b).

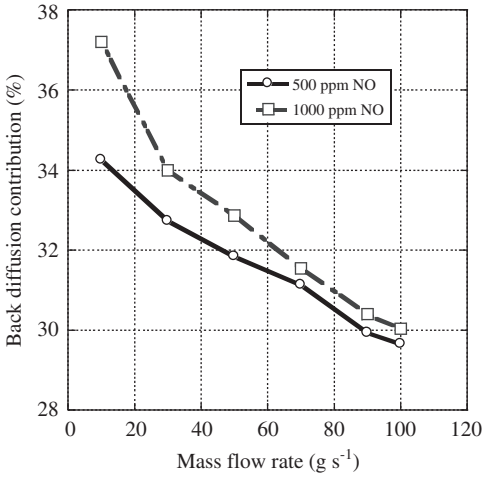

Figure 40 Percentile contribution of back-diffusion phenomena to overall reaction rate as a function of flow rate for two different NO_x concentrations (Haralampous and Koltsakis 2004a,b).

Knoth et al. (2005) using steady-state computational fluid dynamics. In addition, their work presents performance comparisons with flow-through DOC substrates in comparing oxidation effectiveness. The authors of this review article took a simplified approach to this model to reduce the computational load. This was accomplished by eliminating the species transfer effects from the inlet channel to the wall. The subsequent results indicate that flow-through-type structures have better conversion efficiencies than wall-flow style supports. In a more recent work of the same group (Votsmeier et al. 2007), results show that the above simplification is valid only at high flow velocities. They present a less complicated modeling approach claiming that the flow-through-type reactor is more efficient due to increased reaction residence time (Miller and Li 2000). A recent article (Dardiotis et al. 2006) involves modeling a CDPF using the transport-reaction coupling model in parallel with respective flow-through DOC simulations. This work uses DOC and CDPF models to analyze both systems concerning their gaseous species oxidation performance and is recapped here. Further details about the setup and conditions are given in Tables 2 and 3.

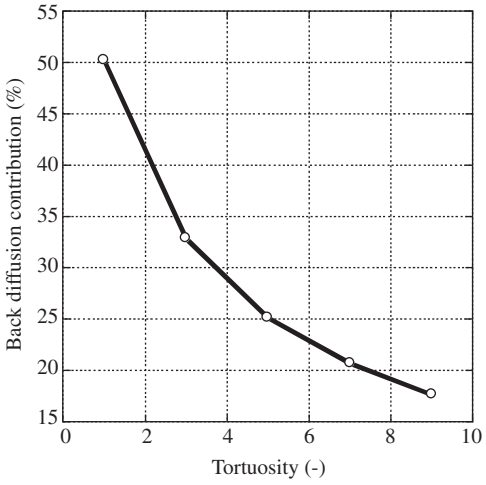

Figure 41 Contribution of diffusion phenomena as a function of tortuosity at one temperature (Haralampous and Koltsakis 2004a,b).

Two main factors differentiate the behavior of the CDPF compared with the DOC when it comes to the oxidation reaction. The first factor involves the axial velocity component; because half of the channels are plugged in a CDPF, the inlet channel axial velocity is higher compared with the DOC. The second factor regarding the CDPF involves the continuous loss of axial inlet bulk flow through the wall to the outlet channel until the axial velocity drops to zero at the rear plug. As the flow passes through the wall, oxidation of CO or HC happens, and as soon as the wall flow exits the wall, it mixes with the axial flow in the outlet channel. As an example, the axial profiles of CO and HC concentration along the outlet channel are shown comparatively for CDPF and DOC in Figure 42. Interestingly, the CO concentration of the gas exiting the CDPF is approximately the same as the respective concentration for the DOC, implying the same conversion potential for both devises, with the same overall dimensions and catalyst loading. This is because, in both systems, the phenomenon is kinetically controlled.

To make a thorough comparison between the flow-through-type DOC and the wall-flow CDPF, Figure 43

Table 2 Geometric and thermophysical properties of the DOC and CDPF (Dardiotis et al. 2006).

	DOC	CDPF
Substrate material	Cordierite	
Filter diameter	0.144 m	
Filter length	0.1508 m	
Plug length	—	0.005 m
Channel density	300 cells in^{-2}	
Wall thickness	3.048×10^{-4} m	
Substrate density	1250 kg m^{-3}	
Substrate permeability	—	5×10^{-13} m^2

Table 3 Exhaust gas concentrations used for the simulations (Dardiotis et al. 2006).

O_2 concentration	10%
CO concentration	100 ppm
HC concentration	90 ppm

presents CO and HC conversion maps obtained by the two models for a range of different practical flow rate/temperature combinations. There are no differences between the two systems with respect to CO efficiency because it is not limited by mass transfer for the tested conditions. Concerning the HC, the CDPF is slightly superior compared with the DOC at high flow rates. The mass-transfer limitation is more important in the case of hydrocarbons because they have the lower diffusivity among the species of interest. At high flow rate and high-temperature conditions, the HC conversion in the DOC becomes mass-transfer limited as opposed to the CDPF.

To continue this comparison of catalytic options, it is important to examine how heat transfer interacts with mass-transfer and chemical reactions during transient operation. This is particularly important during a cold-start event, which typically governs the emissions performance of a vehicle. For two systems of equal thermal mass, the CDPF warms up faster because of the efficient heat transfer mechanism of the flow through the wall. This is illustrated in Figure 44, which shows the calculated temperature profiles for both systems at different times during the warm-up phase. By defining the "active length" as the fraction of the reactor length above the light-off temperature, the study shows that the DOC is more efficient despite the shorter "active length". This is explained by the higher specific flow rate in the inlet CDPF channel compared with the respective flow rate in

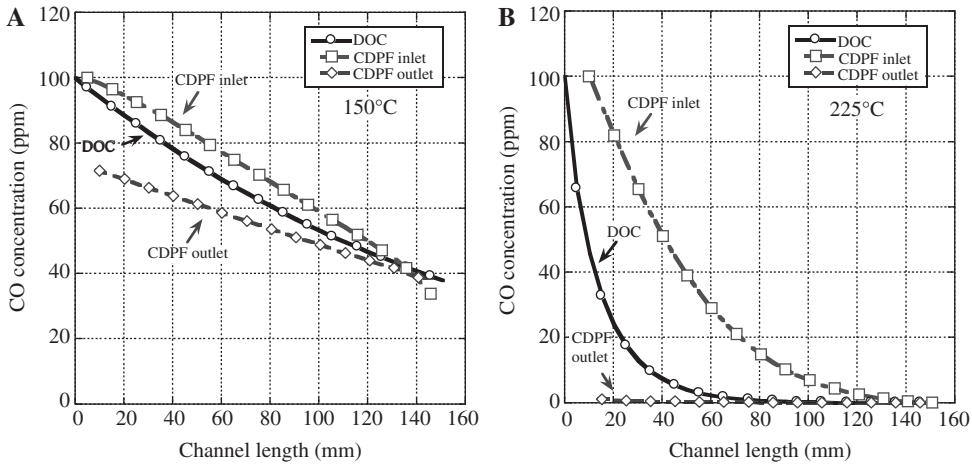

Figure 42 Computed CO concentration profiles in the channels of the clean catalyzed DPF and the oxidation catalyst: (A) 150°C and (B) 225°C (Dardiotis et al. 2006).

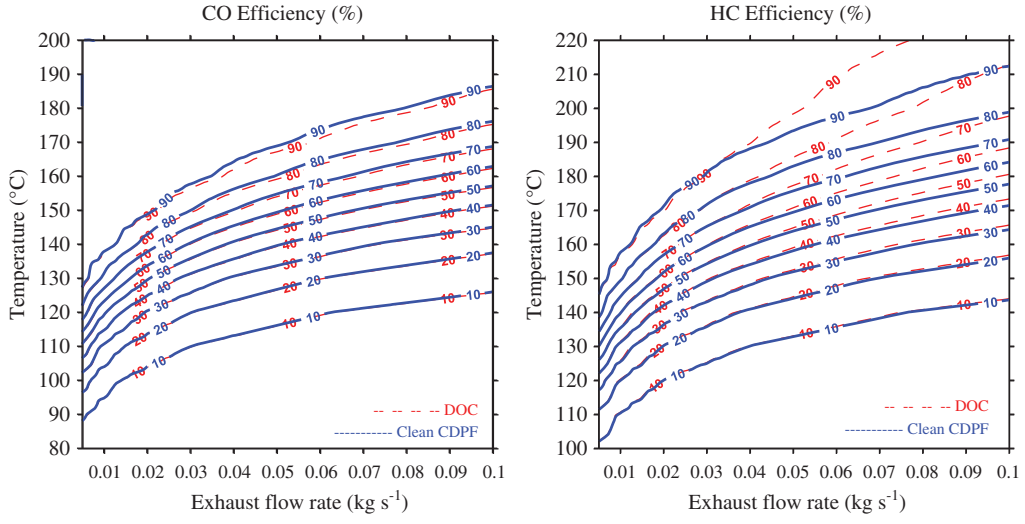

Figure 43 CO and HC conversion efficiency maps as functions of mass flow rate and temperature. Solid line, clean catalyzed DPF; dashed line: flow-through oxidation catalyst (Dardiotis et al. 2006).

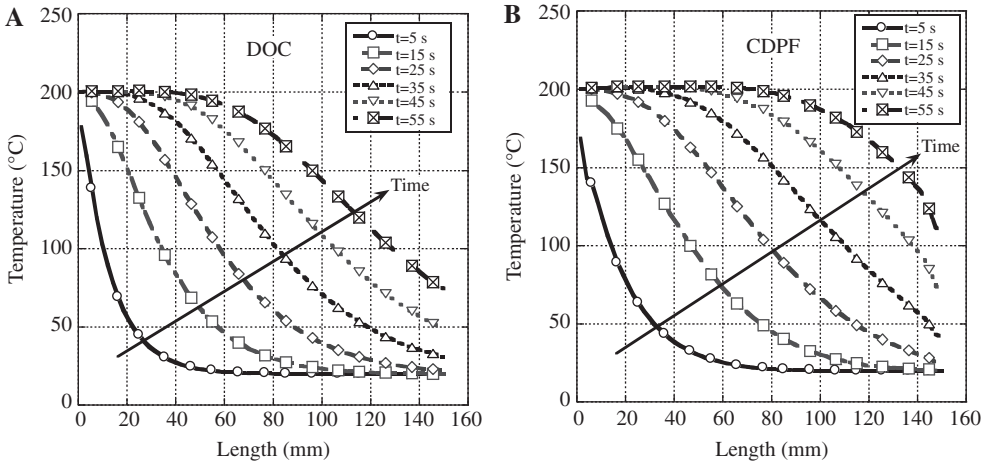

Figure 44 Wall temperature profiles at different times during the warm-up phase along (A) DOC and (B) CDPF (Dardiotis et al. 2006).

the DOC channels in the frontal area of the reactor. As a result, the residence time of the gas flow through the warmer inlet part of both reactors is longer in the case of the DOC. The longer residence time compensates for the shorter active length, leading finally to improved conversion of the DOC.

The temporal evolution of CO conversion efficiency is presented in Figure 45. As explained above, the DOC exhibits superior performance during the initial warm-up period. However, after sufficient warming (45 s from start), the CDPF equals or even exceeds the DOC performance. This is due to the lower mass-transfer resistance at fully warmed conditions, as explained through the presented steady-state results of Figure 43. The advantage of the CDPF is shown more clearly in the case of hydrocarbon conversion efficiency, included in the same graph.

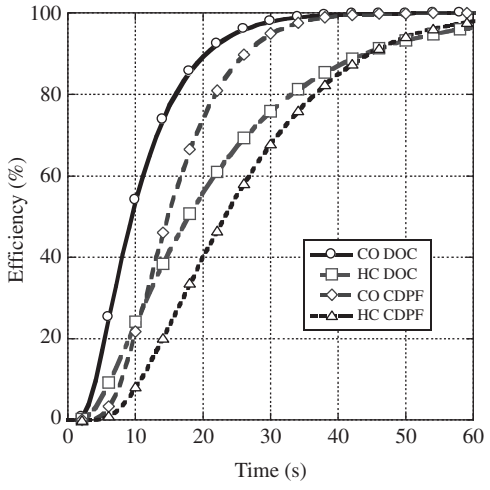

Figure 45 CO and HC conversion efficiency versus time during the transient performance (Dardiotis et al. 2006).

Summarizing, the conversion efficiency of the wall-flow catalyzed filter is a complex function of thermal, mass transport, and chemical phenomena occurring simultaneously. Under steady-state conditions, the CDPF has a higher oxidation conversion efficiency compared with a respective DOC with same dimensions and catalytic loading under mass-transfer limited conditions (high temperature, high flow rate). Under kinetically limited conditions, both systems perform identically. However, for transient operation from cold-start, it appears that the DOC would be preferred. In all cases, the results are relatively similar illustrating that the main differentiation between the two options will likely occur due to other parameters, including variations in cell structure, thermal mass, and quality and amount of wash-coat and precious metals.

3.5 Catalyst zoning

It has been suggested (Punke et al. 2006) that an axially nonuniform catalyst distribution could improve the cold-start behavior for CO and HC conversion in legislated driving cycles. This technology, usually termed “catalyst zoning”, typically employs depositing higher amounts of platinum group metals in the front part of the filter, which is more relevant during the critical warm-up phase. Catalyst zoning offers additional degrees of freedom in designing cost-effective CDPF systems, especially taking into account the high cost of precious metals. In this respect, it is important to support the design optimization with mathematical modeling to minimize the required demand of experimental testing.

To model a CDPF with locally variable catalytic activity, Dardiotis et al. (2008) use variable preexponential

terms in their reaction rates assuming a linear dependency on the local platinum group metals content. They model the zoned-coated DPF (zCDPF) as an oxidation catalyst to make direct comparisons under transient conditions simulating cold-start engine operation and a cool-down phase, which are most relevant for automotive emissions control.

Their study compares the transient performance characteristics of a zCDPF with different zoning schemes. They find that a zoning scheme with more catalyst in the frontal part is more beneficial for CO conversion in a simulated cold-start transient experiment. In the same test case, mass-transfer limitations in the front part of the zCDPF influence hydrocarbon conversion, which results in a lower conversion of the zoned systems under full-warmed conditions. In a simulated cool-down transient test, the system performance over the same zoning scheme was consistently inferior for both CO and HC. An analysis of the reactor performance through examination of the transient temperature and species profiles in the inlet and outlet channels illustrate that the conversion efficiency is a complex function of combined thermal, species transport, and reaction phenomena.

Further tests involving different zoning schemes include transient simulations with input data from a legislated driving cycle. The conclusions are in line with the simplified transient analysis, showing that a preferential coating of the frontal part reduces the cold-start emissions. However, the cool-down modes occurring later in the driving cycle may negate this advantage, which was especially the case for hydrocarbons.

3.6 Incorporation of DeNO$_x$ catalytic functionality

Solving for both the chemical species equations the channels and wall in the model simultaneously allows for the calculation of both DPF and lean NO$_x$ trap (LNT)-related functions (Koltsakis et al. 2007). As an example, Figure 46 presents the calculated NO$_x$ emissions downstream a combined LNT and DPF device during a lean/rich cycle at 350°C inlet temperature. The model allows for the calculation of the complex interactions of LNT functionality in conjunction with passive soot regeneration via the NO$_2$ pathway. Figure 47 shows the calculated NO$_2$ profiles through the soot layer and catalyzed wall at two different axial positions in the filter for two different instants corresponding to the start and the end of the lean (NO$_x$ storage) phase of the experiment shown in Figure 46. As shown in the top graph of Figure 47, the NO$_2$ concentration approaching the soot surface is a function of the axial position due to the advective mass-transfer occurring in the channel gas. The reaction of soot with NO$_2$ is sufficiently fast at this temperature to consume NO$_2$ in the soot phase. On the other hand, the catalytic coating promotes NO$_2$ formation and storage on the LNT component. Concurrently, the concentration gradient drives NO$_2$ back-diffusion to the soot layer. It is interesting to note that analogous phenomena also occur at the end of the lean operation mode, as shown in the bottom graph of the same figure. The differences arise from the fact that the LNT component has been partially saturated, thus influencing the rate of NO$_x$ storage, which in turn affects the overall NO$_2$ profiles in the catalyzed wall and soot layer.

Another concept under evaluation for coupled DeNO$_x$ and filter capabilities is a wall-flow selective catalytic reductant (WSCR; also referred to as SDPF or SCRF) system (Koltsakis et al. 2008, Lee et al. 2008, Ballinger et al. 2009, Cavataio et al. 2009a,b), that is, a filter with integrated SCR functionality. To achieve equivalent NO$_x$ conversion with the SCR catalyst, the authors use a similar volume to a traditional SCR catalyst. In the simulation effort, the model assumes uniform deposition of the catalytic coating in the WSCR wall. In real-world applications, the NO$_x$ conversion efficiency may be different if the manufacturer deposits the wash coat on the outlet channels or on the inlet channels of the filter. The investigation of this effect of wash-coat deposition pattern is within the capabilities of the mathematical model, but the authors did not include it in the study. Using the same reaction kinetics for an SCR catalyst model, Figure 48 presents the DeNO$_x$ performance of three configurations: DOC-SCR-DPF, DPF-SCR, and DOC-WSCR. The combined system presents similar warm-up behavior, with respect to NO$_x$ conversion

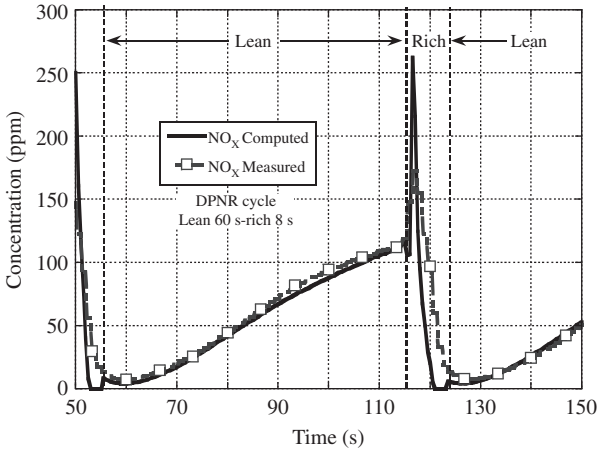

Figure 46 Measured versus simulated NO$_x$ emissions during a lean/rich cycle at 350°C inlet temperature (Koltsakis et al. 2007).

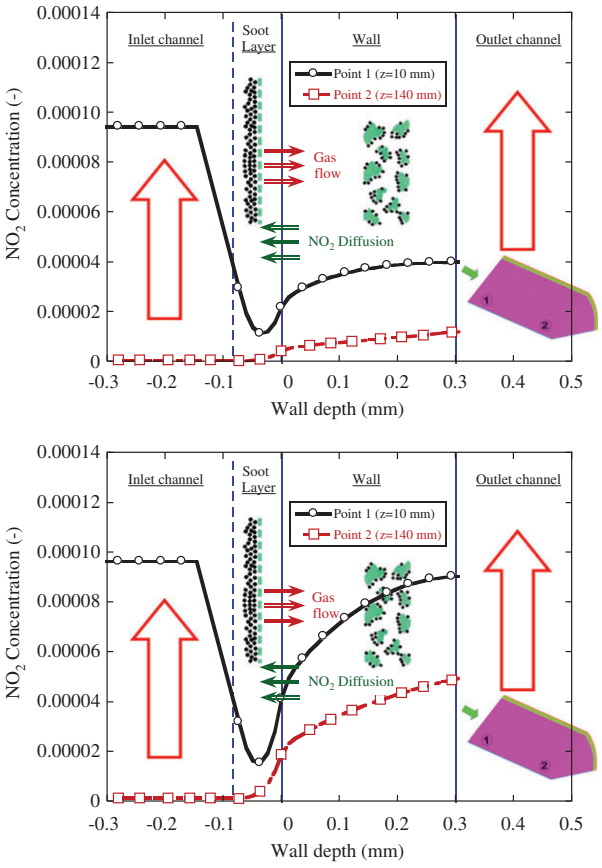

Figure 47 Calculated NO_2 profiles through the soot layer and filter wall at two different positions o f the LNT/DPF.
Top, at the beginning of the NO_x storage process (lean mode); bottom, just before rich mode (Koltsakis et al. 2007).

as with the DOC-SCR-DPF system, and faster compared with the DPF-SCR configuration. In the warmed-up part of the driving cycle, the DOC-WSCR system illustrates practically the same conversion efficiency as to the DOC-SCR-DPF system. During the extra-urban part of the driving cycle, the WSCR system appears to have slightly better conversion efficiency compared with the SCR system. The authors attribute this result to mass-transfer limitations in the case of the flow-through SCR monolith, which are not present in the case of the wall-flow WSCR monolith.

The simulation of a complete exhaust line through a combined mathematical model allows the evaluation of the passive regeneration performance of different exhaust system formulations. A quantification of this performance occurs by calculating the soot mass accumulation rate in the filter per kilometer driven in the New European Driving Cycle (NEDC):

$$\Delta m = (\text{soot mass filtered}) - (\text{soot mass oxidized}) \ [\text{mg km}^{-1}] \quad (161)$$

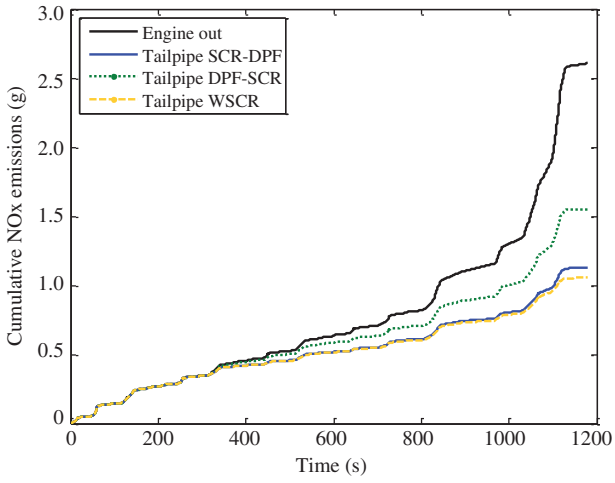

Figure 48 Comparison of the cumulative NO_x emissions over the NEDC for the three configurations simulated (Koltsakis et al. 2008).

The authors employ the model in simulation of different NEDC cycles with various initial soot loading levels at the beginning of the cycle. The accumulation rate depends on the initial soot loading mainly because the NO_2-based reaction rate grows with increased soot loading in the filter. Figure 49 illustrates the comparison between exhaust systems in the case of a Euro 4-compliant vehicle in terms of PM raw emissions (20 mg km^{-1}). The DOC-SCR-DPF formulation presents relatively little passive regeneration attributed to the fact that the upstream SCR system reduces nearly all of the available NO_2. Conversely, the DOC-DPF-SCR system may oxidize up to half of the filtrating soot by passive regeneration with NO_2, a clear advantage over the DOC-SCR-DPF formulation.

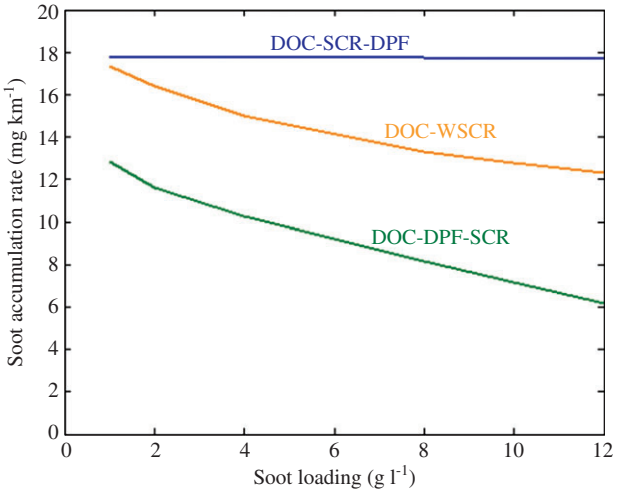

Figure 49 Passive regeneration performance of the two main exhaust line formulations (Koltsakis et al. 2008).

4 3D filter modeling

Although 2D, axisymmetric modeling of the regeneration process is sufficient in the case of cylindrical nonsegmented filters, the heat transfer problem is more complicated in the case of real-world filters. Most commercialized filters are segmented SiC filters and some of them are oval shaped. The presence of adhesive cement layers inside the filter structure influences local heat transfer, the flow distribution in adjacent channels, and consequently the complete evolution of regeneration in the filter. Moreover, 3D effects may arise from asymmetric flow conditions at the entrance of the filter.

4.1 Inlet flow distribution

An important aspect of 3D DPF regeneration modeling is the prediction of the transient flow distribution at filter inlet during regeneration. Even if the total gas flow rate at DPF inlet is constant during regeneration, the following parameters influence the flow distribution entering the filter:

- Inlet cone geometry,
- Soot distribution in the filter, and
- Temperature distribution in the filter affecting the local flow resistance.

The modeler may be able to neglect the effect of inlet cone geometry if the manufacturer designs the cone shape to eliminate flow maldistribution at DPF entrance due to flow separation. On the other hand, radially nonuniform soot distribution occurs commonly in practice due to partial filter regeneration events. Temperature nonuniformities in the filter also occur, but their effects on inlet flow distribution are comparatively smaller, as shown by Haralampous et al. (2003).

From the modeling perspective, after the discretization and grouping of the DPF channels, the flow distribution for each group of channels can be computed using an iterative procedure, as suggested by Koltsakis et al. (2005). Each group calculation begins through the assumption of an initial mass flow rate followed by the solution of the system of equations resulting in a pressure loss value for each representative channel. The calculation of the total pressure drop then occurs followed by corrections to the assumed mass profile. This trial-and-error method continues until the pressure drop calculated in every sector becomes equal. The authors benchmark this approach against respective CFD calculations using commercial tools with validated agreement in cases illustrating extreme flow maldistributions due to temperature and soot loading local nonuniformities.

4.2 Inlet temperature profile

The inlet flow nonuniformity is closely related to an inlet temperature profile due to the simultaneous development of flow and thermal boundary layer, in the pipes and cone upstream of the DPF. Lower temperatures are expected near the periphery due to steady-state heat losses to the ambient and the transient heat-up of the pipes. Therefore, this thermal boundary layer depends on the surface temperature of the metal pipe and can be time dependent.

The thermocouple measurements can offer a good indication about the inlet temperature profile as discussed by Koltsakis et al. (2005). Not surprisingly, the channel near the filter periphery heats up at a slower rate and exhibits an exotherm much later compared with the other channels. Based on these measurements, the temperature difference between the centerline and the periphery at filter inlet can be as high as 90°C during the first seconds of the heat-up phase. Figure 50 shows the steady-state temperature profiles used in the simulations at two reference centerline temperatures (300°C and 600°C). Linear interpolation was applied in-between. As a result, the simulation produced quite accurate results in the periphery for the period of interest. The importance of inlet temperature profile has been further investigated by the authors using CFD coupling (Koltsakis et al. 2009b), as shown in Figure 51, and will be discussed in the following sections.

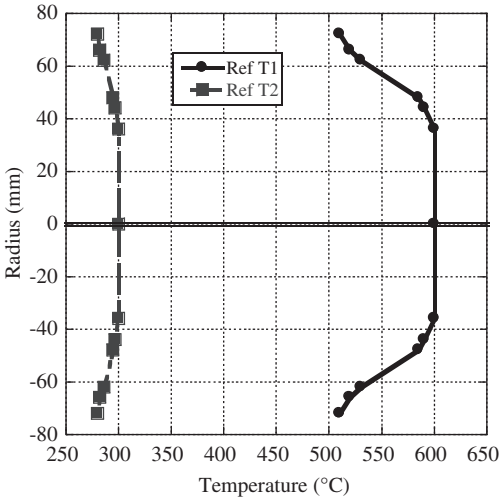

Figure 50 Inlet temperature profile at two reference centerline temperatures (300°C and 600°C) (Koltsakis et al. 2005).

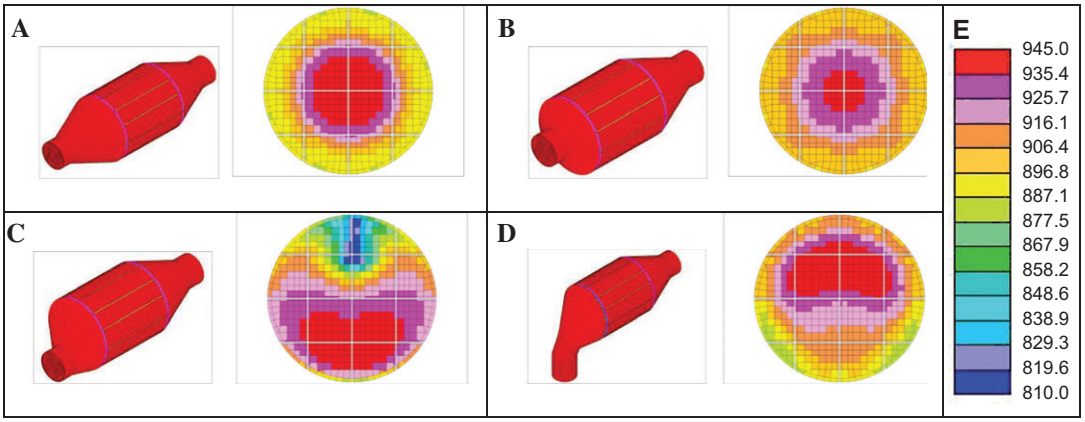

Figure 51 Calculated inlet gas temperature (in K) profiles at DPF entrance for the four inlet pipe geometries: (A) long cone, (B) short cone, (C) asymmetric cone, and (D) bent pipe (Koltsakis et al. 2009b).

4.3 DPF regeneration

The authors further illustrate the importance of 3D modeling in a series of simulations predicting "worst-case" regeneration events demonstrated on an engine bench. Using a common-rail 2 l engine with a Ce-based FBC system, experiments on this bench involve a 5.66×6″ (144×152 mm) SiC 200/15 filter and three different initial soot loadings. The setup of the experiment includes installation of thermocouples at different axial and radial positions in the filter, as shown in Figure 52.

The test protocol included a postinjection phase accompanied by a drastic temperature increase followed by a 20 s operation at low speed and low load without postinjection. The subsequent activation of a second postinjection event then occurs to complete the regeneration event. Repeat experiments occurred three times with three different initial soot loadings: 4, 6, and 8 g l^{-1}. Figure 53 presents the measured values versus the respective computed temperatures at three points along a filter channel located close to the centerline. As expected, the temperature levels increase for higher initial soot loadings with the predictions of the 3D model of relatively high accuracy for all three tests.

Figure 54 presents the results in two separate plots, each corresponding to a different plane. The top graph corresponds to the "45° plane" presenting the temperatures near the filter exit at four different radial positions. The results indicate that the evolution of the regeneration process varies from channel to channel, as evidenced by the differences in the temperature responses. The channel near the filter periphery (#14) heats up at a slower rate and exhibits an exotherm much later compared with the other channels. In the specific test, this is mainly due to the thermal boundary layer at the inlet of the DPF, which

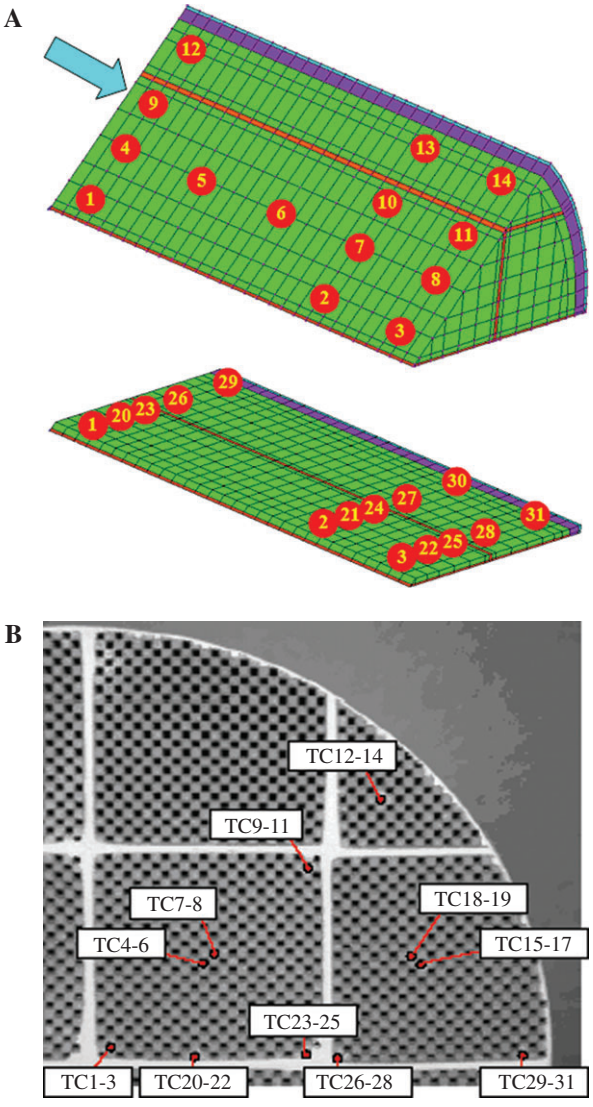

Figure 52 Schematic of thermocouples positioning in the filter and picture of the filter exit face showing the exact channel locations (Koltsakis et al. 2005).

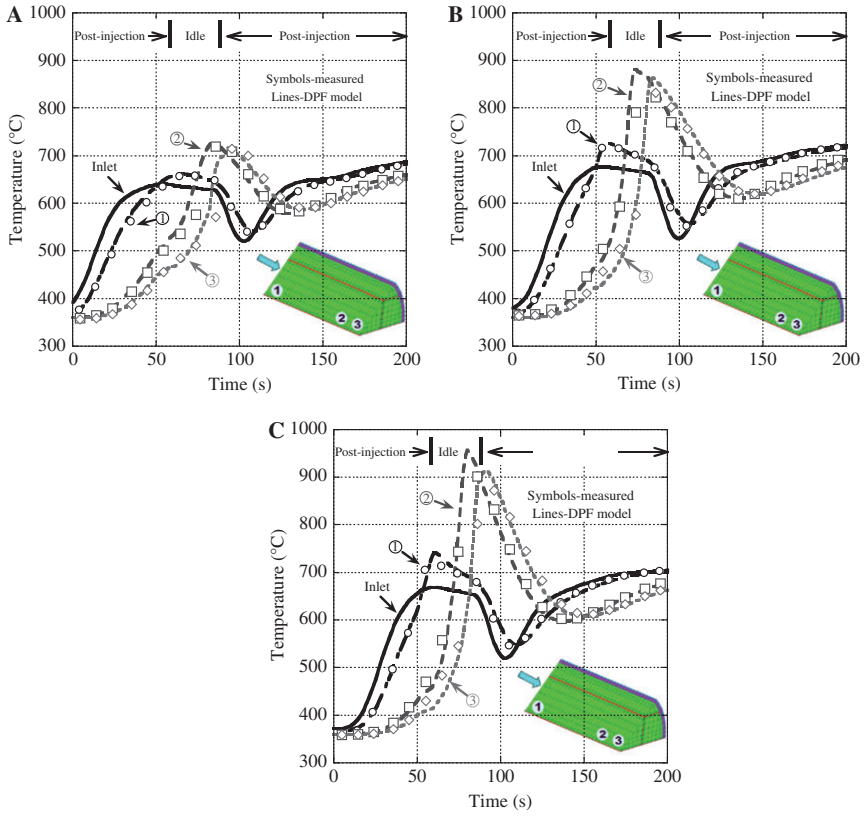

Figure 53 Measured (symbols) and computed (lines) filter temperatures along a filter channel: (A) 4 g l^{-1}, (B) 6 g l^{-1}, and (C) 8 g l^{-1} (Koltsakis et al. 2005).

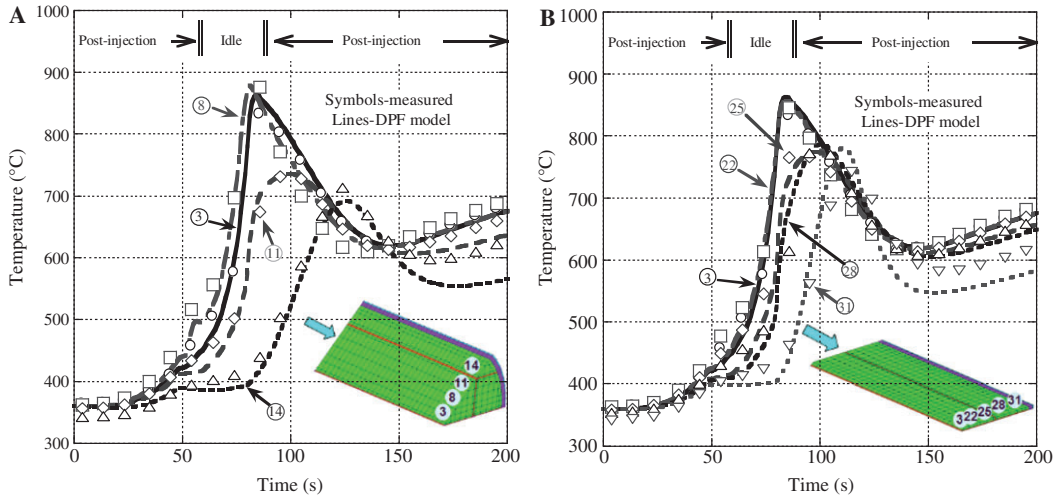

Figure 54 Measured (symbols) and computed (lines) filter temperatures at filter exit for 6 g l^{-1} soot loading: (A) 45° plane (3-8-11-14) and (B) 0° plane (3-22-25-28-31) (Koltsakis et al. 2005).

creates lower DPF inlet temperatures near the filter periphery. Based on these measurements, the temperature difference between the centerline and the periphery at filter inlet can be as high as 90°C during the first few seconds of the heat-up phase. This thermal boundary layer depends on the surface temperature of the metal pipe upstream the DPF and therefore is time dependent.

It is interesting to note that the fastest heat-up rate and the maximum temperature is seen in the channel located at the center of the filter segment (#8), whereas

the channel located at the filter centerline (#3) heats up slower and exhibits a lower temperature peak. All experiments demonstrate this behavior. The model results support this explanation, which relates to the additional heat capacity associated with the cement layers close to centerline. The same is true for the channel in the opposite segment corner (#11). Heat conduction influences the thermal response of the latter with the much colder periphery of the filter, as evidenced by the slower heat-up rate and lower temperature peak.

The bottom graph of Figure 54 presents the temperatures near the filter exit at five different radial positions of the "0° plane". Again, the thermal inertia of the neighboring cement layer similarly affects the channels corresponding to positions #3 and #22. At the positions close to the segment corner (#25 and #28), heat conduction once more influences the temperatures due to the colder periphery. Finally, near the periphery, at position #31, the inlet thermal boundary layer and the heat losses yet again retard the temperature increase. Interestingly, the peak temperature at #31 is slightly higher than the respective temperature at #14, although the thermocouple at #31 is closer to the periphery (10 mm from outer radius) compared with #14 (20 mm from outer radius). This is apparently due to 3D heat conduction because the positioning of the cement layers appears to act like insulators for the smallest filter segments.

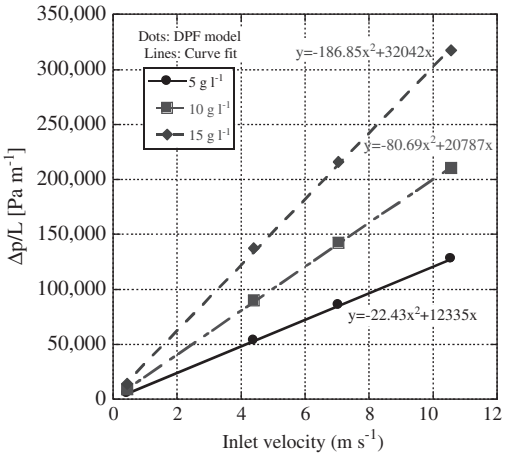

Figure 55 Pressure drop computed as a function of inlet gas velocity (T=500 K) (Koltsakis et al. 2005).

4.4 Coupling with CFD codes

Due to the importance of system packaging restrictions, aftertreatment devices require careful mounting and positioning to avoid unwanted effects from flow maldistribution (Hinterberger et al. 2007, Koltsakis et al. 2009b). In this case, it is important to calculate the influence of flow and temperature nonuniformities by simulating in a 3D environment the complete exhaust aftertreatment system. For this task, it is possible to couple the presented DPF model, and its derivatives, with commercial CFD packages. The porous medium approach has been employed for the simulation of the filter region, with pressure drop resistances (Figure 55), the mass and energy source terms taken from the described above DPF models.

This purpose involves the adoption of two different approaches. The first approach is a full coupling between the CFD software and the aftertreatment simulation code, which is treated as a user subroutine. The second approach is applicable for the case of inlet cone effects and its rationale is to minimize the calculation time. In this case, the CFD software provides only an initial flow solution. A special procedure calibrates the effect of the specific inlet cone on the flow profile. After this automatic calibration procedure, the calculation of the flow profile at the entrance proceeds second-by-second without the need to run the CPU-intensive CFD software.

The presence of an oblique flow field in front of a DPF has a certain impact on the resulting soot distribution during operation. On the other hand, the accumulated soot in the filter creates an additional flow resistance that tends to self-balance the flow maldistribution. The calculation of said effects occurs by coupling the DPF model with commercial CFD software and providing feedback to both simulations. Figure 56 presents a simulation example for the case of a DPF subjected to a nonuniform flow resulting from a bent inlet pipe. This simulation involves coupling the DPF model with Star-CD, a commercial CFD software program. This program is responsible to calculate the flow upstream and downstream of the DPF, whereas the DPF model, in the form of "user subroutine", calculates all the flow and filtration phenomena inside the DPF channels. The results show a homogenization of the initially nonuniform flow observed in the case of a clean DPF after soot accumulates in the filter. This is because soot accumulation ends up acting similar to a flow self-balancer. During regeneration, the inlet cone geometry can induce significant nonuniformities in temperature, flow, and soot loading consumption. Figure 57 shows the regeneration of a filter with bent inlet pipe. Due to the nonuniform inlet temperature profile, initial soot oxidation focuses on the upper central segments combined with sharp temperature increase in the same location. Subsequently, the localized soot consumption uncovers regions with lower flow resistance, resulting in higher local velocities and faster cooling.

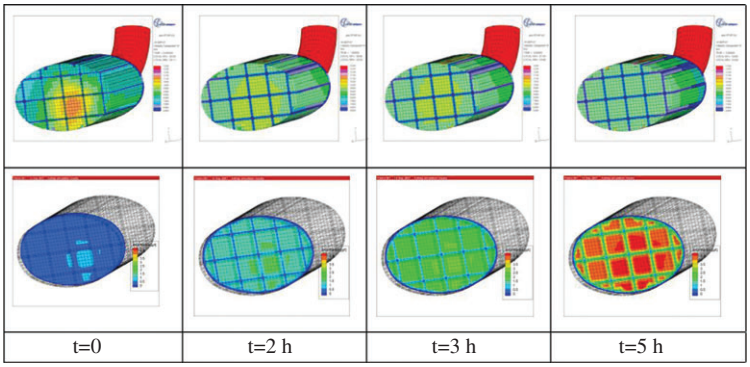

Figure 56 Flow maldistribution effect on soot loading calculated by coupling Star-CD with Axitrap. Top, flow distribution; bottom, soot distribution at one DPF slice.

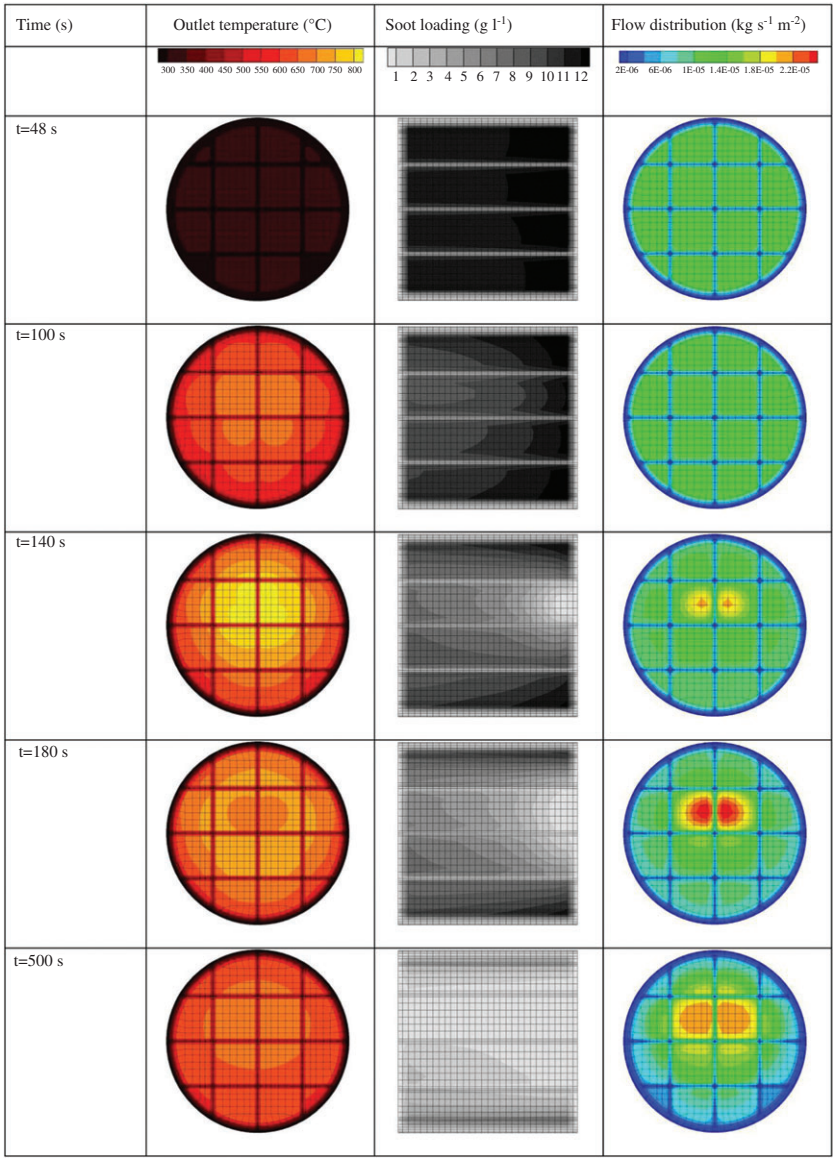

Figure 57 Computed outlet temperature profiles, soot loading fields, and inlet flow profiles during a transient regeneration of a filter with bent inlet pipe geometry (Koltsakis et al. 2009b).

At the same time, neighboring regions start to heat up and regenerate, which results in a slight homogenization of the flow. The final soot loading field remains highly nonuniform and a considerable fraction of the soot fails to regenerate in the periphery. The regeneration implications of several inlet cone geometries are summarized in Figure 58, which shows the peak temperatures and final soot fields in correlation with inlet temperature profile.

Coupling with CFD software is very important for certain applications where 3D effects require investigation in detail. However, in this combined example, the calculation time for a single time step increases significantly. In the case of DPF regeneration simulations, typically more than 1000 time steps are necessary. The CFD-integrated approach requires many hours of CPU time or even days on a single processor. In such cases, it is more practical to apply the second coupling approach mentioned above. This requires only one steady-state solution from the CFD software program. The DPF model is then responsible to calibrate the flow resistance parameters describing the inlet cone effect. The result is that the 3D simulation can be performed with very low CPU times (approx. 1 h for a 10-min regeneration on a single processor). The validity of this approach has been verified at several flow conditions with nonuniform soot loading, as shown in Figure 59, whereas the accuracy of the results is very satisfactory compared with the CFD simulation (Figure 60). Figure 61 presents such a regeneration simulation example for the case of an oval-shaped DPF subjected to a nonsymmetric flow and temperature profile.

4.5 Coupling with stress analysis codes

Due to the failure problems of DPFs, stress analysis was very early employed in the study of filters. Similar problems concerning flow-through substrates offered a useful basis in this respect (Heck et al. 2009). The first DPF stress analysis calculations involved 2D geometries and temperate fields estimated directly from measurements and later reached 3D geometries with equivalent or actual meshes and accurate temperature fields taken directly from validated DPF models. The setup of a stress analysis model involves, on the one hand, mesh and material properties and, on the other hand, structural loads, namely temperature conditions and mounting pressure.

Following the developments of DPF models, the first stress analysis calculations involved 2D meshes (Umehara and Nakasuji 1993, Miyairi et al. 2001), which evolved to 3D in the course of the last decade (Pontikakis et al. 2002, Barataud et al. 2003, Kuki et al. 2004, Hajireza et al. 2010). Related to the mesh selection are the structural properties of the material. A common feature in the articles referenced is the usage of an equivalent lumped material with anisotropic structural properties as explained by Kim (2004) instead of the actual honeycomb geometry. This allows the usage of simplified meshes skipping the channel details. It is also convenient when comparing stresses with failure limits, which are commonly given for equivalent materials due to the measurement techniques applied in practice (Stobbe et al. 1993). Of note, the equivalent failure limits are the product of both channel geometry and solid

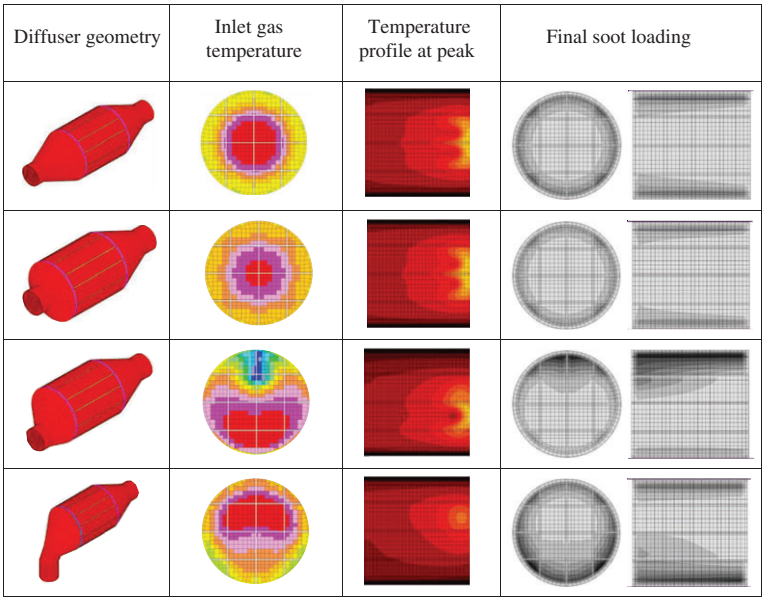

Figure 58 Effect of diffuser geometry on inlet gas temperature, temperature profile at the peak of the regeneration, and final soot loading (Koltsakis et al. 2009b).

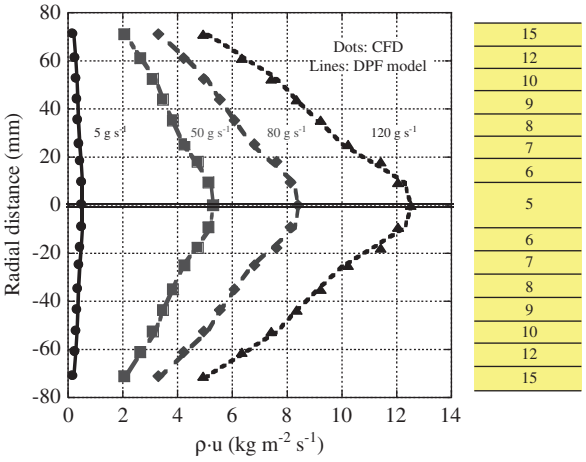

Figure 59 Right, assumed nonuniform soot distribution in a filter in grams per liter; left, flow distribution at filter inlet predicted by CFD and by the 3D DPF model (Koltsakis et al. 2005).

substrate material. It is worth noting the work of Kuki et al. (2004), who applied a two-step procedure. The first step involved a simplified 3D mesh and equivalent properties and the second step involved the actual channel geometry with plugs and channel imperfections at the periphery and solid material properties, thus aiming at better accuracy. Furthermore, to minimize the computer load, Kuki et al. confined their second calculation to a section around the critical location and used results of the previous calculation for the boundary conditions.

A nonuniform temperature field alone or together with a multimaterial structure causes the development of thermally induced stresses, which can be critical in the case of DPF. To estimate the complete temperature field, the first researchers (Umehara and Nakasuji 1993, Miyairi et al. 2001) interpolated data from several thermocouple measurements. The main contribution of validated DPF models (Pontikakis et al. 2002, Kuki et al. 2004) in the frame of direct coupling to stress analysis was the replacement of these rough approximations with accurately calculated 3D temperature fields, which were exported to stress analysis solvers. This procedure was repeated typically every time step to obtain the full history of stresses during a regeneration and estimate the global critical points (Hajireza et al. 2010), as shown in Figure 62. On top of thermal stresses, mounting pressure also causes stresses inside the filter. This extra load can be taken into account as a pressure at the periphery surface. Although the mounting pressure is dependent on the packaging technique (Rajadurai et al. 1999) and the mat's and canning's response to temperature excursions, it is usually assumed constant due to the complexity of estimating the temperature effect on the mounting pressure. Such a coupled calculation can take into account the effect of all material properties, substrate, cement, mat, and canning in the development of both temperature field and the resulting thermal stresses, thus allowing the overall study and optimization including thermal durability.

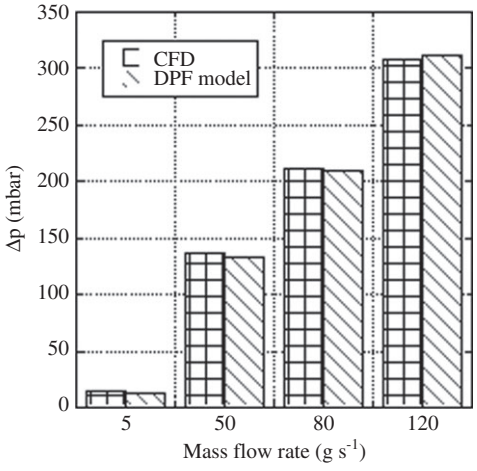

Figure 60 Computed pressure drop at different flow rates for a radially nonuniform loaded DPF (Koltsakis et al. 2005).

5 Other contributions

Similar to removing ash from a fireplace after the combustion of wood, ash will accumulate in the DPF during operation. The buildup of ash is a time-dependent phenomenon that will require special consideration during modeling. Moreover, DPFs are not required to use square channels. In the following sections, these last topics are discussed along with their resulting impact on the modeling equations.

5.1 Ash

The regeneration events used to remove soot result in the accumulation of ash within the DPF via two separate mechanisms. Depending on the type of regeneration, the ash will form a plug at the end of the channel or build up in the pores of the filter walls. Once regeneration occurs, ash is composed mostly of phosphorous, sulfur, calcium, and zinc (Ishizawa et al. 2009). Ash is an oxidized substance where the total amount is contingent on the metal elements in the lubricant additives in the engine oil and how much is consumed in the engine for nonadditive systems. With additive-based systems, the majority of the

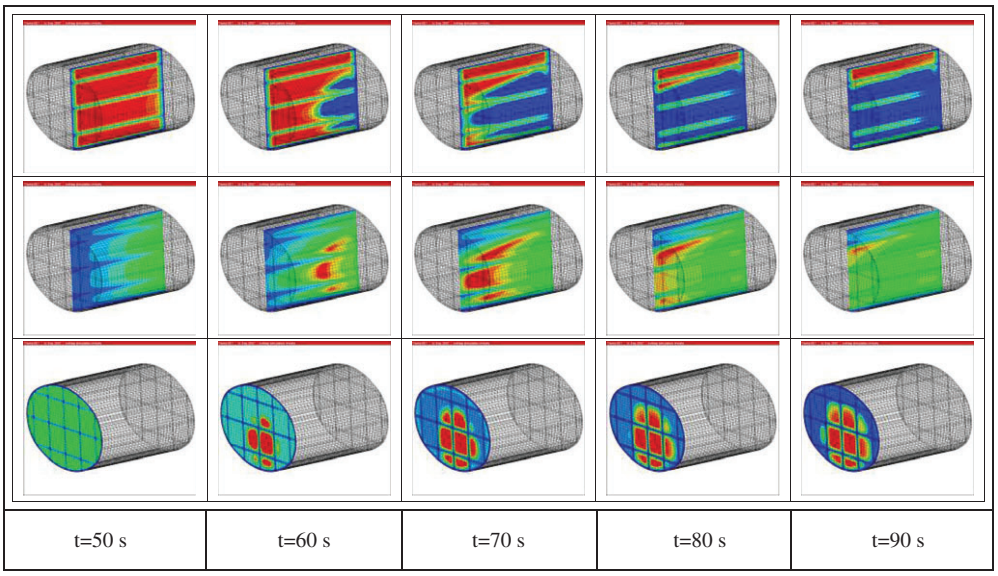

Figure 61 Soot loading (top), temperature (middle), and flow (bottom) distribution calculation during an oval DPF regeneration subjected to asymmetric inlet flow.

ash comes from the FBC with the remainder stemming from the engine oil components (Konstandopoulos et al. 2000, Gaiser and Mucha 2004, Konstandopoulos and Kladopoulou 2004, Ishizawa et al. 2009, Liati et al. 2012). Ash building up in either system increases the risk of uncontrollable combustion in the filter during regeneration (Ishizawa et al. 2009).

Two types of ash deposits form through the different regeneration modes of soot as well as the driving cycle of the engine (Gaiser and Mucha 2004). Ash produced during passive regeneration forms small clusters and stagnates in its area of production along the filter walls. This regeneration undergoes a cooler combustion temperature than active regeneration, making the ash particles much smaller but more dense. These small particles then adhere to the filter wall creating a buildup across the entire filtration area. This creates a significant pressure drop because the generated ash is not fully permeable; hence, this wall of ash restricts flow through the DPF while influencing the working life of the filter (Ishizawa et al. 2009). Under active regeneration, typically a larger amount of soot builds before regeneration occurs. Once regeneration commences, ash forms a large cluster that the exhaust gas carries throughout the inlet channel and accumulates to form a plug at the end of this channel. This reduces the effective length of the filtering wall and creates an increase in the pressure drop, although these larger clusters are more permeable that those generated through passive regeneration (Gaiser and Mucha 2004).

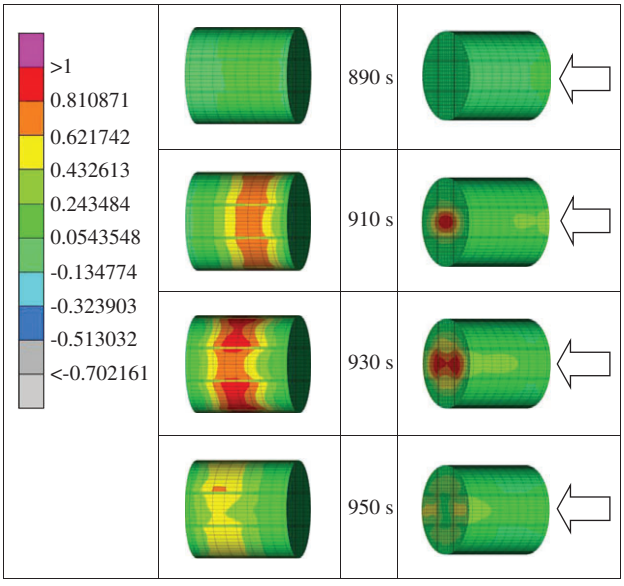

Figure 62 Left column, normal Z stresses (normalized values); right column, normal Y stresses (normalized values) (Hajireza et al. 2010).

The main difference between the two mechanisms is the ash particle size. When regeneration occurs at lower temperatures, smaller particles are formed that can fit inside the pores of the filter and begin to form a wall, reducing the effective permeability of the DPF wall and increasing the pressure drop. Under higher temperatures, the ash particles are larger and travel down the channel until the end where they become lodged (Gaiser and Mucha 2004, Ishizawa et al. 2009). In one study, Ishizawa et al. compared the two types of regeneration and took

pictures of the cross-section of the DPF to illustrate the differences. Each type of regeneration clearly influences filter operation in a different manner. However, equal amounts of ash from active regeneration forming a plug do not create the same amount of pressure drop as ash forming on the filter walls from passive regeneration. Ash spread uniformly across the filter walls creates a greater increase in pressure drop than when it forms a plug at the end of the channel. With respect to subsequent soot introduction after ash formation, soot primarily forms on top of the ash layer. However, it is possible for the soot and ash to create one common layer. Moreover, under high engine loads or substantial acceleration events, it is possible for soot to form under the ash layer. This combination of soot loading and ash generation affects DPF operation significantly (van Setten et al. 2001, Konstandopoulos et al. 2005, Johnson 2007).

Ash accumulation is a time-dependent phenomena that builds as a function of successive loading and regeneration events. At each snapshot in time, both the wall-generated and the plug-generated ash can be modeled through a thickness variable and included in DPF simulations as accomplished by Gaiser and Mucha (2004) and Konstandopoulos and Kladopoulou (2004). Moreover, the area-conserved efforts of Depcik allow modeling of this accumulation of ash along the channel through a shrinking gaseous channel area in the governing equations. However, a methodology is needed to track the accumulation of ash as a function of time. With the nonlinear operation of engines and on-road usage, a potentially quicker option is to formulate an effective permeability parameter as a function of engine run time. By factoring the reduced permeability of the ash, the resultant factors in the model via Eqs. (50) and (51) can be adjusted according using a simplified time factor effect on permeability and matched to a measured pressure drop across the device, which is analogous to a precious metal surface area parameter in catalyst modeling that can be used to factor sintering (Oh and Cavendish 1982).

5.2 Asymmetric channels

Asymmetric channel geometries have been proposed to account for the drawbacks of ash accumulation in the form of rear plugs. The basic idea is to increase the cross-section of the inlet channel in comparison with the outlet channel. Consequently, for a given volume of ash, the unavailable channel length is minimized and this can be used to reach the 250,000 km lifetime requirement or reduce the filter size.

Although a large variety of geometries including triangular and hexagonal shapes (ECOpoint 2012) has been studied, mostly square-like solutions have been selected for commercialization. The first from Ibiden with the acronym OS (OctoSquare) (Ogyu et al. 2004) features a large octagonal inlet channel and a smaller square outlet channel. The second from Corning with the acronym ACT (Young et al. 2004) features a large inlet square channel and a smaller outlet square channel. An asymmetric solution has also been proposed by NGK with the HAC concept (Caroca et al. 2009).

To model asymmetric geometries, the ratio (d_{c2}/d_{c1}) is necessary as input parameter to calculate the inlet and outlet channel widths d_{c1} and d_{c2}:

$$d_{c1}=\frac{2}{1+\left(d_{c2}/d_{c1}\right)}\left(\sqrt{\frac{1}{cpsm}}-t_f\right) \tag{162}$$

where cpsm is the channels per square meter. Additionally, to define the full geometry, the corner side width d_{c3} has to be calculated for the octagonal channel, as shown in Figure 63:

$$d_{c3}=\frac{\sqrt{2}}{2}\left[\left(1-d_{c2}/d_{c1}\right)d_{c1}-\left(2-\sqrt{2}\right)t_f\right]. \tag{163}$$

Indicatively, the effect of channel geometry on pressure drop for an ash-free filter is shown in Figure 64A. A common cell density of 300 cpsi and a wall thickness of 12 mil has been selected for all cases. The outlet-inlet channel ratio has been selected as 0.7. The symmetric design presents lower backpressure at soot loadings below 3 g l^{-1}, attributed to the lower axial flow resistance in the outlet channel. At higher loadings, the smaller filtration area becomes critical and asymmetric geometries show slightly lower backpressure. The real advantage of these geometries is shown in Figure 64B. In the complete range, the asymmetric geometries perform better with a reduction

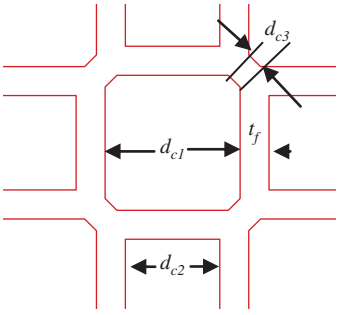

Figure 63 Schematic of octagonal inlet channels and square outlet channels.

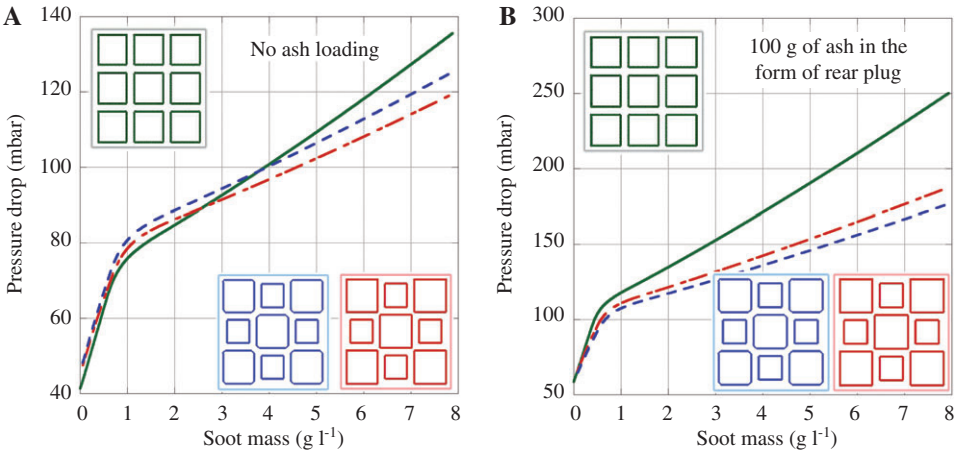

Figure 64 Effect of soot loading on pressure drop for symmetric and asymmetric channel geometries (300 cpsi, 12 mil, 0.7 channel width ratio): (A) no soot loading and (B) 100 g ash.

of approximately 30% in back-pressure at the maximum loading.

5.3 Inhomogeneous wall structure

Since 2008, an inhomogeneous wall structure technology has been presented by several DPF suppliers (Ogyu et al. 2008, Furuta et al. 2009, Wolff et al. 2010, Iwasaki et al. 2011). This technology concerns the addition of a membrane or layer with small pores usually on top of the standard wall layer. For comparative purposes, Figure 65 sketches the soot distribution in the wall of a standard DPF compared with a DPF with this membrane. The thin membrane provides highly effective filtration with empty filters and accelerates the soot cake formation. Because of the membrane, the soot trapped inside the wall can be decreased significantly. This subsequently improves the fuel economy of the engine due to a reduced pressure drop and restriction in the exhaust. In addition, Mizutani et al. (2010) noticed that the correlation of pressure drop and soot becomes linear with the addition of a membrane, which brings advantages in on-board estimations of the current soot load.

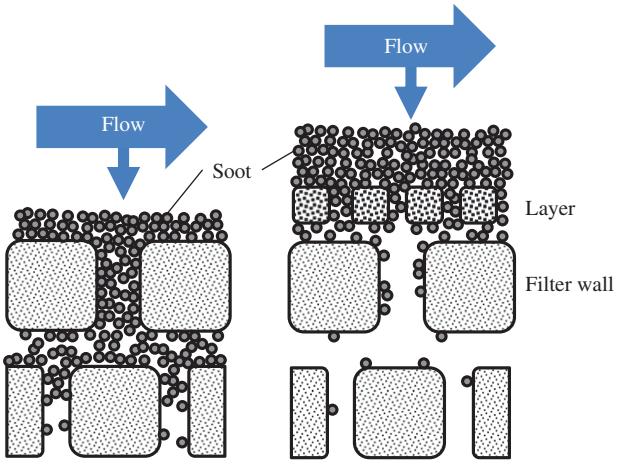

Figure 65 Schematic soot accumulation at standard DPF (left) and membrane DPF (right) (Koltsakis et al. 2012).

These functionalities have been explained theoretically using a detailed multilayered wall model (Koltsakis et al. 2012). The filtration efficiency of a DPF is most crucial when it is empty. After forming a sufficient soot cake, the cake acts as filter providing approximately perfect filtration. Hence, the target is to reach the cake filtration condition as soon as possible. With the membrane layer added, the duration can be notably decreased while at the same time reducing the soot slip and the amount of soot inside the wall. This embedded soot in the wall is largely responsible for the high-pressure drop across the filter. Figure 66 compares the number-based filtration per particle size of a conventional filter (single-layer) and a layered (double-layer) filter at the beginning of a loading event. The benefit of the layer is obvious. In particular, the number of small particles with diameter of 23–70 nm is reduced considerably. Figures 67 and 68 show the filtration efficiency and resulting soot slip for the beginning of the simulated loading case, with both benefitting substantially from the addition of this layer. With a higher filtration efficiency of the empty filter and faster cake formation, the soot slip is appreciably reduced. Figure 69 displays the soot accumulation in the filter over the first 6000 s. The soot inside the wall is considerable lower

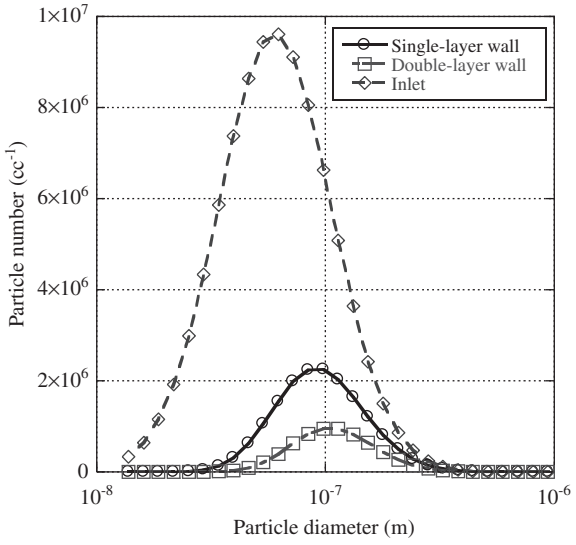

Figure 66 Particle number-based filtration per particle size of clean filter (Koltsakis et al. 2012).

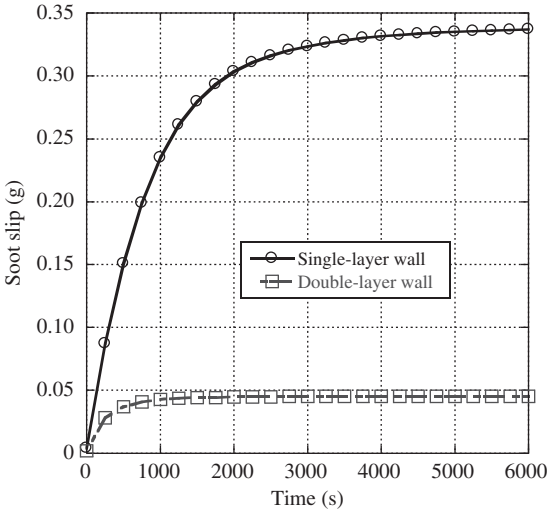

Figure 68 Soot slip during steady-state loading of empty filters (Koltsakis et al. 2012).

with the layer addition. As a result, although the relatively dense membrane layer increases the initial pressure drop of the filter, the reduction in soot stored within the wall quickly demonstrates the overriding benefit of adding a membrane layer (Figure 70).

6 Conclusion

Catalyzed DPF modeling has advanced steadily for over three decades, supporting the market introduction of efficient and reliable diesel aftertreatment concepts. It is currently accepted that modeling is indispensable for understanding the fundamental phenomena inside the catalyzed filter and their contribution to overall performance. The complexity stemming from the plethora of phenomena, the multiple scales, and the variety of catalyst configurations and geometries is of special scientific interest. All these challenges have been faced with increasingly detailed and accurate models supported by extensive experimental validations. As a result, today's advanced computations tools are considered by many not only an exhaust system design and optimization aid but also an integral part of the development process, offering insight for further improvements and breakthroughs in DPF technology. Despite the maturity of the modeling and

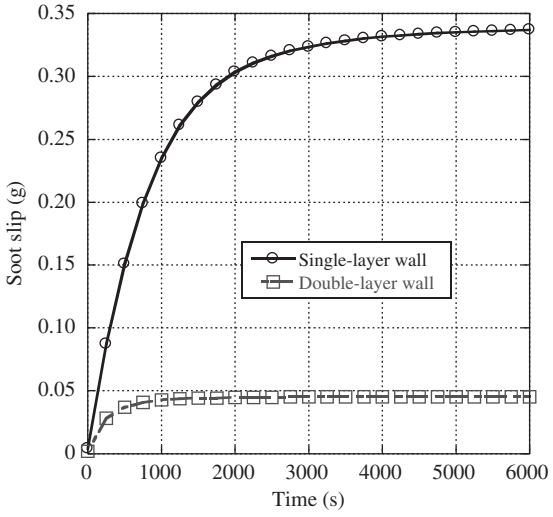

Figure 67 Filtration efficiency during steady-state loading of empty filters (Koltsakis et al. 2012).

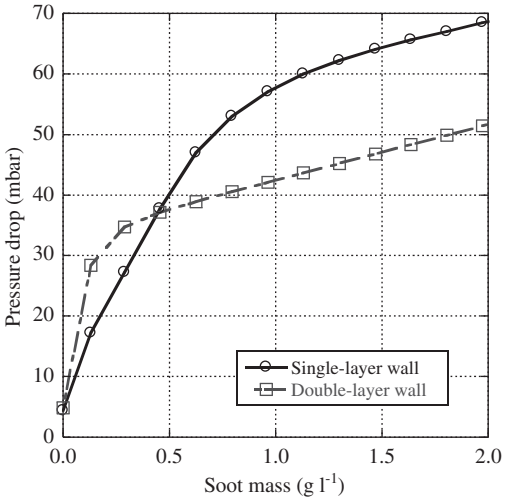

Figure 69 Soot mass during steady-state loading of empty filters (Koltsakis et al. 2012).

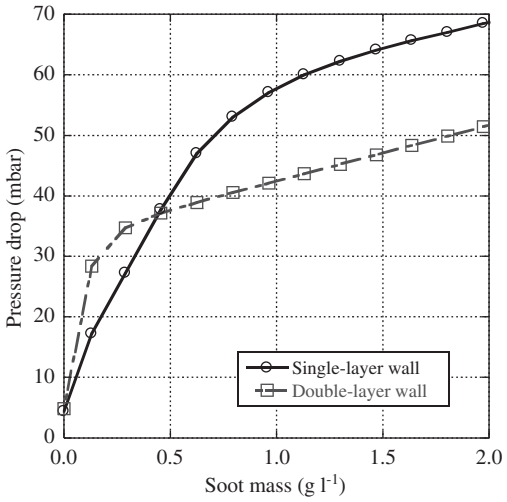

Figure 70 Pressure drop during steady-state loading of empty filters (Koltsakis et al. 2012).

simulation tools, a number of topics still pose challenges to the aftertreatment engineers, especially with respect to soot thermophysical and chemical properties, which are typically engine dependent. Further work is also in progress to address increased accuracy requirements in long-term pressure drop predictions in the cases of repeated partial regenerations as well as phenomena related to soot aging and semistochastic migration along the inlet channel. Finally, the aspects of catalyzed DPF aging and the prediction of ash accumulation are expected to attract the interest of DPF modeling engineers in the near future.

Nomenclature

$\tilde{a}$ Surface area density [m^{-1}]
A Cross-sectional area [m^2]
A Preexponential [m K^{-1} s^{-1}]
A_{flt} Filtration area [m]
A_s Cross-sectional area in soot layer per unit length [m]
A_w Cross-sectional area in wall layer per unit length [m]
B Width available to flow [m]
c Specific heat [J kg^{-1} K^{-1}]
c Species concentration [kg m^{-3}]
c_m Soot migration constant [—]
c_p Constant pressure specific heat of gas [J kg^{-1} K^{-1}]
D Diameter [m]
d_b Unit cell diameter [m]
d_c Characteristic dimension of unit spherical collector (loaded) [m]
d_c^0 Characteristic dimension of unit spherical collector (clean) [m]
d_{c1} Asymmetric inlet channel diameter [m]
d_{c2} Asymmetric outlet channel diameter [m]
d_{c3} Corner side width [m]
d_{cdl} Characteristic delay length [m]
d_{eff} Effective length scale for deposition [m]
d_p Pore diameter [m]
D Species or soot diffusion [m^2 s^{-1}]
$\mathbf{D}$ Vector of species diffusion [m^2 s^{-1}]
D_i Inner DPF zone diameter [m]
D_o Outer DPF zone diameter [m]
$\mathbf{D}^T$ Thermal diffusion vector [m^2 s^{-1}]
E_a Activation energy [J mol^{-1}]
f Haralampous et al. geometry factor [—]
F Friction factor of Bissett (28.454) [—]
F View factor in filter energy equation [—]
f_y Geometrical parameter [—]
h Specific enthalpy [J kg^{-1}]
h_c Convective heat transfer coefficient in soot and wall layers [W m^{-2} K^{-1}]
h_g Convective heat transfer coefficient in the channels [W m^{-2} K^{-1}]
k Rate constant [m s^{-1}]
k_B Boltzmann's constant [m^2 kg s^{-2}]
k_m Mass-transfer coefficient [m s^{-1}]
ℓ Mean free path [m]
L Channel length [m]
m Mass [kg]
$\dot{m}$ Mass flow rate [kg s^{-1}]
N_c Total number of channels [—]
N_{ic} Total number of inlet channels [—]
N_s Number of discretizations in the soot and wall layer [—]
p Pressure [Pa]
p_a Compressibility pressure indicative of cake layer strength [Pa]
p_c Compressive stress on cake layer [Pa]
p_m Solid compressive stress [Pa]
Pe Peclet number [—]
$\dot{q}$ Volumetric energy source [W m^{-3}]
$\dot{Q}_{cat}$ Energy released through direct soot conversion through catalyzed surface [W m^{-1}]
$\dot{Q}_{cond}$ Energy due to conduction within the wall [W m^{-2}] or [W m^{-1}]
$\dot{Q}_{conv}$ Energy due to convection of gas in channels [W m^{-2}] or [W m^{-1}]
$\dot{Q}_{inner}$ Energy due to convection in soot and wall layers [W m^{-1}]
$\dot{Q}_{multi}$ Energy due to multidimensional conduction effects [W m^{-1}]
$\dot{Q}_{rad}$ Radiation energy within filter channels [W m^{-1}]
$\dot{Q}_{reac}$ Energy exotherm/endotherm due to soot/wall reactions [W m^{-2}] or [W m^{-1}]
$\dot{Q}_{supply}$ Active energy supply to wall [W m^{-1}]
$\dot{Q}_{wall}$ Energy flow through the wall [W m^{-1}]
r Radial direction in multidimensional DPF models [m]
R Reaction rate of soot oxidation [s^{-1}]
R Gas constant [J mol^{-1} K^{-1}]
$\dot{\mathbf{R}}$ Catalytic reaction vector [mol m^{-3} s^{-1}]
R_{red} Fuel additive reaction rate [s^{-1}]
R_u Universal gas constant (8.3145) [J mol^{-1} K^{-1}]
S Surface area per unit length [m]
$\dot{\mathbf{S}}$ Array of soot conversion rates [kg m^{-3} s^{-1}]
S_a Surface area [m^2]
S_{ca} Catalytic surface area [m^2]
SCF Slip flow effects [—]
s_F Specific area of filter [m^{-1}]
$\dot{S}_{C_{(s)}}$ Overall soot combustion rate [kg $C_{(s)}$ m^{-3} s^{-1}]
$\dot{S}_{\text{mass}}$ Total mass accumulation rate [kg m^{-3} s^{-1}]
$\dot{S}_{CO}$ Carbon monoxide generation rate [kg CO m^{-3} s^{-1}]
$\dot{S}_{CO_2}$ Carbon dioxide generation rate [kg CO_2 m^{-3} s^{-1}]
$\dot{S}_{O_2}$ Oxygen combustion rate [kg O_2 m^{-3} s^{-1}]

S_p Specific surface area of soot [m^{-1}]
t Time or thickness [s] or [m]
t_d Soot thickness [m]
t_f Filter wall thickness [m]
T Temperature [K]
T_f Temperature of solid phase in the wall [K]
T_w Temperature of gas phase in the wall [K]
$\overline{T}$ Average temperature [K]
u Velocity [m s^{-1}]
$\overline{u}$ Average velocity in soot and wall layer [m s^{-1}]
V Volume per axial length [m^2]
$\mathbf{V}$ Diffusion velocity vector [m s^{-1}]
V_{de} Total empty channel volume with soot present per axial length [m^2]
V_{DPF} Total DPF volume in model zone per axial length [m^2]
V_e Total empty channel volume per axial length [m^2]
W Molecular weight [g mol^{-1}]
$\mathbf{W}$ Vector of molecular weights [g mol^{-1}]
$\hat{W}$ Mixture molecular weight [g mol^{-1}]
X Mole fractions [—]
$\mathbf{X}$ Vector of mole fractions [—]
y Soot and wall (normal) distance [m]
Y Mass fractions [—]
$\mathbf{Y}$ Vector of mass fractions [—]
z Channel (axial) distance [m]

Greek variables

α Thermal diffusivity [m^2 s^{-1}]
α_1 O_2 partial oxidation factor [—]
α_2 NO_2 partial oxidation factor [—]
α_{cat} Catalytic reaction index of completeness [—]
β Forchheimer inertial coefficient [m^{-1}]
χ Inverse of soot combustion time scale [s^{-1}]
ΔH_{reac} Heat of reaction [J mol^{-1}]
ε DPF void fraction [—]
ε_d DPF void fraction with soot present [—]
ε_p Filter porosity [%]
ε_p^0 Clean filter porosity [%]
ε_s Cake solidosity [—]
ε_s^0 Uncompressed state of cake solidosity [—]
Φ Partition coefficient [—]
κ Constant that represents continuum description of soot microstructure [—]
K Darcy's law permeability [m^2]
η Efficiency [%]
η_c Local collection efficiency [%]
φ Constant that represents continuum description of soot microstructure [—]
λ Thermal conductivity [W m^{-1} K^{-1}]
λ^* Thermal conductivity influenced by close proximity of filter [W m^{-1} K^{-1}]
λ_{eff} Effective radial thermal conductivity that includes geometric details [W m^{-1} K^{-1}]
μ Dynamic viscosity of gas [kg m^{-1} s^{-1}]
θ Soot accumulation angle [°]
ρ Density [kg m^{-3}]
σ Stephen-Boltzmann constant [W m^{-2} K^{-4}]
s Mass flow rate of soot to the surface per mesh interval [kg $C_{(s)}$ m^{-1} s^{-1}]
τ Tortuosity [—]
ω Dimensionless percolation factor [—]
ξ Moles of metal oxides in soot as compared to carbon [—]
Ξ Effective Peclet number for soot layer width [—]
ψ Flow resistance coefficient [—]

Subscript and sub-subscript

d Soot
f Filter
fd Fully developed
g Gas
i Discretization index
I Inlet channel
II Outlet channel
j Species and normal index numbers
Kn Knudsen
n Time index
NM Total number of species
r Interception
s Soot gas layer
w Wall
* Iterative guesses

Received July 18, 2012; accepted November 19, 2012

References

Ahlström AF, Odenbrand CI. Combustion characteristics of soot deposits from diesel engines. Carbon J 1989; 27: 475–483.

Allansson R, Blakeman PG, Cooper BJ, Hess H, Silcock PJ, Walker AP. Optimising the low temperature performance and regeneration efficiency of the continuously regenerating diesel particulate filter (CR-DPF) system. SAE Paper 2002-01-0428, 2002.

Aoki H, Asano A, Kurazono K, Kobashi K, Sami H. Numerical simulation model for the regeneration process of a wall-flow monolith diesel particulate filter. SAE Paper 930364, 1993.

Awara AE, Opris CN, Johnson JH. A theoretical and experimental study of the regeneration process in a ceramic diesel particulate trap using a copper fuel additive. SAE Paper 970188, 1997.

Ballinger T, Cox J, Konduru M, De D, Manning W, Andersen P. Evaluation of SCR catalyst technology on diesel particulate filters. SAE Paper 2009-01-0910, 2009.

Banno Y, Tanak Y, Hihara T, Nagata M. Pre-filter diesel oxidation catalyst development for DOC-CSF dystem. SAE Paper 2004-01-1430, 2004.

Barataud C, Bardon S, Bouteiller B, Gleize V, Charlet A, Higelin P. Diesel filter optimization. SAE Paper 2003-01-0376, 2003.
Beck JL. Convection in a box of porous material saturated with fluid. Phys Fluids 1972; 15: 1377–1383.
Benedict RP, Carlucci NA, Swetz SD. Flow loss in abrupt enlargements and contractions. J Eng Power 1966; 88: 73–81.
Bissett EJ. Combustion of particles on regenerable filters with large conduction. Warren, MI: General Motors Research, 1981.
Bissett EJ. Mathematical model of the thermal regeneration of a wall-flow monolith diesel particulate filter. Chem Eng Sci 1984; 39: 1232–1244.
Bissett EJ. Thermal regeneration of particle filters with large conduction. Math Model 1985; 6: 1–18.
Bissett EJ, Shadman F. Thermal regeneration of diesel particulate monolithic filters. AIChE J 1985; 31: 753–758.
Bissett EJ, Kostoglou M, Konstandopoulos AG. Frictional and heat transfer characteristics of flow in square porous tubes of wall-flow monoliths. Chem Eng Sci 2012; 84: 255–265.
Boomsma K, Poulikakos D. On the effective thermal conductivity of a three-dimensionally structured fluid-saturated metal foam. Int J Heat Mass Transfer 2001; 44: 827–836.
Brinkman HC. A calculation of the viscous force exerted by a flowing fluid on a dense swarm of particles. Appl Sci Res A 1947a; 1: 27–34.
Brinkman HC. On the permeability of media consisting of closely packed porous particles. Appl Sci Res A 1947b; 1: 81–86.
Calmidi VV, Mahajan RL. Forced convection in high porosity metal foams. J Heat Transfer 2000; 122: 557–565.
Caroca J, Villata D, Fino D, Russo N. Comparison of different diesel particulate filters. Top Catal 2009; 52: 2076–2082.
Cavataio G, Girard JW, Lambert C. Cu/zeolite SCR on high porosity filters: laboratory and engine performance evaluations. SAE Paper 2009-01-0897, 2009a.
Cavataio G, Warner JR, Girard JW, Ura J, Dobson D, Lambert CK. Laboratory study of soot, propylene, and diesel fuel impact on zeolite-based SCR filter catalysts. SAE Paper 2009-01-0903, 2009b.
Coltrin ME, Kee RJ, Rupley FM. Surface Chemkin: a Fortran package for analyzing heterogeneous chemical kinetics at a solid-surface-gas-phase interface. Albuquerque, NM: Sandia National Laboratories, 1990.
Cooper BJ, Thoss JE. Role of NO in diesel particulate emission control. SAE Paper 890404, 1989.
Cooper BJ, Jung HJ, Thoss JE. Treatment of diesel exhaust gases. Taylor, MI, 1990.
Cussler EL. Diffusion: mass transfer in fluid systems. Cambridge, UK: Cambridge University Press, 1995.
d'Hueppe A, Chandesris M, Jamet D, Goyeau B. Boundary conditions at a fluid-porous interface for a convective heat transfer problem: analysis of the jump relations. Int J Heat Mass Transfer 2011; 54: 3683–3693.
Darcy HPG. Les Fontaines Publiques de la Ville de Dijon. Paris, 1856.
Dardiotis C, Haralampous O, Koltsakis GC. Catalytic oxidation performance of wall-flow vs flow-through monoliths for diesel emissions control. Ind Eng Chem Res 2006; 45: 3520–3530.
Dardiotis CK, Haralampous OA, Koltsakis GC. Catalytic oxidation in wall-flow reactors with zoned coating. Chem Eng Sci 2008; 63: 1142–1153.
Depcik C. Simulating the concentration equations and the gas-wall interface for one-dimensional based diesel particulate filter models. ASME J Eng Gas Turbines Power 2010; 132: 1–12.
Depcik C, Assanis D. One-dimensional automotive catalyst modeling. Prog Energy Combust Sci 2005; 31: 308–369.
Depcik C, Assanis D. Simulating area conservation and the gas-wall interface for one-dimensional based diesel particulate filter models. ASME J Eng Gas Turbines Power 2008; 130: 1–18.
Depcik C, Srinivasan A. One + one-dimensional modeling of monolithic catalytic converters. Chem Eng Technol 2011; 34: 1949–1965.
Depcik C, van Leer B, Assanis D. The numerical simulation of variable-property reacting-gas dynamics: new insights and validation. Numer Heat Transfer A Appl 2005; 47: 27–56.
ECOpoint. ECOpoint Consultants. http://www.dieselnet.com/ecopoint, 2012.
Forchheimer P. Wasserbewegung durch Boden. Z Ver Dtsch Ing 1901; 45: 1736–1741, 1781–1788.
Fukushima S, Ohno K, Vlachos N, Konstandopoulos AG. New approach for pore structure and filtration efficiency characterization. SAE Paper 2007-01-1918, 2007.
Furuta Y, Mizutani T, Miyairi Y, Yuki K, Kurachi H. Study on next generation diesel particulate filter. SAE Paper 2009-01-0292, 2009.
Gaiser G, Mucha P. Prediction of pressure drop in diesel particulate filters considering ash deposit and partial regenerations. SAE Paper 2004-01-0158, 2004.
Gallant T. Single channel DPF experiments to investigate soot cake structures. 11th Diesel Engine Emissions Reduction (DEER) Conference, Chicago, 2005.
Gantawar AK, Opris CN, Johnson JH. A study of the regeneration characteristics of a silicon carbide and cordierite diesel particulate filters using a copper fuel additive. SAE Paper 970188, 1997.
Garner CP, Dent JC. A thermal regeneration model for monolithic and fibrous diesel particulate traps. SAE Paper 880007, 1988.
General Motors. General Motors response to EPA notice of proposed rulemaking on particulate regulation for light-duty diesel vehicles submitted to Environmental Protection Agency, 1979.
Gropi G, Tronconi E. Continuous vs. discrete models of nonadiabatic monolith catalysts. AIChE J 1996; 42: 2382–2387.
Hajireza S, Johannesen LT, Wolff T, Koltsakis GC, Samaras ZC, Haralampous OA. A modeling and experimental investigation on an innovative substrate for DPF applications. SAE Paper 2010-01-0891, 2010.
Haralampous OA, Koltsakis GC. Intra-layer temperature gradients during regeneration of diesel particulate filters. Chem Eng Sci 2002; 57: 2345–2355.
Haralampous OA, Koltsakis GC. Back-diffusion modeling of NO_2 in catalyzed particulate filters. Ind Eng Chem Res 2004a; 43: 875.
Haralampous OA, Koltsakis GC. Oxygen diffusion modeling in diesel particulate filter regeneration. AIChE J 2004b; 50: 2008–2019.
Haralampous OA, Koltsakis GC, Samaras ZC. Partial regenerations in diesel particulate filters. SAE Paper 2003-01-1881, 2003.
Haralampous OA, Dardiotis CK, Koltsakis GC, Samaras ZC. Study of catalytic regeneration mechanisms in diesel particulate filters using coupled reaction-diffusion modeling. SAE Paper 2004-01-1941, 2004a.
Haralampous OA, Kandylas IP, Koltsakis GC, Samaras ZC. Diesel particulate filter pressure drop. Part I: modeling and experimental validation. Int J Engine Res 2004b; 5: 149–162.
Haralampous OA, Kandylas IP, Koltsakis GC, Samaras ZC. Experimental evaluation of apparent soot oxidation rates in diesel particulate filters. Int J Vehicle Des 2004c; 35: 365–382.

Haralampous OA, Koltsakis GC, Samaras ZC, Vogt C-D, Ohara E, Watanabe Y, Mizutani T. Modeling and experimental study of uncontrolled regenerations in SiC filters with fuel borne catalyst. SAE Paper 2004-01-0697, 2004d.

Haralampous OA, Koltsakis GC, Samaras ZC, Vogt C-D, Ohara E, Watanabe Y, Mizutani T. Reaction and diffusion phenomena in catalyzed diesel particulate filters. SAE Paper 2004-01-0696, 2004e.

Harvey GD, Baumgard KJ, Johnson JH, Gratz LD, Bagley ST, Leddy DG. Effects of a ceramic particle trap and copper fuel additive on heavy-duty diesel emissions. SAE Paper 942068, 1994.

Hawker P, Myers N, Hüthwohl G, Vogel HT, Bates B, Magnusson L, Bronnenberg P. Experience with a new particulate trap technology in Europe. SAE Paper 970182, 1997.

Hawker P, Hüthwohl G, Henn J, Koch W, Lüders H, Lüers B, Stommel P. Effect of a continuously regenerating diesel particulate filter on non-regulated emissions and particle size distribution. SAE Paper 980189, 1998.

Hayes RE, Kolaczkowski ST, Li PK, Awdry CS. Evaluating the effective diffusivity of methane in the washcoat of a honeycomb monolith. Appl Catal B Environ 2000; 25: 93–104.

Heck RH, Farrauto RJ, Gulati ST. Catalytic air pollution control: commercial technology. New York, NY: John Wiley and Sons, 2009.

Heywood JB. Internal combustion engine fundamentals. New York: McGraw-Hill, 1988.

Hindmarsh AC. Serial Fortran solvers for ODE initial value problems. http://www.llnl.gov/CASC/odepack, 2002.

Hinterberger C, Olesen M, Kaiser R. D simulation of soot loading and regeneration of diesel particulate filter systems. SAE Paper 2007-01-1143, 2007.

Ho FG, Strieder W. Numerical evaluation of the porous medium effective diffusivity between the Knudsen and continuum limits. J Chem Phys 1980; 73: 6296–6300.

Howitt JS, Montierth MR. Cellular ceramic diesel particulate filter. SAE Paper 810114, 1981.

Ingham DB, Bejan A, Mamut E, Pop I. Emerging technologies and techniques in porous media. Dordrecht: Kluwer Academic Publishers, 2004.

Ishizawa T, Yamane H, Satoh H, Sekiguchi K, Arai M, Yoshimoto N, Inoue T. Investigation into ash loading and its relationship to DPF regeneration method. SAE Paper 2009-01-2882, 2009.

Iwasaki S, Mizutani T, Miyairi Y, Yuuki K, Makino M. New design concept for diesel particulate filter. SAE Int J Engines 2011; 4: 527–536.

Jacquot F, Logie V, Brilhac JF, Gilot P. Kinetics of the oxidation of carbon black by NO_2. Influence in the presence of water and oxygen. Carbon 2002; 40: 335–343.

Johnson TV. Diesel emission control in review. SAE Paper 2007-01-0233, 2007.

Johnson TV. Diesel emission control in review. SAE Paper 2009-01-0121, 2009.

Jørgensen MW, Sorenson SC. A 2-dimensional simulation model for a diesel particulate filter. SAE Paper 970471, 1997.

Kandylas IP, Koltsakis GC. Simulation of continuously regenerating diesel particulate filters in transient driving cycles. Proc Inst Mech Eng D J Automobile Eng 2002; 216: 591–606.

Kandylas IP, Haralampous OA, Koltsakis GC. Diesel soot oxidation with NO_2: engine experiments and simulations. Ind Eng Chem Res 2002; 41: 5372–5384.

Kim JS. Substrate failure prediction during converter canning process. SAE Paper 2004-01-1134, 2004.

Knoth JF, Drochner A, Vogel J, Gieshoff J, Koegel M, Pfeifer M, Votsmeier M. Transport and reaction in catalytic wall-flow filters. Catal Today 2005; 105: 598.

Kolaczkowski ST. Measurement of effective diffusivity in catalytic coated monoliths. Catal Today 2003; 83: 85–95.

Koltsakis GC, Stamatelos AM. Modeling catalytic regeneration of wall-flow particulate filters. Ind Eng Chem Res 1996a; 35: 2–13.

Koltsakis GC, Stamatelos AM. Modeling thermal regeneration of wall-flow diesel particulate traps. AIChE J 1996b; 42: 1662–1672.

Koltsakis GC, Stamatelos AM. Catalytic automotive exhaust aftertreatment. Prog Energy Combust Sci 1997a; 23: 1–39.

Koltsakis GC, Stamatelos AM. Modes of catalytic regeneration in diesel particulate filters. Ind Eng Chem Res 1997b; 36: 4155–4165.

Koltsakis GC, Haralampous OA, Margaritis NK, Samaras ZC, Vogt C-D, Ohara E, Watanabe Y, Mizutani T. 3-Dimensional modeling of the regeneration in SiC particulate filters. SAE Trans J Fuels Lubricants (SAE Paper 2005-01-0953) 2005.

Koltsakis GC, Konstantinou A, Haralampous OA, Samaras Z. Measurement and intra-layer modeling of soot density and permeability in wall-flow filters. SAE Trans J Fuels Lubricants (SAE Paper 2006-01-0261) 2006.

Koltsakis GC, Haralampous O, Samaras Z, Kraemer L, Heimlich F, Behnk K. Control strategies for peak temperature limitation in DPF regeneration supported by validated modeling. SAE Paper 2007-01-1127, 2007.

Koltsakis GC, Haralampous O, Koutoufaris IZ. Potential and challenges of integrating de-NO_x catalysts on DPF substrates. SIA Paper R-2008-05-22, 2008.

Koltsakis GC, Dardiotis CK, Samaras Z, Maunula T, Kinnunen T, Lundorf P. Optimization methodology for DPF substrate-catalyst combinations. SAE Paper 2009-01-0291, 2009a.

Koltsakis GC, Samaras ZC, Echtle H, Chatterjee D, Markou P, Haralampous OA. Flow maldistribution effects on DPF performance. SAE Paper 2009-01-1280, 2009b.

Koltsakis GC, Bollerhoff T, Samaras Z, Markomanolakis I. Modeling the interactions of soot and SCR reactions in advanced DPF technologies with nonhomogeneous wall structure. SAE Paper 2012-01-1298, 2012.

Konstandopoulos AG. Flow resistance descriptors for diesel particulate filters: definitions, measurements and testing. SAE Paper 2003-01-0846, 2003.

Konstandopoulos AG, Johnson JH. Wall-flow diesel particulate filters – their pressure drop and collection efficiency. SAE Paper 890405, 1989.

Konstandopoulos AG, Kladopoulou E. The optimum cell density of wall-flow monolithic filters: effects of filter permeability, soot cake structure and ash loading. SAE Paper 2004-01-1133, 2004.

Konstandopoulos AG, Kostoglou M. Periodically reversed flow regeneration of diesel particulate traps. SAE Paper 1999-01-0469, 1999.

Konstandopoulos AG, Kostoglou M. Reciprocating flow regeneration of soot filters. Combust Flame 2000; 121: 488–500.

Konstandopoulos AG, Kostoglou M. Microstructural aspects of soot oxidation in diesel particulate filters. SAE Paper 2004-01-0693, 2004.

Konstandopoulos AG, Kostoglou M. Computationally fast implementations of convection, diffusion, and chemical

reaction phenomena in diesel particulate filters. SAE Paper 2010-01-0890, 2010.
Konstandopoulos AG, Kostoglou M, Skaperdas E, Papaioannou E, Zarvalis D, Kladopoulou E. Fundamental studies of diesel particulate filters: transient loading, regeneration and aging. SAE Paper 2000-01-1016, 2000.
Konstandopoulos AG, Kostoglou M, Housiada P. Spatial non-uniformities in diesel particulate trap regeneration. SAE Paper 2001-01-0908, 2001.
Konstandopoulos AG, Skaperdas E, Masoudi M. Microstructural properties of soot deposits in diesel particulate traps. SAE Paper 2002-01-1015, 2002.
Konstandopoulos AG, Kostoglou M, Housiada P, Vlachos N, Zarvalis D. Multichannel simulation of soot oxidation in diesel particulate filters. SAE Paper 2003-01-0839, 2003a.
Konstandopoulos AG, Vlachos N, Housiada P, Kostoglou M. Simulation of triangular-cell-shaped, fibrous wall-flow filters. SAE Paper 2003-01-0844, 2003b.
Konstandopoulos AG, Kostoglou M, Vlachos N, Kladopoulou E. Progress in diesel particulate filter simulation. SAE Paper 2005-01-0946, 2005.
Konstandopoulos A, Kostoglou M, Vlachos N, Kladopoulou E. Advances in the science and technology of diesel particulate filter simulation. Adv Chem Eng 2008; 33 213–294.
Kostoglou M, Housiada P, Konstandopoulos AG. Multi-channel simulation of regeneration in honeycomb monolithic diesel particulate filters. Chem Eng Sci 2003; 58: 3273–3283.
Kuki T, Miyairi Y, Kasai Y, Miyazaki M, Miwa S. Study on reliability of wall-flow type particulate filter. SAE Paper 2004-01-0959, 2004.
Lee W-T. Local preconditioning of the Euler equations. Ann Arbor, MI: Doctor of Philosophy, University of Michigan, 1992.
Lee KO, Yang SY. Parametric examination of filtration processes in diesel particulate filter membranes with channel structure modification. SAE Paper 2010-01-0537, 2010.
Lee JH, Paratore MJ, Brown DB. Evaluation of Cu-based SCR/DPF technology for diesel exhaust emission control. SAE Paper 2008-01-0072, 2008.
Li CG, Koelman H, Ramanathan R, Baretzky U, Forbriger G, Meunier T. Particulate filter design for high performance diesel engine application. SAE Paper 2008-01-1747, 2008.
Liati A, Eggenschwiler PD, Gubler EM, Schreiber D, Aguirre M. Investigation of diesel ash particulate matter: a scanning electron microscope and transmission electron microscope study. Atmos Environ 2012; 49: 391–402.
Liu J, Schorn N, Schernus C, Peng L. Comparison studies on the method of characteristics and finite difference methods for one-dimensional gas flow through IC engine manifold. SAE Paper 960078, 1996.
Lu W, Zhao CY, Tassou SA. Thermal analysis on metal-foam filled heat exchangers. Part I: metal-foam filled pipes. Int J Heat Mass Transfer 2006; 49: 2751–2761.
MacDonald JS, Vaneman GL. Experimental evaluation of fibrous filters for trapping diesel-exhaust particulates. SAE Paper 810956, 1981.
Maly M, Claussen M, Carlowitz O, Kroner P, Ranalli M, Schmidt S. Influence of nitrogen dioxide based regeneration on soot distribution. SAE Paper 2004-01-0823, 2004.
Mason EA, Malinaukus AP. Gas transport in a porous media: the dusty gas model. Amsterdam: Elsevier, 1983.
Masoudi M, Konstandopoulos AG, Nikitidis MS, Skaperdas E, Zarvalis D, Kladopoulou E, Altiparmakis C. Validation of a model and development of a simulator for predicting the pressure drop of diesel particulate filters. SAE Paper 2001-01-0911, 2001.
Miller RK, Li CG. Effect of catalyst support structure on conversion efficiency. SAE Paper 2001-01-0183, 2000.
Miyairi Y, Miwa S, Abe F, Xu Z, Nakasuji Y. Numerical study on force regeneration of wall-flow diesel particulate filters. SAE Paper 2001-01-0912, 2001.
Mizutani T, Watanabe Y, Yuuki K, Hashimoto S, Hamanaka T, Kawashima J. Soot regeneration model for SiC-DPF system design. SAE Paper 2004-01-0159, 2004.
Mizutani T, Iwasaki S, Miyairi Y, Yuuki K, Makino M, Kurachi H. Performance verification of next generation diesel particulate filter. SAE Paper 2010-01-0531, 2010.
Mogaka ZN, Wong VW, Shahed SM. Performance and regeneration characteristics of a cellular ceramic diesel particulate trap. SAE Paper 820272, 1982.
Mohammed H, Triana AP, Yang S-L, Johnson JH. An advanced 1D 2-layer catalyzed diesel particulate filter model to simulate: filtration by the wall and particulate cake, oxidation in the wall and particulate cake by NO_2 and O_2, and regeneration by heat addition. SAE Paper 2006-01-0467, 2006.
Nield DA, Bejan A. Convection in porous media, 3rd ed. New York, NY: Springer-Verlag, 2006.
Ochoa-Tapia JA, Whitaker S. Heat transfer at the boundary between a porous medium and a homogeneous fluid. Int J Heat Mass Transfer 1997; 40: 2691–2707.
Ogyu K, Ohno K, Hong S, Komori T. Ash storage capacity enhancement of diesel particulate filter. SAE Paper 2004-01-0949, 2004.
Ogyu K, Oya T, Ohno K, Konstandopoulos AG. Improving of the filtration and regeneration performance by the SiC-DPF with the layer coating of PM oxidation catalyst. SAE Paper 2008-01-0621, 2008.
Oh SH, Cavendish JC. Transients of monolithic catalytic converters: response to step changes in feedstream temperature as related to controlling automobile emissions. Ind Eng Chem Res 1982; 2: 29–37.
Oh SH, MacDonald JS, Vaneman GL, Hegedus LL. Mathematical modeling of fibrous filters for diesel particulates – theory and experiment. SAE Paper 810113, 1981.
Onorati A, Ferrari G, D'Errico G. Fluid dynamic modeling of the gas flow with chemical specie transport through the exhaust manifold of a four cylinder SI engine. SAE Paper 1999-01-0557, 1999.
Opris CN, Johnson JH. A 2-D computational model describing the flow and filtration characteristics of a ceramic diesel particulate trap. SAE Paper 980545, 1998a.
Opris CN, Johnson JH. A 2-D computational model describing the heat transfer, reaction kinetics and regeneration characteristics of a ceramic diesel particulate trap. SAE Paper 980546, 1998b.
Pattas KN, Samaras ZC. Computational simulation of the ceramic trap transient operation. SAE Paper 890403, 1989.
Pattas KN, Stamatelos AM, Koltsakis GC, Kandylas IP, Mustel W. Computer aided engineering in the design of catalytically assisted trap systems. SAE Paper 970472, 1997.

Pauli E, Lepperhoff G, Pischinger F. The description of the regeneration behavior of diesel particulate traps with the aid of a mathematical model. SAE Paper 830180, 1983.
Peters BJ. Numerical simulation of a diesel particulate filter during loading and regeneration. 2003 Spring Technical Conference of the ASME Internal Combustion Engine Division, Salzburg, Austria, 2003.
Peters BJ, Wanker RJ, Münzer A, Wurzenberger JC. Integrated 1D to 3D simulation workflow of exhaust aftertreatment devices. SAE Paper 2004-01-1132, 2004.
Pontikakis G, Stamatelos A, Bakasis K, Aravas N. 3-D catalytic regeneration and stress modeling of diesel particulate filters by ABAQUS FEM software. SAE Paper 2002-01-1017, 2002.
Punke A, Grubert G, Li Y, Dettling J, Neubauer T. Catalyzed soot filters in close coupled position for passengers vehicles. SAE Paper 2006-01-1091, 2006.
Rajadurai S, Tagomori MK, Berryhill J, Baig A, Snider BJ. Single seam stuffed converter design for thinwall substrates. SAE Paper 1999-01-3628, 1999.
Reaction Design. Transport core utility manual. San Diego, CA, 2003.
Reif FP. Statistical and thermal physics. New York: McGraw-Hill, 1975.
Roe PL. Characteristic-based schemes for the Euler equations. Ann Rev Fluid Mech 1986; 18: 337–365.
Romero AF, Castrejón-Rodríguez J, Serrano-Romero R. Self regenerating catalyzed diesel aftertreatment system. SAE Paper 950367, 1995.
Romero AF, Gutiérrez R, García-Moreno R. Combustion processes of particulate matter and soot in ceramic filter traps for diesel engines and numerical modeling. SAE Paper 970475, 1997.
Sahraoui M, Kaviany M. Slip and no-slip temperature boundary conditions at the interface of porous plain media: convection. Int J Heat Mass Transfer 1994; 37: 1029–1044.
Salvat O, Marez P, Belot G. Passenger car serial application of a particulate filter system on a common rail direct injection diesel engine. SAE Paper 2000-01-0473, 2000.
Shadman F, Bissett EJ. Analysis of thermal regeneration of fibrous diesel-particulate filters. Ind Eng Chem Prod Res Dev 1983; 22: 203–208.
Shampine LF, Reichelt MW, Kierzenka JA. Solving index-I DAEs in MATLAB and Simulink. SIAM Rev 1999; 41: 538–552.
Smith JM. Chemical engineering kinetics. New York: McGraw-Hill, 1970.
Sorenson SC, Høj JW, Stobbe P. Flow characteristics of SiC diesel particulate filter materials. SAE Paper 940236, 1994.
Springer KJ, Stahman RC. Removal of exhaust particulate from a Mercedes 300D diesel car. SAE Paper 770716, 1977.
Sprouse III C, Mangus M, Depcik C. Diesel particulate filter model with detailed permeability analysis. 2011.
Stobbe P, Petersen HG, Høj JW, Sorenson SC. SiC as a substrate for diesel particulate filters. SAE Paper 932495, 1993.
Stratakis GA. Experimental investigation of catalytic soot oxidation and pressure drop characteristics in wall-flow diesel particulate filters. Doctor of Philosophy, University of Thessaly, 2004.
Suresh A, Johnson JH. A Study of dilution effects on particle size measurement from a heavy-duty diesel engine with EGR. SAE Paper 2001-01-0220, 2001.
Tan JC, Opris CN, Baumgard KJ, Johnson JH. A study of the regeneration process in diesel particulate traps using a copper fuel additive. SAE Paper 960136, 1996.
Tessier LP, Sullivan HF, Bragg GM, Hermance CE. The development of a high efficiency diesel exhaust particulate filter. SAE Paper 800338, 1980.
Tighe CJ, Twigg MV, Hayhurst AN, Dennis JS. The kinetics of oxidation of diesel soots by NO_2. Combust Flame 2011; 159: 77–90.
Umehara K, Nakasuji Y. Lifetime prediction of wall-flow type diesel particulate filters using fatigue characteristics. SAE Paper 930128, 1993.
van Setten BAAL, Makkee M, Moulijn JA. Science and technology of catalytic diesel particulate filters. Catal Rev 2001; 43: 489–564.
Versaevel P, Colas H, Rigaudeau C, Noirot R, Koltsakis GC, Stamatelos AM. Some empirical observations on diesel particulate filter modeling and comparison between simulations and experiments. SAE Paper 2000-01-0477, 2000.
Votsmeier M, Gieshoff J, Kogel M, Pfeifer M, Knoth JF, Drochner A, Vogel H. Wall-flow filters with wall-integrated oxidation catalyst: a simulation study. Appl Catal B Environ 2007; 70: 233–240.
Wakao N, Kaguei S, Funazkri T. Effect of fluid dispersion coefficients on particle-to-fluid heat transfer coefficients in packed beds. Chem Eng Sci 1979; 34: 325–336.
Wark K, Warner CF. Air pollution: its origin and control, 2nd ed. New York: Harper & Row, Publishers, 1981.
Wolff T, Friedrich H, Johannesen L, Hajireza S. A new approach to design high porosity silicon carbide substrates. SAE Paper 2010-01-0539, 2010.
Wooding RA. Steady state free thermal convection of liquid in a saturated permeable medium. J Fluid Mech 1957; 2: 273–285.
Young D, Hickman DA, Bhatia G, Gunasekaran N. Ash storage concept for diesel particulate filters. SAE Paper 2004-01-0948, 2004.
Zhao CY, Kim T, Lu TJ, Hodson HP. Thermal transport in high porosity cellular metal foams. J Thermophys Heat Transfer 2004; 18: 309–317.
Zukauskas AA. Convective heat transfer in cross-flow. In: Kakac S, Shah RK, Aung W, editors. Handbook of single-phase convective heat transfer. New York: Wiley, 1987.

Dr. Grigorios Koltsakis received his diploma and PhD from the Department of Mechanical Engineering of Aristotle University of Thessaloniki. He is currently an Associate Professor at the Laboratory of Applied Thermodynamics of Aristotle University. Dr. Koltsakis is specialized in internal combustion engines, with emphasis on catalysis and aftertreatment technology. His research and teaching interests further include catalysis, heat transfer, and numerical methods. Dr. Koltsakis currently leads a research group working on the simulation and evaluation of aftertreatment technologies. He is the cofounder and director of Exothermia SA, a university spinoff company developing exhaust system simulation software.

Dr. Onoufrios Haralampous is an Assistant Professor at Technological and Educational Institute of Larissa since 2010. His research interests cover modeling of transport phenomena and numerical methods with emphasis on internal combustion engines and exhaust aftertreatment. After his graduation from Aristotle University Thessaloniki in 2000, he continued his studies as a PhD candidate at the Laboratory of Applied Thermodynamics, participating in projects funded by the automotive and fuel industry. During this period, he developed advanced computational codes for modeling of exhaust aftertreatment devices and was awarded by SAE with “Arch T. Colwell Merit Award” for his work in DPF modeling. He finished his PhD in 2005, and in 2007, he participated in the foundation of Exothermia SA, a spinoff company of Laboratory of Applied Thermodynamics, where he was responsible for the successful commercialization of these codes. He is the author of more than 30 publications in international journals and conferences.

Dr. Christopher Depcik is an Assistant Professor from the Department of Mechanical Engineering at the University of Kansas. Before joining the University of Kansas, he worked at the University of Michigan as a postdoctoral research fellow. He received his PhD in mechanical engineering from the University of Michigan in 2003 as well as his MS in aerospace engineering in 2002 and MS in mechanical engineering in 1999. He received his BS in mechanical engineering from the University of Florida in 1997. Dr. Depcik conducts research revolving around a sustainable approach to energy and the transportation infrastructure. This includes a feedstock to tail-pipe analysis of fuel production and its resultant combustion, exhaust emissions, and energy recovery using multiple feedstock and different fuels. This incorporates the development of predictive models for catalytic exhaust aftertreatment devices. Students in his University of Kansas EcoHawks design project research electrified vehicles, renewable energy, and their interconnection with the electrical grid.

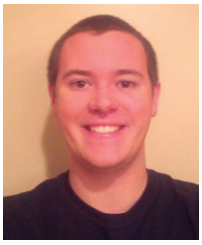

J. Colter Ragone is a brake design engineer for Honda R&D Americas located in Ohio. He worked under Dr. Christopher Depcik as a research assistant at the University of Kansas, where he received his MS in mechanical engineering in 2012. Before his graduate studies, Colter completed a BS in mechanical engineering from the University of Arizona in 2010.